Geoingegneria Ambientale e Mineraria
Geoengineering Environment and Mining

GEAM

Pàtron Editore 169

Rivista della **ASSOCIAZIONE GEORISORSE E AMBIENTE**

SOMMARIO

In copertina: Scorcio del Monte Bianco da
Entreves (AO)

Autore: Paolo Dabove

GEAM

Editorial

The second issue of the GEAM magazine for the year 2023 (n. 169) includes five very transversal articles. Some of these concern the mining environment, with the main focus on the positioning of tools, machines, and operators; others focus on the design of torrential barriers or the soil behaviour in function of temperature in the context of climate change. Particular attention is also paid to geology in this issue, with a contribution regarding the statistical analysis of boreholes and geological data applied to a specific case study in Italy.

After some time, we return to talk about safety in the workplace in the GEAM magazine: one of the articles is dedicated in particular to this activity, with a review regarding the occupational and environmental safety of fluids in chainsaw operations.

We are continuously trying to include articles related to different topics in order to give the readers the possibility to have a broad spectrum of issues and provide the most interesting articles regarding the geoengineering and environmental aspects from a scientific point of view. I hope you will enjoy the articles included in this issue, so I leave you to read the scientific contributions the authors have decided to publish in this magazine.

Paolo Dabove

https://www.geam-Journal.org/homepage

Application of positioning systems for the working bodies of mining equipment to update mining surveying plans and digital surface models

Andrey S. Eliseev*
Abdelwahab Agaguena**
Vladimir N. Gusev***
Aleksandr V. Mikhailov***

* Postgraduate Student of the Mining Surveying Department, Saint Petersburg Mining University, Russia
** Postgraduate Student of the Mechanical Engineering Department, Saint Petersburg Mining University, Russia
*** Doctor of Engineering Sciences, Saint Petersburg Mining University, Russia

Corresponding author:
eliseev.spmi@bk.ru

The Mining Surveying Department performs a wide range of tasks: it takes part in drawing up plans for the development of a deposit, monitors compliance with design decisions during the construction of a quarry, deals with issues of monitoring the movement of a rock mass, calculates production volumes and supports drilling and blasting. In this regard, the issue of automation of daily mining surveying tasks is acute. To date, there are technologies that allow to automate most of the daily tasks of the mining surveying service and bring economic benefits to the enterprise. Such technologies include systems for positioning the working bodies of mining equipment – a set of sensors and controllers installed on a working machine. These systems are already actively used abroad and in some Russian road construction companies. The aim of the work is to increase the efficiency of the mining surveying service in open-pit mining by introducing a positioning system for mining equipment. The article deals with the issue of using in the production of systems for positioning the working bodies of mining equipment in order to update mining surveying plans and digital surface models. The accuracy with which these solutions can work is calculated.

Keywords: *technologies, positioning, leveling, excavation.*

1. Introduction

The mining sector has been rapidly developing in recent years and, accordingly, the requirements for the accuracy of work are increasing, the issue of increasing the productivity of equipment and reducing costs is very acute. First of all, it is necessary to reduce the indicators of losses and dilution during the development of the deposit.

In the practice of mining, the main role in transferring the design position of workings to the area is assigned to the mining surveying service, which performs this task using traditional methods (Blishchenko, 2020; Voroshilov, 2007).

Nowadays, in order to update the situation of mining operations and reconcile with the project, they mainly use tacheometric surveys, surveys with satellite equipment and periodic surveys using UAVs and scanning systems. It is necessary to spend a lot of time preparing, shooting and processing information to perform each of these operations. The departure of the mining surveying service to the mine is often associated with risks to life and health. Often, machine downtime is related to weather conditions. (Agaguena *et al.*, 2021). For such work, it is necessary to regularly update the mining surveying support network. In addition, an extensive fleet of devices must be monitored and updated periodically.

The survey results, after processing in software environments, are applied to the mining surveying plans and the current digital surface model is updated. For this purpose, specialized programs are used, such as: Autodesk Autocad, Autodesk Civil 3D, CredoDat, Agisoft PhotoScan. This is not a complete list. Some programs are bundled with the equipment, others must be purchased separately. Each of these programs takes time to master.

There are already solutions on the market for mining products that automate mining processes in a quarry. This solution is a positioning system for mining machines and equipment that allows to determine the position of the working body of the machine (Park *et al.*, 2021; Siukhin, Zverev & Balashov, 2018; Batalina & Ilemkova, 2013).

Positioning systems greatly increase the productivity of equipment, eliminating downtime. All that a surveyor needs to do when servicing such systems is to download the design position of

the development elements into the machine controller (Pugin & Piramatov, 2017).

The history of control over the position of the working bodies of construction machines dates back to the era of the USSR. The positioning of the working body on road works was carried out relative to a stretched metal (string line) string (Ministry of Transport, 1978). The work consisted of installing a string line and constantly checking its accuracy. The next stage in the development of positioning systems was laser and ultrasonic systems (Khvalev, Satyukov & Orekhov, 2017; Zubova, 2013). Currently, ultrasonic and laser systems are used for high-precision site planning (Dudnik, Govorukhin & Tupoleva, 2018). The laser positioning system works by linking the machine to a robotic tacheometer (the tacheometer is a source of a laser beam, and a reflec-

tor is installed on the road construction machine), this system is highly accurate, but has speed limits and cannot work if there are obstacles between the tacheometer and the machine. The ultrasonic positioning system works on the basis of data received from ultrasonic sensors that determine the distance to the ground. The latest generation are satellite positioning systems of equipment. The advantage of these systems is that the operation of the system is possible if there are obstacles between the equipment and the base station (Sahapov, 2019; Tselovalnikov, 2006; Potiuchliaev, 2012). The appearance of these systems made it possible to make their use on mining machines massive. In foreign practice, there are almost no productions where this technology is not used.

The following article provides an overview of the main types of

positioning systems on the market that can replace traditional surveying methods.

1.1. Overview of modern types of positioning systems

The excavator working equipment positioning system is a 3D control system designed to improve the efficiency of the excavator, which allows to see the current position of the excavator bucket in the coordinate system in real time (fig. 1).

In 3D systems, the excavator determines its position in absolute coordinates relative to the digital model of the required surface. The coordinate system can be selected based on the ease of use for certain types of work (Mustafin & Tran Thanh Son, 2018). The position of the working body of the machine is determined in coordinates
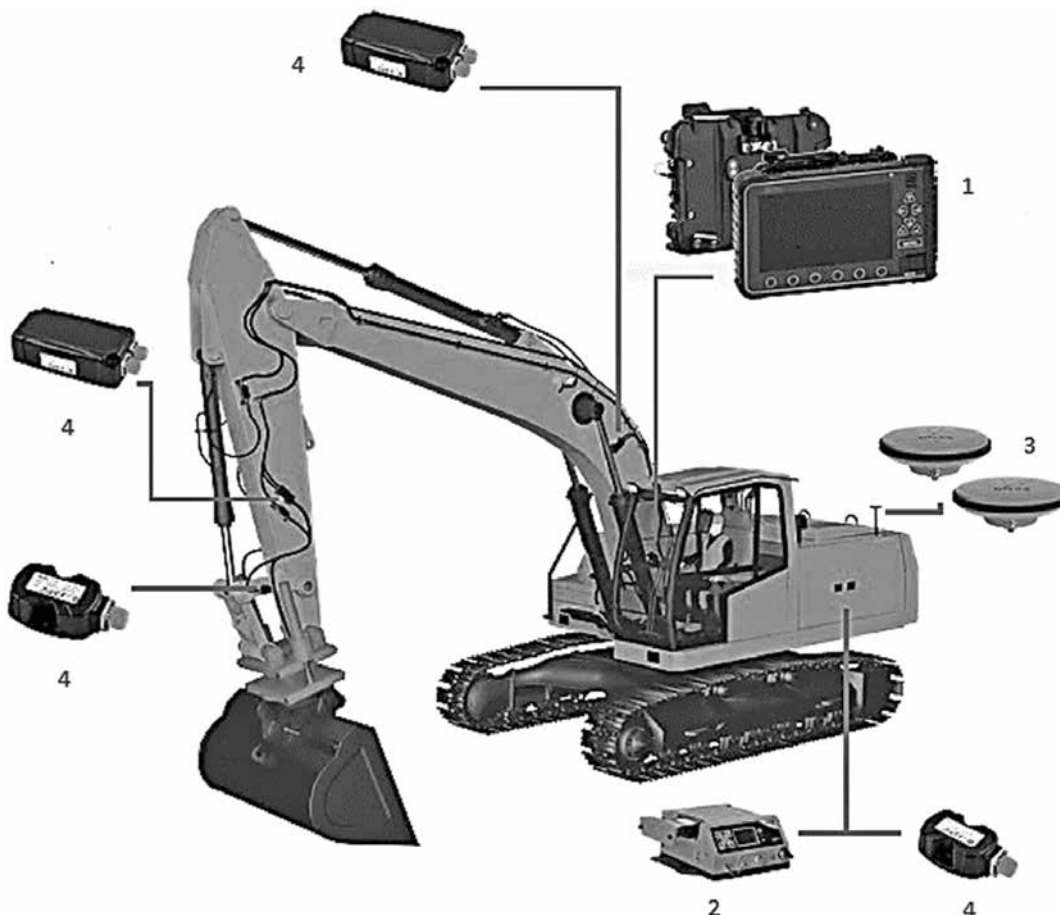
Fig. 1 – The structure of the placement of the bucket positioning systems on the excavator, where: 1. Control Panel; 2. Sensor Data Receiver; 3. GNSS Antennas; 4. Angle Sensors. *Source:* Compiled by the authors.
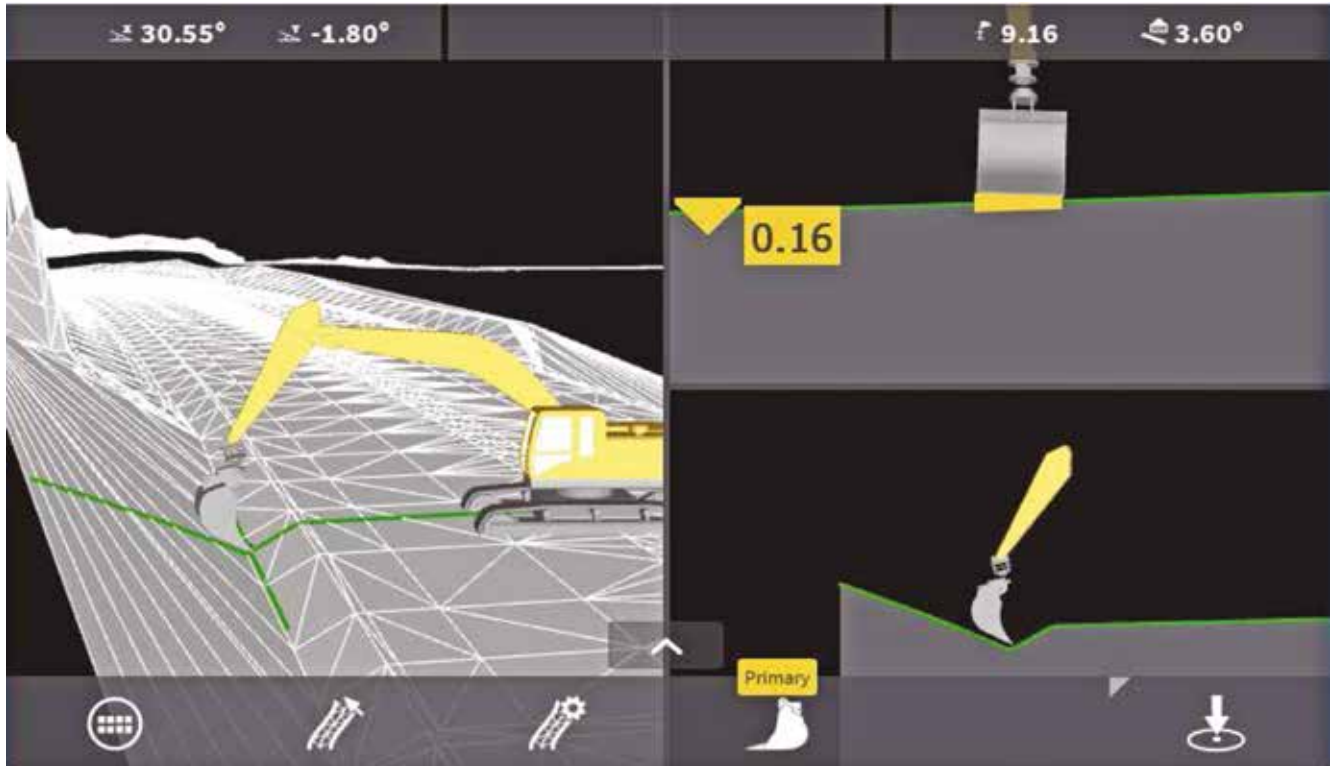
Fig. 2 – The program interface on the excavator operator's tablet. *Source:* Compiled by the authors.

by standard geodetic methods, thereby allowing to compare the current coordinates with the coordinates on the digital model and make the necessary corrections. This approach allows the machine to move freely around the construction site and at the same time form complex surfaces with high accuracy (Yu *et al.*, 2010; Wang *et al.*, 2016; Bender *et al.*, 2017).

The system is based on a 3D digital surface model (DSM), which is prepared in CAD programs for design (AutoCAD, DATAMINE) (Tanoli *et al.*, 2018). Then, the 3D DSM file is loaded into the computer on the excavator, having previously been processed to a continuous triangulation model (Floriani, & Puppo, 1995; Morris & Kanade, 2000; Soucy & Laurendeau, 1996) (fig. 2). Further, angle sensors and a GNSS receiver come into operation, which, together with external geodetic equipment, determine the position of the excavator bucket with a declared accuracy of 5-20 cm. (Antonovich, 2007; Gavrylenko,

2016; Mitrakhovich, 2016). The computer compares the data on the position of the bucket teeth and on the screen shows the offset relative to the project – according to the elevation of the ledge and the planned position in space.

To determine the position of the bucket teeth relative to the center of rotation of the body, all systems use the same algorithm, which is based on trigonometric calculations (Sing, 1995). To perform these calculations, the system needs to know the current angles of the boom elements, such as the boom itself, the arm and the bucket, as well as the distances between the axes of rotation of these elements (Bradley & Seward, 1998; Liu, Hasan & Yu, 2010; Vähä & Skibniewski, 1993). The angles of inclination in all control systems are determined by special angle sensors placed on all elements of the boom, and the distances are determined once during installation of the system and recorded in the system control panel for the correct configuration of the machine

(He, Hao & Zhang, 2008; Vähä & Skibniewski, 1993).

In prospect, when the excavator is operating, any system for changing the angles of the boom can calculate the correct position of the bucket relative to some initial position, that is, the system will calculate the vertical and horizontal movement of the bucket relative to the body (Koivo *et al.*, 1996; Korobkov, 2000). Positioning system body sensor not only determines the current roll and pitch of the machine, it also determines the angle of rotation of the body due to the integrated compass (Savenko, 2006). This feature serves to improve the accuracy of the system, as it complements the operation of satellite systems (gives the necessary redundancy) (Korobkov, 2000).

The positioning system of the bulldozer blade (fig. 3), designed to improve the efficiency of the earthmoving machine, in real time indicates to the operator of the bulldozer the current deviation from the design surface.

GEAM

GEORESOURCES AND MINING
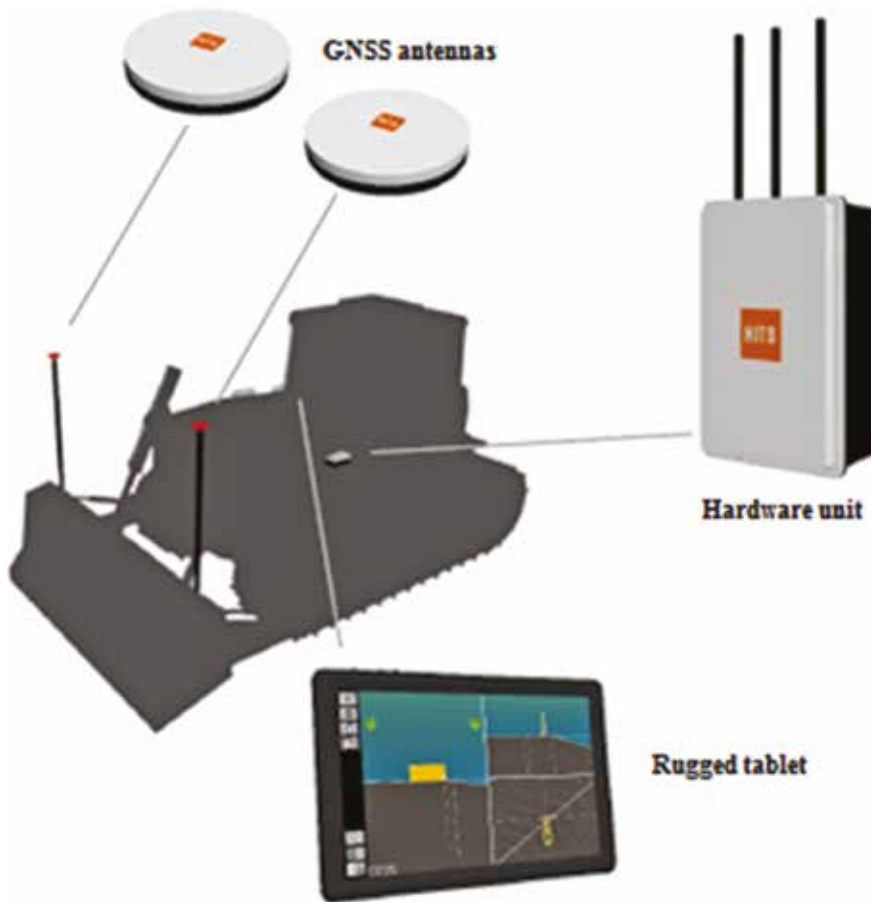
Fig. 3 – The structure of positioning system placement on the bulldozer. *Source:* Compiled by the authors.

the empirical level, the following will be applied: measurement and experiment.

The analogy method will be used in the study of scientific papers devoted to systems similar in construction.

The induction method is also used: we will calculate the accuracy characteristics using the same method due to their fundamental structural similarity for different models of excavators. The main part of the work consists of experimental studies.

This article describes the principles of construction and operation of automatic leveling systems and solves the issue of the accuracy of these systems. It is important to know this in order for the owners of production facilities to understand that the introduction of these technologies not only reduces the risks that arise during work, but also significantly increases the speed of work without losing accuracy.

The system consists of two GNSS antennas located on the bulldozer blade, a hardware unit and a protected tablet. The principle of operation of this system is simpler than that of an excavator, since it does not process measurements from angle sensors. Loading the design surface and unloading the DSM from the software does not differ from the system on the excavator.

Main applications: road construction, base vertical layout, dumps and landfills, preparatory work on large construction sites with complex profiles.

2. Materials and Methods

The work objective is to increase the efficiency of the mining surveying service in open-pit mining by introducing a positioning sy-

stem for mining equipment.

The main tasks of the study:
1) Evaluation of the accuracy of the positioning system as a set of components located on mining equipment;
2) Determination of mining surveying works that can be replaced by the introduction of positioning systems into production;
3) Formulation of recommendations on the use of mining machines to update digital models of technogenic structures of open-pits in real time and calculate the volume of production.

To solve the set tasks, basic trigonometric calculations and analysis of field data of various positioning systems are used. The methods at the theoretical level used in this work will be: analogy, mathematical modeling and induction. At

3. Results

3.1. Calculation of the accuracy of the positioning system for an excavator

We will calculate the accuracy of positioning the position of the excavator bucket teeth. To do this, we will lay an imaginary (improvised) polygonometric course on the excavator (fig. 4). The stroke will go from the GNSS antennas directly to the bucket teeth.

Let's start the calculations with satellite antenna fixed on the machine using vibration-resistant masts at the rear of the excavator body. Their positioning accuracy is equal to the accuracy of GNSS equipment: 20 mm in plan and 50 mm in height (Korobkov, 2000; Voroshilov, 2007).

The stroke is laid according to the

8

Agosto 2023
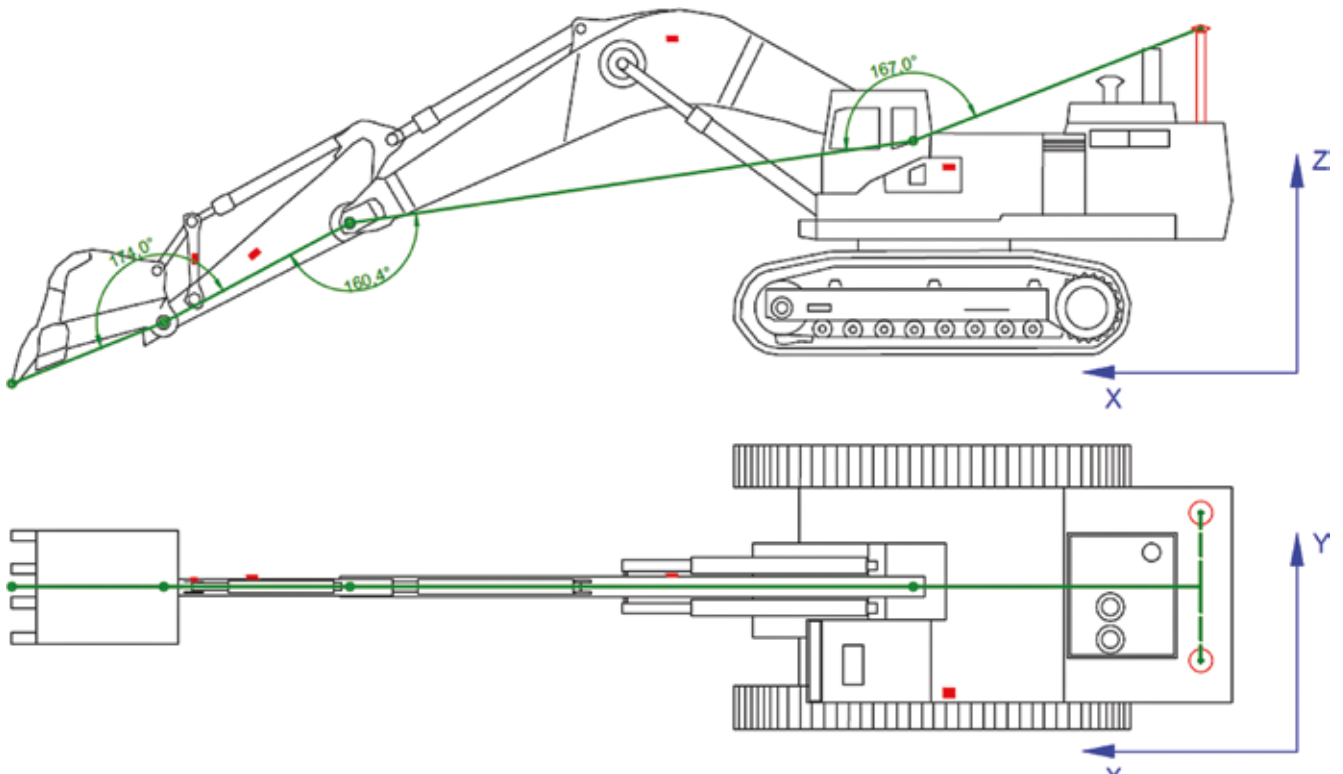
Fig. 4 – Excavator stroke (green) and system components (red). *Source:* Compiled by the authors.

following sequence of points: satellite antennas, rotation axis of the excavator boom, rotation axis of the excavator arm, rotation axis of the excavator bucket, bucket teeth.

Tilt angle sensors are located on each side of the stroke. For the body, boom, arm and bucket, as a rule, the same type of two-axis sensors with the declared dynamic accuracy are used 0,1° (Luczak, 2006).

All side lengths are known in advance and determined based on the documentation for the excavator and the bucket used. Accuracy calculations will be made according to the simplified formula 1:

$$\sigma = \sin{(0{,}1°)} \cdot L \qquad (1),$$

where
- σ is the error at the opposite point of the element of the working body,
- 0,1° is the declared accuracy of the tilt sensor,
- *L* is the length of the element of working body

The operation of the bucket tilt sensor should be considered in more detail. The impossibility of installing the sensor directly on the bucket is explained by two reasons: firstly, due to the high probability of its mechanical damage, and secondly, due to the fact that several types of buckets are often installed on the same excavator (Koivo *et al.*, 1996). As a result of these reasons, the sensor is mounted on the so-called "thrust". In this case, in order to find the angle of rotation of the bucket relative to the arm, it is necessary to find the relationship between the angle of rotation of the "thrust" and the angle of rotation of the bucket. For this, peculiar "epures" of the movement of these elements are built. (Koivo *et al.*, 1996; Vähä & Skibniewski, 1993) (fig. 5). Next,
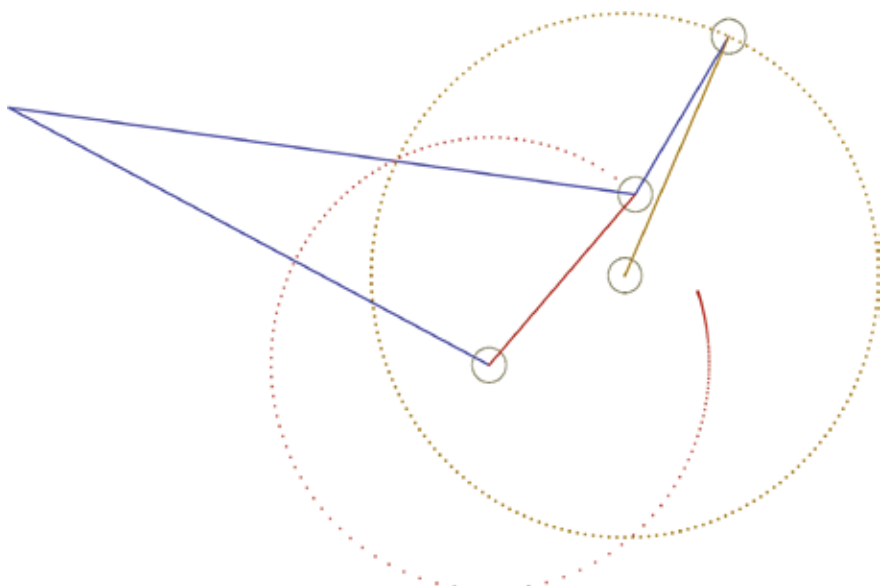
Fig. 5 – "Epure" of the bucket movement. *Source:* Compiled by the authors.

the trend line closest to the dependence is selected. In this case, it is a polynomial of the sixth degree (fig. 6). Since the value of the approximation reliability is equal to one throughout the dependence, we can assume that the sensor is allegedly installed on the bucket itself. Therefore, it becomes possible to calculate the accuracy on the bucket teeth. This dependence is calculated for each of the buckets and stored in the system memory.

Table 1 shows the calculation of the accuracy of determining the coordinates of the last stroke point (bucket teeth).

Thus, without taking into account the accuracy of determining the position of satellite antennas, the error on the bucket teeth is 36 mm. In order to take into account all the working conditions of the excavator, rounding up to 50 mm was made.

So, taking into account the error in determining the position of satellite antennas, we get the following indicators: the error in determining the planned position is 70 mm; the high-altitude position is 100 mm.

Bulldozer positioning systems are equipped with fewer sensors, so better accuracy can be expected.

3.2. Implementation example

An example of the introduction of this technology in open-pit mining is the work at the gold ore production of "Svetloye" LLC, the Emmi quarry (Khabarovsk Krai).

According to the results of comparing the contours of grade planning and the actual mining of an ore block of complex geometric shape, in the slope part of the open-pit, the largest deviation from the project was 20 cm (fig. 7-9). In the figures, the design contour is shown in red, and the actual one in gray.

During the period of work (Mar-
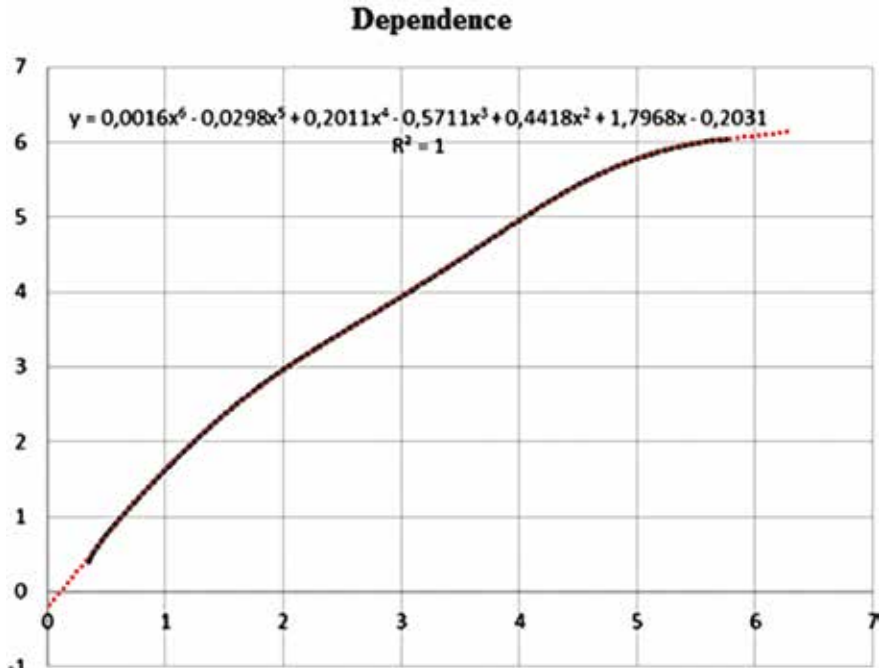
Fig. 6 – Dependence of the bucket rotation angle on the thrust rotation angle in radians. *Source:* Compiled by the authors.

$$y = 0{,}0016x^6 - 0{,}0298x^5 + 0{,}2011x^4 - 0{,}5711x^3 + 0{,}4418x^2 + 1{,}7968x - 0{,}2031$$
$$R^2 = 1$$
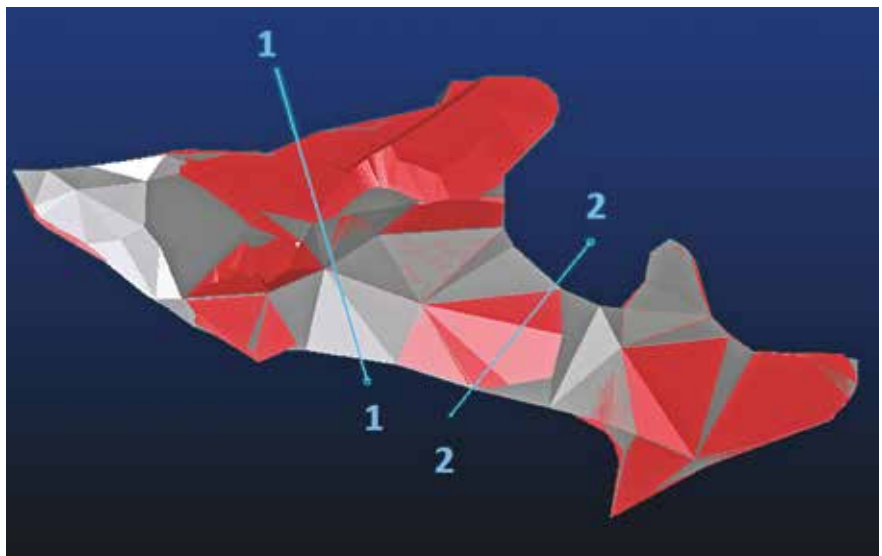
Fig. 7 – Deviations from the project during grade planning (axonometry). *Source:* Compiled by the authors.

Tab. 1 – Calculation of the accuracy of determining the coordinates of the last stroke point (bucket teeth). *Source:* Compiled by the authors.

Stroke part	Stroke part length (mm)	Angular error (degrees)	Error (mm)
antennas – high boom axle	5060		9
high boom axle – high arm axle	9340		16
high arm axle – high axis of the bucket	3450	0,1	6
high axis of the bucket – bucket teeth	2680		5
	Sum		36

ch-April 2019), using bucket positioning systems at the Emmy quarry, 12 sectors were mined with deviations of +/− 20 cm, despite the fact that part of the mining was carried out at the initial stage of quarry development – in zones with geological disturbances and loose deposits. These factors always influence the quality of mining operations. The system made it possible to mine blocks of complex geometric shape with minimal losses and impoverishment. Comparison of grade planning with actual mining using a positioning system is presented in Table 2.

This solution also made it possible to form the sides of the quarry to the final position with minimal

Tab. 2 – Comparison of grade planning with actual block development. *Source:* Compiled by the authors.

Grade planning							
Sector/Block	Ledge, m		Merchantable ore, tons	AU, g/t	AU, kg	Losses, %	Dilution, %
2S-12.03-C2	630	625	6210	2.30	14.3	2.0	8.0
Actual mining							
Sector/Block	Ledge, m		Merchantable ore, tons	AU, g/t	AU, kg	Losses, %	Dilution, %
2S-12.03-C2	630	625	6715	2.32	15.6	1.6	6.6

Fig. 8 – Deviations from the project during grade planning (section 1-1). *Source:* Compiled by the authors.
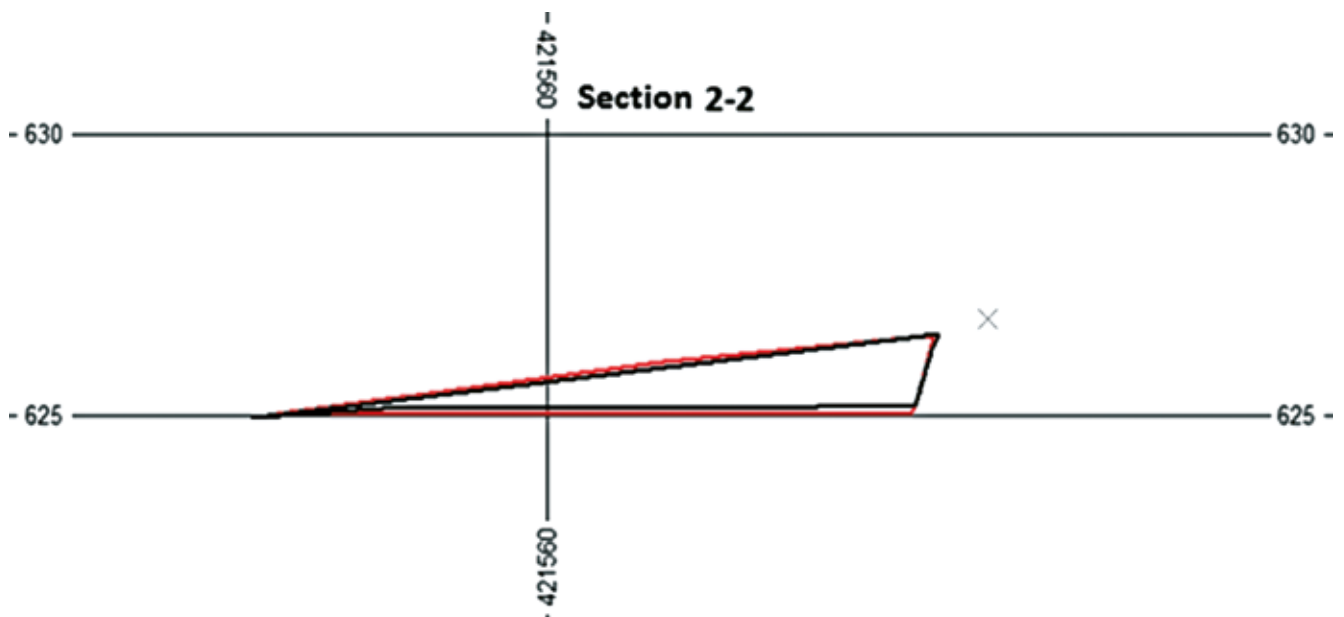
Fig. 9 – Deviations from the project during grade planning (section 2-2). *Source:* Compiled by the authors.

deviations from the project. The tacheometric survey of the sides of the quarry showed that on those sides where the excavator equipped with the positioning system was used, the design slope angle of 65° was maintained, and where the excavator worked without the high-precision bucket positioning system (HPBPS), the angle was 58° (fig. 10).

In this case, the solution was applied solely to follow the mining project, but there was no use of the system as a survey unit.

4. Discussion

It is worth noting that there were more experiments that show an increase in performance when using these solutions. For example, in one such study, the systems show an 81.12% increase in productivity and an accuracy of ± 2.1 m³ compared to traditional methods (Park *et al.*, 2021).

In addition, the use of positioning systems greatly reduces the risk of damage to underground utilities by the excavator bucket (Tanoli *et al.*, 2019).

At the moment, most manufacturers of equipment positioning systems have solutions that allow collecting information about the operation of each of the machines operating in the field into a single control center on the server. This allows to monitor the position of mining operations in real time in all areas at once and thus update the graphic information.

In many open pits, the navigation systems of mining machines can use GNSS receivers as long as enough satellites are in "visibility zone". However, as the excavation deepens, the visible part of the sky narrows, and with it the number of satellites tracked by the receiver decreases, the geometry of their configuration worsens, which leads to a deterioration in the accuracy of determining the coordinates of mining machines and a

decrease in the availability of navigation data. In conditions of limited satellite visibility, the use of satellite positioning systems (and with them the navigation systems of mining machines) becomes impossible, forcing the mining enterprise to turn to less efficient methods, such as geodetic measurements using electronic total stations. As a result, the operation of mining machines slows down or even temporarily stops, which leads to a deterioration in the efficiency of the enterprise and a decrease in production volumes. But already now there are several solutions to the "closed sky" problem. These include the definition of a "closed" sky using geographic information systems and the use of inertial solutions in the development of positioning systems (Freeland *et al.*, 2012; Sun *et al.*, 2017).

Locata has also developed and patented a new wireless synchronization technology called TimeLoc. The technology allows, without using atomic clocks, to synchronize all devices included in the Locata network with an accuracy of about one nanosecond. It is this development that is key, and thanks to it LocataNet (the ground network of Locata devices) is similar in capabilities to the GPS system placed on the ground. Unlike GNSS systems, LocataNet provides highly accurate positioning without the need for additional reference base stations or additional corrections. The transmitters, called LocataLite, transmit Locata system signals from special towers, reproducing the capabilities of the satellites locally. For example, the manufacturer Topcon called this technology SiteLink. This solution allows to receive data from any performer or machine to a central communication center and transmit this and other information to all participants in the work on the construction site. Equipped
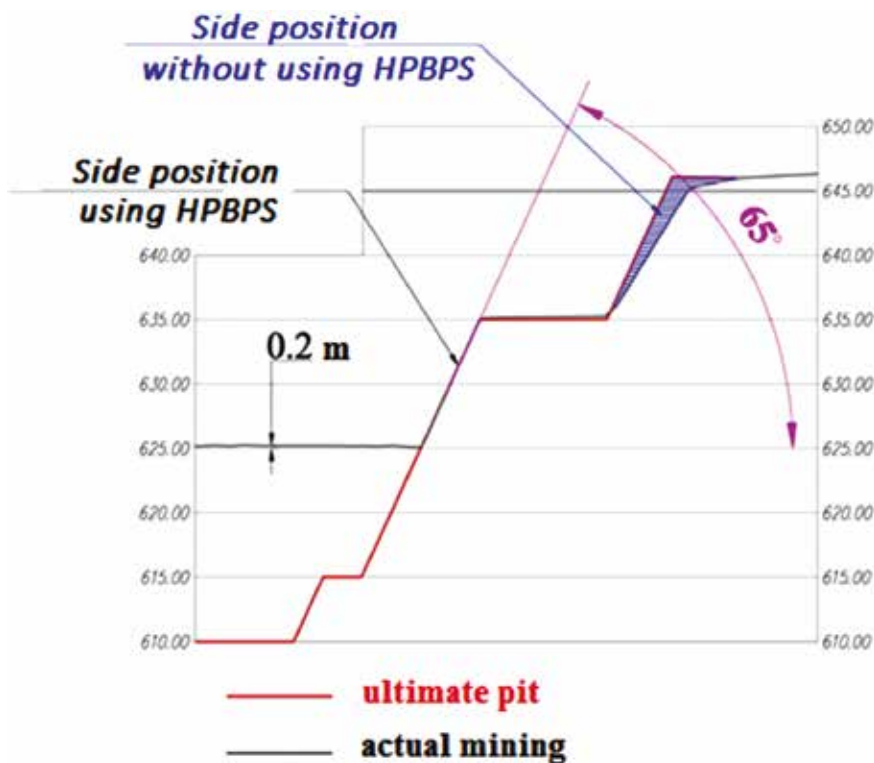
Fig. 10 – Formation of the side of the quarry to the final position – section along the side. *Source:* Compiled by the authors.

with a positioning system and a SiteLink controller, each piece of construction equipment can send real-time information about its position and the progress of the current project, as well as quickly receive updated models to ensure non-stop operation (Barnes *et al.*, 2007; Rizos, Gambale & Lilly, 2013).

5. Conclusion

The resulting accuracy of determining the coordinates on the teeth of the excavator bucket allows the surveying department to solve the following tasks: updating the digital surface model; ensuring accurate compliance with the mining project (face position and slope angle); ensuring "entrance" to the ore zone with industrial content and "exit" from it.

Excavators at the quarry perform not only the loading of the exploded rock mass into dump trucks, but also the scaling of the face and bringing it to the design position after the explosion. To this end, the operator is forced to drive the bucket over the entire face area. Taking advantage of the fact that a digital model of the surface is loaded into the excavator, which is updated when the bucket crosses it, it is possible to carry out operational monitoring of the state of mining. The accuracy of this model will correspond to the survey accuracy required for plans at a scale of 1:500 (Tselovalnikov, 2006).

At the access of mine workings to the ore body and exit from it, blast holes are drilled at some distance from its boundary in order to prevent the impoverishment of the useful component. After an explosion, the face often remains at some distance from the design contour. The task of the excavator is to remove the rest of the

mountain range. When using the system for determining the spatial position of the bucket, there is no need for mine surveying support of this stage of work, namely, the removal of pegs on the upper edge of the boundary of the ore deposit.

At the moment, most manufacturers of equipment positioning systems have solutions that allow collecting information about the operation of each of the machines operating in the field into a single control center on the server. This may allow real-time monitoring of the position of mining operations at once in all areas and thus update the graphical information. During the work on the quarry, the blade of the bulldozer clearing the ledge will cross the digital surface model. Thus, information about the current state of work will be updated in real time. The maximum benefit from this technology can be achieved by equipping every mining machine with a positioning system. As a result, the mining surveying department will always have an up-to-date version of the mining situation.

Mining surveying plans, in most cases, do not differ in the richness of topological objects. The main objects on them are elements of disturbed relief (slopes and ledges). For software environments, it is not difficult to translate the DSM into a plan with drawing dashed lines on slopes. This can already be done by some amateur utilities for Autodesk products. The mine surveyor will only have to remove communications and buildings in order to put them on the plan.

Based on the foregoing, we can conclude that the use of automated positioning systems allows you to set the position of the working body of the mechanism at any point in the mining operation in a fully automatic mode. This makes it possible to facilitate work on mine surveying support for the construction of facilities

due to the absence of the need to carry out work on the thickening of SCN in the bottomhole space, carrying out and fixing the axles. The tasks of surveyors in this case are: creation and maintenance of a sufficient number of base GNSS stations, timely provision of positioning systems with the necessary data and control of the progress of work. Also, the efficiency and accuracy of volume calculation increases, since the overlay of the previous DSM on the current DSM allows to immediately calculate the difference in volume. Positioning systems allow to increase the pace of work and labor productivity by reducing the number of operations required to achieve the design surface elevations.

The ability to remotely download a mining project to the controller of each specific machine eliminates equipment downtime and reduces the time to complete quarterly, monthly and ten-day mining plans.

It should also be noted that the introduction of positioning systems will improve the safety level of mining operations by eliminating the presence of personnel in potentially dangerous areas of the face during accompanying works.

References

Agaguena, A., Chishegorov, D., Ivanov, S. & Mikhailov, A., (2021). *Influence of the main operational factors on the working capacity of a mining hydraulic excavator: International Conference on Innovations, Physical Studies and Digitalization in Mining Engineering*. Saint-Petersburg, Russian Federation. https://doi.org/10.1051/e3sconf/202132600007

Antonovich, K.M., (2007). *Use of satellite radio navigation systems in geodesy. (PhD thesis)*. Russia, Novosibirsk: Siberian State Geodetic Academy.

Barnes, J., Lamance, J., Lilly, B., Rogers,

I., Nix, M. & DeBeers, A., (2007). An integrated Locata & Leica Geosystems positioning system for open-cut mining applications. In *Proceedings of the 20th International Technical Meeting of the Satellite Division of the Institute of Navigation (ION GNSS 2007)*, 1661-1668.

Batalina, S.A., & Ilemkova, N.R., (2013) Control systems for earth-moving equipment of the third generation. *Youth and science. Proceedings of the International Scientific and Practical Conference of Students of the Nizhny Tagil Technological Institute (branch), Ural Federal University,* 61-65.

Bender, F.A., Göltz, S., Bräunl, T. & Sawodny, O., (2017). Modeling and offset-free model predictive control of a hydraulic mini excavator. *IEEE Transactions on Automation Science and Engineering*, 14(4), 1682-1694. DOI:10.1109/TASE.2017.2700407

Blishchenko, A.A., (2020). Use of geodetic instruments in open-pit mining, the trend of using of unmanned technologies. *Colloquium-journal*, (14 (66)), 46-47. DOI: 10.24411/2520-6990-2020-11902

Bradley, D.A. & Seward, D.W. (1998). The Development, Control and Operation of an Autonomous Robotic Excavator. *Journal of Intelligent and Robotic Systems* 21, 73-97. https://doi.org/10.1023/A:1007932011161

Dudnik, A.E., Govorukhin, M.G. & Tupoleva, G.K., (2018). Modern use of 3D-leveling technologies. *Modeling and analysis of complex technical and technological systems*, 122, 33-34.

Floriani, L.D., & Puppo, E. (1995). Hierarchical triangulation for multiresolution surface description. *ACM Trans. Graph.*, 14, 363-411. DOI:10.1145/225294.225297

Freeland, R., Buschermohle, M., Wilkerson, J., & Glafenhein, E., (2012). RTK Mobile Machine Control-Assessing Partial Sky Blockage with GIS. *Applied Engineering in Agriculture*. 28. 703-710. DOI: 10.13031/2013.42421

Gavrylenko, D., (2016). Influence of distance between base stations and satellite receiver on accuracy of coordinate measurement in RTK-mode. *Bulletin of Kharkiv National University of Municipal Economy named after A.N. Beketov*, 33, 33-35.

He, Qh., Hao, P. & Zhang, Dq., (2008). Modeling and parameter estimation for hydraulic system of excavator's arm. *J. Cent. South Univ. Technol.* 15, 382-386. https://doi.org/10.1007/s11771-008-0072-1

Khvalev, P.S., Satyukov, A.B. & Orekhov, S.A., (2017) Information technologies for automatic leveling in road construction equipment. T*rends in the development of science and education*, 26-1, 32-34. DOI: 10.18411/lj-31-05-2017-11

Koivo, A.J., Thoma, M., Kocaoglan, E., & Andrade-Cetto, J. (1996). Modeling and Control of Excavator Dynamics during Digging Operation. Journal of Aerospace Engineering, 9, 10-18. DOI:10.1061/(ASCE)0893-1321(1996)9:1(10)

Korobkov, S.A., (2000) Estimation of the accuracy of the spatial position of a geodetic point. *Geodesy and cartography*, 26(1), 3-10.

Liu, Y., Hasan, M.S. & Yu, H.N., (2010) Modelling and remote control of an excavator. *Int. J. Autom. Comput.* 7, 349-358. https://doi.org/10.1007/s11633-010-0514-8

Luczak, S., Oleksiuk, W. & Bodnicki, M., (2006). Sensing tilt with MEMS accelerometers. *IEEE Sensors Journal* 6(6), 1669-1675. DOI: 10.1109/JSEN.2006.881433

Ministry of Transport (1978). Technological map. *Building-up of stringlines for the operation of machines of the DS-100 set on the construction of airfield bases (coverings)*. Entered into force in 1978. Ministry of Transport, Russian Federation.

Mitrakhovich, I.O., (2016). The system for determining the angles of orientation of objects in space based on the RTK method. *Bulletin of the Belarusian State University*, 313, 10-12.

Morris, D., & Kanade, T., (2000). Image-consistent surface triangulation. Proceedings *IEEE Conference on Computer Vision and Pattern Recognition*. CVPR 2000 (Cat. No.PR00662), 1, 332-338, DOI:10.1109/CVPR.2000.855837

Mustafin, M.G., & Tran Thanh Son (2018). Use of a topocentric rectangular coordinate system in solving engineering and geodesic problems. *Bulletin of Siberian State University of Geosystems and Technologies* 23(3), 21-22.

Park, S., Kim, J., Lee, S., & Seo, J.W., (2021). A Comparative Analysis of Automated Machine Guidance and Control Systems for Trench Excavation. *KSCE Journal of Civil Engineering*, 25, 4065-4074. DOI:10.1007/s12205-021-0159-x

Potiuchliaev, V.G., (2012). The calculation of accuracy of breaking the network using satellite navigation systems. *Journal of Mining Institute*, 199, 61-62.

Pugin, K.G. & Piramatov, W.A., (2017). Leveling systems in domestic technology. *Modernization and scientific research in the transport complex*, 1, 54-57.

Rizos, C., Gambale, N. & Lilly, B., (2013). Mine machinery automation using Locata-augmented GNSS. In *Proceedings of the ION 2013 Pacific PNT Meeting*, 463-469.

Sahapov, R.L., (2019). Satellite navigation management systems for learning dynamic models. *Innovations in Agriculture*, 1, 222-230.

Savenko, N., (2006). Accelerometers and gyroscopes for portable devices. *Modern electronics*, 6, 18-21.

Sing, S. (1995). *Synthesis of tactical plans for robotic excavation.* Pittsburgh, USA, Carnegie Mellon University.

Siukhin, A.A., Zverev M.V. & Balashov P.V., (2018). The systems of levelling used in construction of roads. *Virtual modeling, prototyping and industrial design*, 1, 253-259.

Soucy, M. & Laurendeau, D. (1996). Multiresolution surface modeling based on hierarchical triangulation. *Computer Vision and Image Understanding*. 63(1), 1-14.

Sun, D.I., Kim, S.H., Lee, Y.S., Lee, S.K. & Han, C.S., (2017). Pose and position estimation of dozer blade in 3-dimensional by integration of IMU

with two RTK GPSS. In *ISARC. Proceedings of the International Symposium on Automation and Robotics in Construction (Vol. 34). IAARC Publications*, DOI: 10.22260/isarc2017/0137

Tanoli, W.A., Seo, J.W., Sharafat, A., & Lee, S.S., (2018). 3D design modeling application in machine guidance system for earthwork operations. *KSCE Journal of Civil Engineering*, 22(12), 4779-4790. https://doi.org/10.1007/s12205-018-0309-y

Tanoli, W.A. & Sharafat, A. & Park, J. & Seo, J.W., (2019). Damage Prevention for underground utilities using machine guidance. *Automation in Construction*. 107. 102893. DOI: 10.1016/j.autcon.2019.102893

Tselovalnikov, V.G., (2006). The using satellite radio navigation systems in modern construction. *Journal of the Mining Institute*, 167. 1, 11.

Vähä, P., & Skibniewski, M.J. (1993). Dynamic Model of Excavator. *Journal of Aerospace Engineering*, 6, 148-158. DOI:10.1061/(ASCE)0893-1321(1993)6:2(148)

Voroshilov, A.P., (2007). *Satellite systems and electronic tacheometers in the construction work*: Textbook. Chelyabinsk, Russian Federation: AXWELL.

Wang, D., Zheng, L., Yu, H., Zhou, W. & Shao, L., (2016). Robotic excavator motion control using a nonlinear proportional-integral controller and cross-coupled pre-compensation. *Automation in Construction*. 64. 1-6. DOI: 10.1016/j.autcon.2015.12.024

Yu, H. & Liu, Y. & Hasan, M.S., (2010). Review of modelling and remote control for excavators. *International Journal of Advanced Mechatronic Systems*, 2(1-2), 68-80. DOI: 10.1504/IJAMECHS.2010.030850

Zubova, O.A., (2013). Application of modern automatic leveling systems in road construction. *Bulletin of Kazakh Leading Academy of Architecture and Construction*, 2, 22-23.

Design of torrential barriers

The rapid erosion of alpine valleys can be prevented by torrential barriers. For their design is crucial the thrust acting upon them due to earth and water pressures. From the evaluation of damage events and field investigations it can be inferred that often no water saturation and thus not the full hydrostatic pressure acts upon such barriers. The uncertainty associated herewith is reflected in various guidelines. The field observations can be explained by the structure of the backfill but also by the distribution of the water pressure. An empirical assessment of the loads on such structures is here proposed, which takes into account the probabilities of the individual events.

Keywords: *natural hazards, torrential barriers, water pressure, culverts.*

Robert Hofmann*
Simon Berger*

* University of Innsbruck, Unit for Geotechnical and Tunnel Engineering, Innsbruck Austria

Corresponding author:
robert.hofmann@uibk.ac.at

1. Introduction

When planning and dimensioning torrential barriers (also called consolidation dams), the distribution of the water pressure is of essential importance. It was heuristically determined until the Austrian code ONR 24802 [6] appeared in 2001. However, experience is very different in the several provinces of Austria. In 1973, a guideline for the dimensioning of torrential barriers was published in Switzerland [3]. In Austria, an investigation of the loads acting upon concrete and reinforced concrete torrential barriers was published in 1998 [2], where all types of structures (energy conversion structures and dams) were considered. The water pressure acting upon the barriers is not always the hydrostatic one. This article presents an attempt to realistically assess the thrust acting upon torrential barriers.

2. Function and construction of torrential barriers

Torrential barriers (fig. 1) have the task of consolidating the bed of a torrent [7]. This is achieved by reducing the flow gradient. The fluid retained by a torrential barrier can be pure water or a fluviatile mixture or a debris. Torrential barriers reduce the kinetic energy of this fluid. The reduction of the gradient through the formation of free overflows with conversion of the energy of the flow and the associated raising of the channel bottom cause the retention of solids and thus have a positive influence on the bedload balance. Since the torrential barriers reduce the flow velocity in torrents, they slow down erosion and the associated deepening of valleys. They thus contribute also to stabilising the valley flanks.

3. Typical damage to existing structures

3.1. Low torrential barriers

It is interesting to investigate to which extent damage on torrential barriers can be attributed to water pressure. Figures 2 to 5 show some observed damage to torrential barriers with heights up to 5 m. The damage was caused by earth pressure exerted by the slope (slope thrust damage type A and C), debris flow (damage type B) and erosion due to undercurrents and overspill of the barrier (damage type D). Despite the relatively large culverts in all torrential barriers, very little or no water discharge is visible –as contrasted to a large amount of water in the overspill. Despite small foundation widths and the tight lateral embedding of the wings, no damage due to earth and water pressure was obser-

If there are references to colour figures in the text, the articles are available in open-access mode on the site www.geam-journal.org

Fig. 1 – Types of torrential barrier.

ved. The backfilling of the barriers took place immediately after their completion with hardly permeable mixed grain material. Figures 2 to 4 show barrier wings damaged by slope thrust. Despite the strong water flow in the torrent, only small discharges are visible at the culverts (figs. 2 and 4). With

damage type B (fig. 3), the wing of the torrent barrier was destroyed by the debris flow. The lateral embedding and thus a lateral spread of the load to the wing was no longer possible. Also in this case, the failure was not caused by the static earth and water pressures but by dynamic effects from the

torrent. Presumably due to locally more permeable zones in the sedimentation body, internal erosion has occurred in damage type D. The damage was caused by a large number of rock blocks. The floor discharge has wiped out the full embedding of the wing. However, the high local discharge in the se-
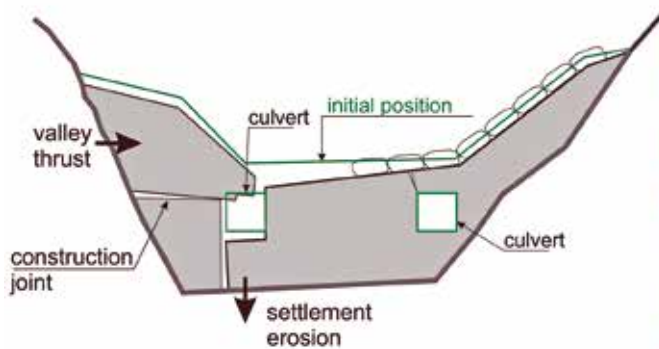
Fig. 2 – Damage pattern A.
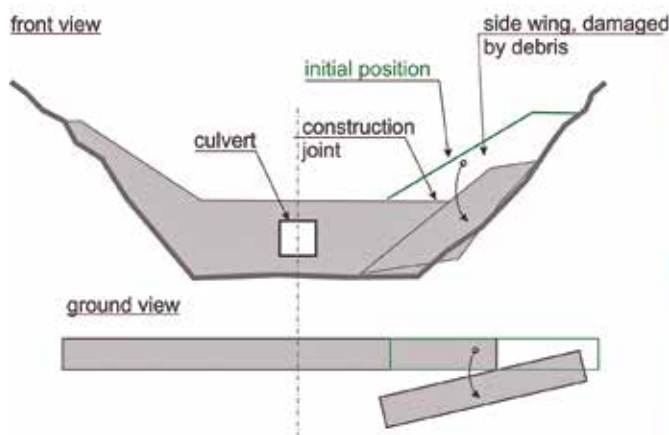
Fig. 3 – Damage pattern B.
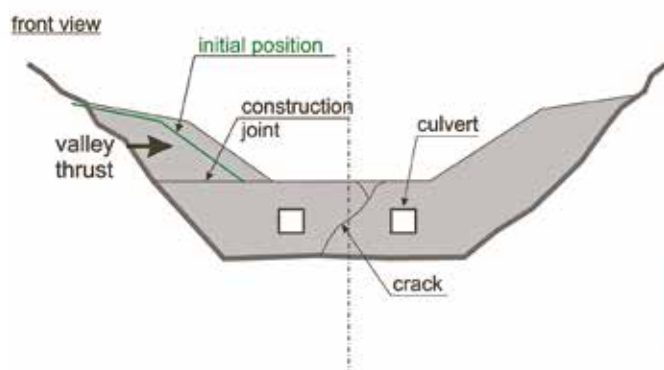
Fig. 4 – Damage pattern C.
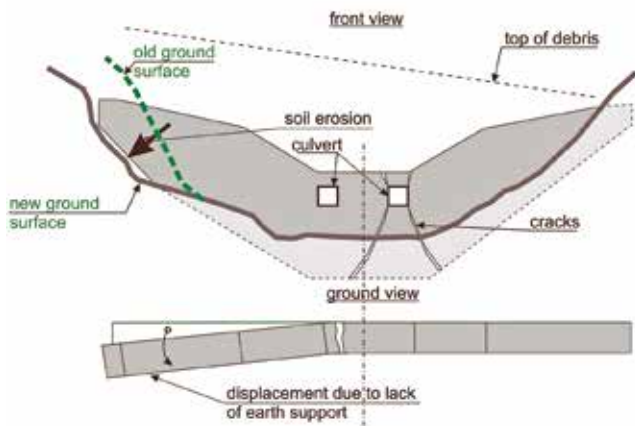
Fig. 5 – Damage pattern D.

dimentation body and in the torrent, also in this case, did not lead to any significant leaks from the culverts.

3.2. High torrential barriers

As an example are described the water conditions behind a torrent dam completed in 1954 and immediately backfilled (Figures 6 and 7), consisting of a sandwich construction with two exterior mortarized stone layers and a backfill with slope debris. The backfilling was carried out with slightly permeable mixed grain phyllites with a fine grain content between 12 and 28%. In 2018, six horizontal boreholes with a diameter of 46 mm were drilled through the structure —having a total height of 23.5 m— in order to draw conclusions about a possible water pressure. Very small amounts of water have been observed in the orographically left wing (fig. 7). It should be noted that the boreholes closest to the crown showed the smallest amounts of water and the culvert openings generally showed varying water discharge. The orographically right wing showed significantly higher amounts of water than the left wing. In a core drilling behind the left wing (axis E, Figure 7) the groundwater level was detected 12 m below the barrier crown. The only damage observed at this very

Fig. 6 – Torrential barrier of 23.5 m height.
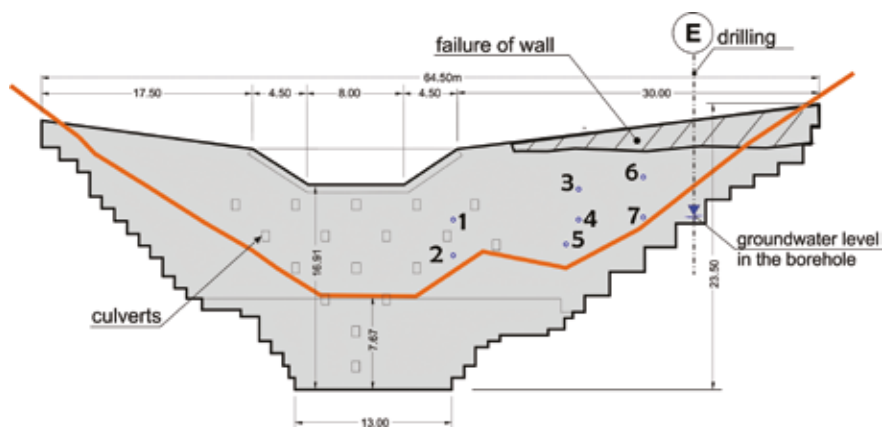
Fig. 7 – Torrential barrier of 23.5 m height. Boreholes 1, 2 and 4: dry; borehole 3: slight water discharge, borehole 5: discharge of 0.12 l/s; borehole 6 and 7: discharge of 0.05 l/s.

slim construction (wall thickness 2.0 to 2.5 m at the boreholes) with relatively low internal load-bearing capacity and ductility (air-side and earth-side stonewalls with backfill) was a displacement of the upper left wing to a maximum height of 2 m (fig. 7). The observed damage and the water leaks from the culverts as well as the boreholes

through the barrier and the elevation of the groundwater level in the borehole allow the conclusion that the backfill was not water saturated and therefore no water pressure was acting. The permeability of the various backfill layers, on the other hand, had a strong influence on the water pressure distribution behind the structure. A full hydrostatic water pressure can therefore be rather excluded. Field investigations (fig. 8) at an old uncovered 6 m high dam showed, indeed, that the backfill was relatively dry. Below the muddy bed there was a muddy, sandy gravel, which was suitable for installation and compaction. This can be explained as follows: The water in the torrent is either permanently in motion, or – as in many case – the torrent discharges only a small part of the annual water. The phases of the water flow in connection with the low permeability of the torrent debris are not sufficient to saturate the backfill.

4. Water pressure

4.1. Basic considerations

If the supported soil is water-saturated, the effect of culverts on the distribution of earth and water pressures is here investigated.

Fig. 8 – Uncovered torrential barrier Toedterbach with outlets.

In the literature [1] different approaches to the water pressure on torrential barriers can be found. The static water pressure on the structure can be reduced due to underflow and by the culverts, according to the specifications for the dimensioning of torrential barriers, concrete and reinforced concrete [3]. However, there is not mentioned that the reduction of the water pressure leads to an increase in the earth pressure due to the drag force. The reduction of the water pressure can be estimated from Figure 9 with 5 to 10% [3].

The state of the art for the design of the torrential barriers and in particular for the hydrostatic water pressure approach is described in ONR 24801 [8] and ONR 24802 [6]. Contrary to a possible underflow of the structure, the culverts are not taken into account. The water pressure in the backfill must be taken into account as in conventional retaining structures, see Figure 10 with

- $W_{s,ow}$: static water pressure backwater, crown,
- $W_{B,ow}$: static water pressure backwater, foundation,
- $W_{B,uw}$: static water pressure frontwater, foundation,
- WS: bottom water pressure.
- e: earth pressure
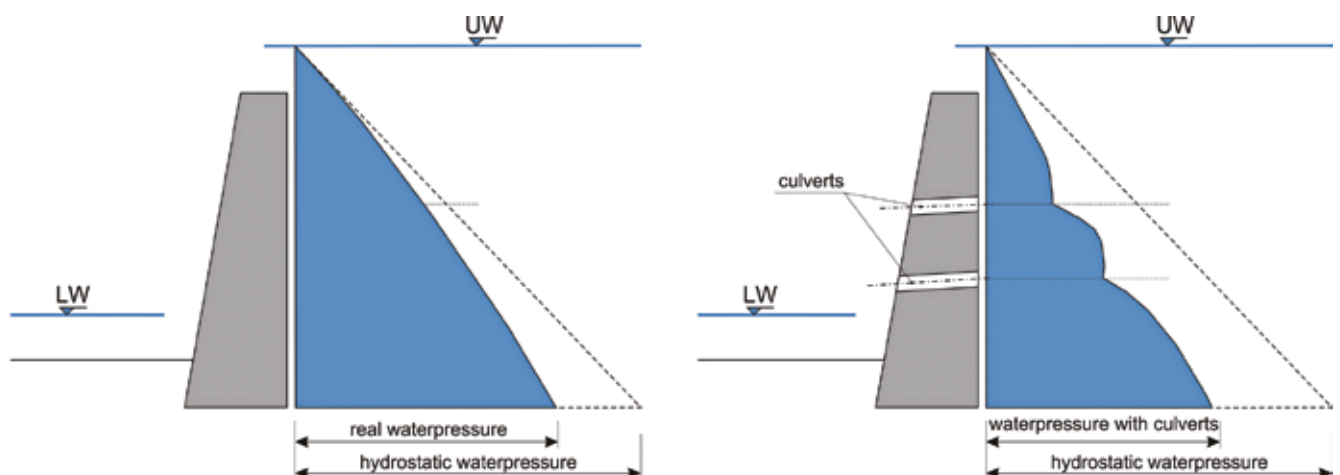
Fig. 9 – Water pressure acting upon torrential barrier without (left) and with (right) outlets [2].

4.2. Effect of culverts

4.2.1. Basic principles

Boreholes or openings (culverts) in torrential barriers, intend to reduce i.e. to relieve the water pressure. But even if the pore water pressure is reduced as a result, a large part of the thrust remains, which is then exerted upon the supporting structure by the drag force via the grain skeleton [4]. We consider a retaining wall which, in addition to earth pressure, is also loaded by water pressure and is provided with a culvert (fig. 11). Of course, this opening is designed so that no fines can be washed out (e.g. protected by a filter). We consider equilibrium of the horizontal effective stresses along the horizontal axis *x*:

$$\frac{\partial \sigma'_{xx}}{\partial x} + \frac{\partial \tau_{yx}}{\partial y} = b_x \qquad (1)$$

It makes sense to assume that the principal stress trajectory runs approximately horizontally (this was confirmed by FE calculation of the potential behind a barrier, which results in an almost horizontal drag force, see Figure 12). Therefore $\tau_{yx} \approx 0$ and therefore also applies: $\partial \tau_{yx}/\partial y \approx 0$. The horizontal volume force b_x results from the hydrodynamic drag. As is well known, this amounts to $-\gamma_w h$, where h is the energy height. So we can write:

$$b_x = -\gamma_w \nabla h = -\gamma_w \nabla (z + \gamma_w) =$$
$$= -\nabla p = \frac{\partial p}{\partial x} \qquad (2)$$

Thus, the equilibrium condition in the horizontal direction reads:

$$\frac{\partial(\sigma'_x + p)}{\partial x} = 0 \qquad (3)$$

hence

$$\sigma'_x + p = \text{const} \qquad (4)$$

along the horizontal *x*-axis. This means that a decrease of water pressure is counteracted by an
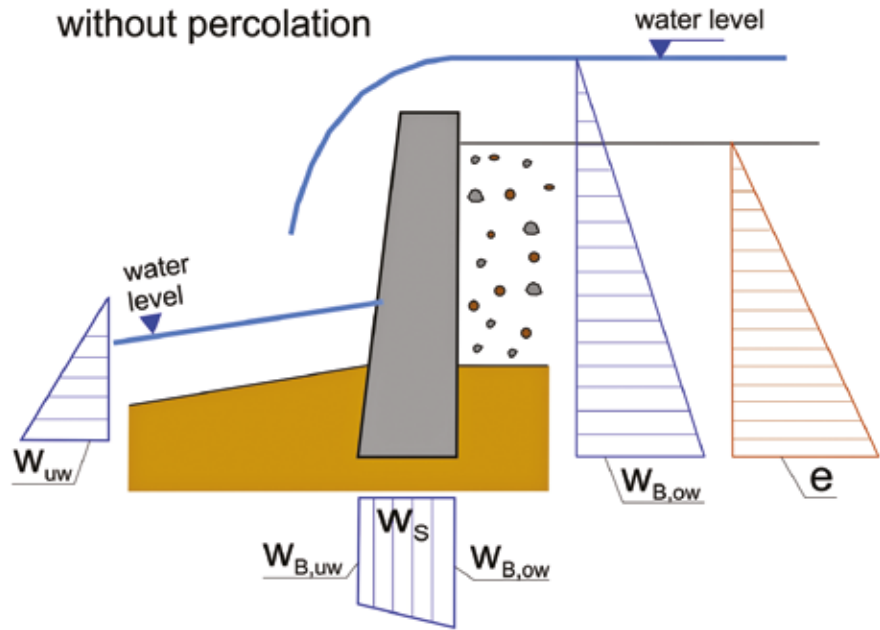
Fig. 10 – Water pressure distribution according to ONR24802. The names of the variables are taken from ONR 24802.
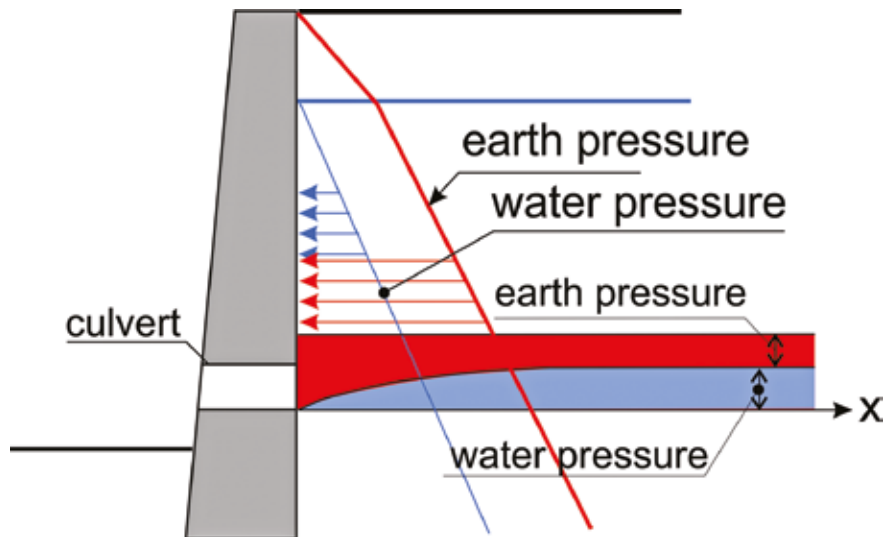
Fig. 11 – Earth pressure and water pressure acting upon a torrential barrier with a culvert.

increase of effective stress in the grain skeleton. Let us look at the conditions along the *x*-axis (fig. 11): With increasing distance from the barrier, the opening gets less noticeable, the 'undisturbed' geostatic stress distribution and the hydrostatic water pressure prevail. The further you go to the left, the more the water pressure decreases, up to the value 0 directly at the opening, and accordingly the horizontal effective stress increases. The total load however remains unchanged. Hence, the culvert

does not provide any water pressure relief for the retaining wall unless it affects the groundwater level in the backfill. However, this should not occur with impermeable soil or with sufficient water supply.

4.2.2. Numerical comparison calculations

The distribution of the water pressure behind a torrential barrier Leonhardsbach, Tirol, Austria (fig. 12a) with and without culverts

was calculated numerically with the OPTUM CE Program OPTUM G2 (fig. 12b). The torrential barrier has a total height of about 6.5 m (1.5 m backfill downstram; left hand side in Fig. 12b). The culverts have diameters about 0.4 m.

The numerical results depend on the size of the area under consideration and the associated boundary conditions. The calculations with the FE method (fig. 12b) provide a resulting horizontal load of 227,5 kN/m (with two culverts evenly distributed over the height and without culverts) for a 6,5 m high barrier. Fig. 12b shows the flow in the lower area which acts upon the grain skeleton and thus also increases the earth pressure. As already shown in 4.1, the resulting water pres-

Fig. 12a – Uncovered torrential barrier Leonhardsbach with culverts.

sure is reduced, but the simultaneous increase in earth pressure has the same magnitude and thus the two effects cancel each other.

In total, the effect on the barrier with two doles without additional measures (see section 4.3) is the same as without culverts.
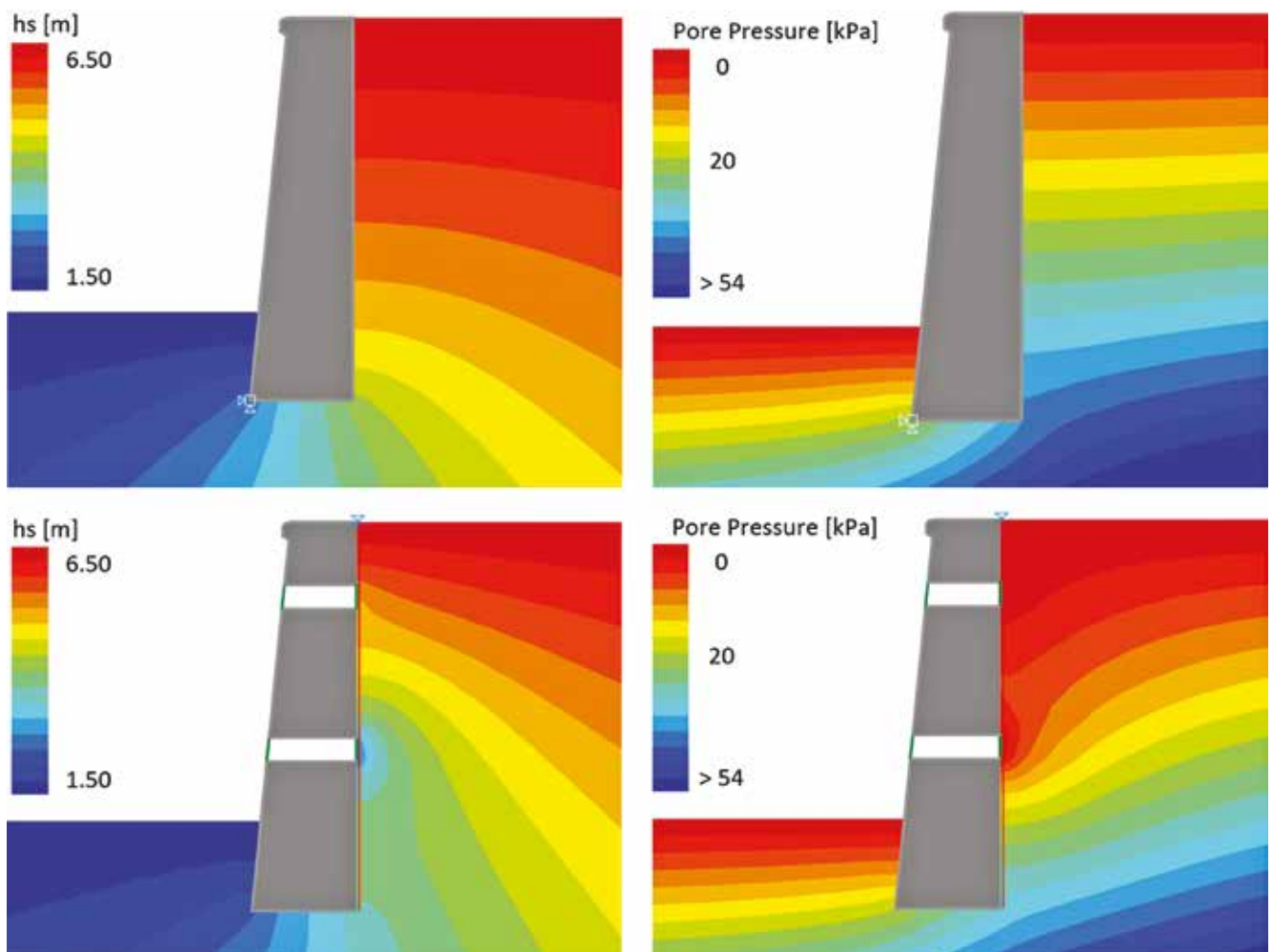
Fig. 12b – Distribution of energy height and water pressure behind a torrential barrier with (Fig 12b. below) and without culverts (fig. 12b above) with $k_x = k_y = 1 \times 10^{-5}$ m/s.
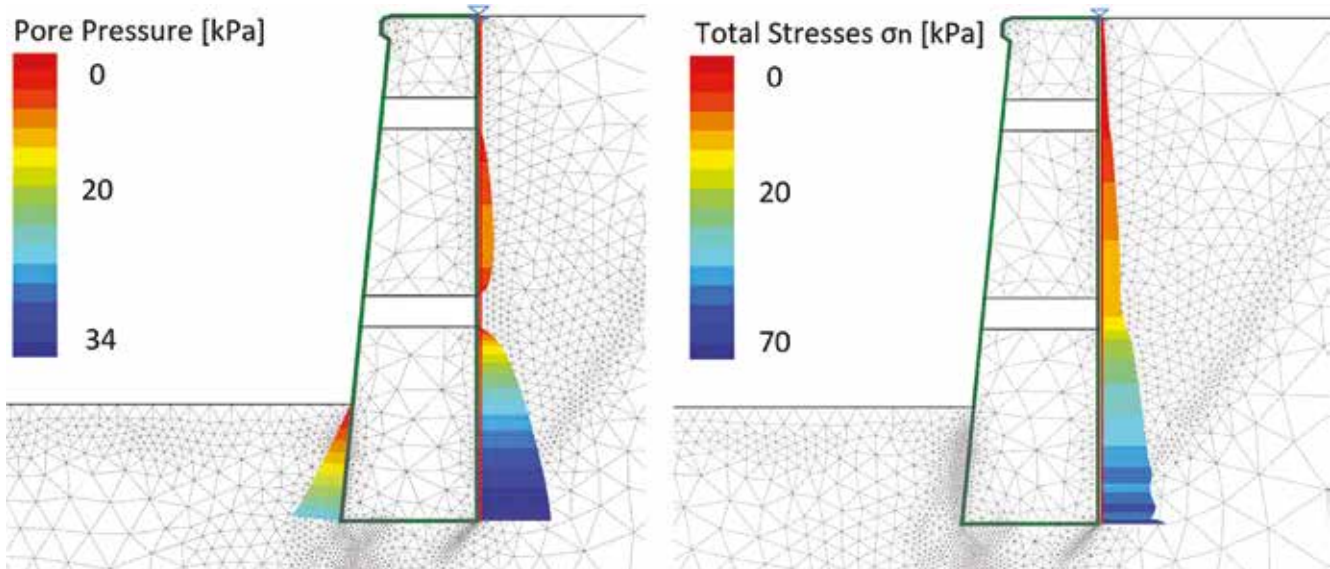
Fig. 12c – Distribution of total pressure (kN/m^2) and water pressure behind the torrential barrier with culverts (friction angle φ = 42° and saturated unit weight of the backfill γ$_r$ = 12 + 10 = 22 kN/m^3).

The numerical calculations give a maximum total stress of 71.0 kN/m² (fig. 12c) and thus a horizontal load of 227.5 kN/m (equation 5).

$$E_{k,A3} = 70,0 \cdot 6.5 \cdot \frac{1}{2} = \\ = 227.5\,\mathrm{kN/m} \qquad (5)$$

4.3. Comparison of the effects of different drainage systems

The importance of the various distributions of water pressure is shown by four examples for the torrential barrier Leonhardsbach (fig. 12a and 15):

1. Backfilling unsaturated (earth-moist)
2. Full water pressure
3. Drainage in the slip surface
4. Drainage immediately behind the barrier

Case 3 may appear somewhat artificial, but is possible in case of a special structure of the backfill.

4.3.1. Thrust without drainage (case 1)

It is assumed that a sealing layer is present in the bottom of the stream so that the backfill is not water-saturated. In this case, the loading on the barrier results from the earth pressure calculated with the moist unit weight γ = 21 kN/m³. With a friction angle φ = 42° (resulting in the active horizontal earth pressure coefficient K_{ah} = 0.198) and a wall friction angle δ = 0°, the horizontal component of the earth pressure reads (fig. 13a):

$$E_{k,1} = R = \frac{1}{2} \cdot \gamma H^2 K_{ah} = \\ = 1/2 \cdot 21 \cdot 6,5^2 \cdot 0.198 = \\ = 87.8\,\mathrm{kN/m} \qquad (6)$$

4.3.2. Thrust without drainage, backfilling water-saturated (case 2)

In case 2, the sedimentation body is completely water-saturated and the design water level is assumed to be at the level of the backfill surface. This case corresponds in principle to the specifications of ONR 24801 [8] and ONR 24802 [6]. The load upon the wall with active earth pressure and water pressure is obtained with the buoyant unit weight γ' = 12 kN/m³ and the full hydrostatic water pressure. The active earth pressure is E_h = 50.2 kN/m, the water pressure is W = 211.2 kN/m, and thus the resulting force reads (fig. 13b):

$$E_{k,2} = 1/2\gamma' H^2 K_{ah} + 1/2\gamma_w H^2 = \\ = 1/2 \cdot 12 \cdot 6.5^2 \cdot 0.198 + \\ + 1/2 \cdot 10 \cdot 6.5^2 = \\ = 50.2 + 211.2 = 261.4\,\mathrm{kN/m} \qquad (7)$$

4.3.3. Thrust in case of inclined drainage (case 3)

According to Lamb & Whitmann [5], the resulting load is reduced for a retaining wall with a design water level at the ground surface of the backfill by considering an inclined drainage over a low permeability soil layer. For the example considered (case 3), it was assumed that the drainage is located on a soil layer inclined at ϑ = 45° + φ/2 = 66° (fig. 14a). With a vertical flow through the sedimentation body, the vertical downward drag force results in S = iγ_w with i = 1. This case is a rather academic example, but still possible, as shown in Figure 14a.

In a downward water flow (fig. 14a), no water pressure builds up, but the earth pressure is proportional to the saturated unit weight of the backfill γ$_r$ = 12 + 10 = 22 kN/m³, taking into account the downward drag force. Hence:

$$E_{k,3} = 1/2\gamma_r H^2 K_{ah} = \\ = 1/2 \cdot 22 \cdot 6.5^2 \cdot 0.198 = \\ = 92.0\,\mathrm{kN/m} \qquad (8)$$

4.3.4. Vertical drainage (case 4)

Also treated in [5] is the case (4) with a vertical drainage adjacent to the retaining wall. Under the assumption that the leachate is freely discharged under the wall bottom or through the wall and the water pressure is thus reduced, the water pressure on the active slip surface can be calculated from the flow net. For an assumed or given slip surface (fig. 14b), the water pressure upon it results from the flow net as: P = 37.1 kN/m, oriented normally to the slip surface. With the weight of the earth wedge (with the saturated unit weight of the soil) of G = 206.9 kN/m, the total load on the barrier resulting from water and earth pressures (fig. 14c) is therefore:

$$E_{k,4} = R = (G - P\cos v) \cdot \tan(90° - v) + P\sin v = 119.3 \text{ kN/m} \qquad (9)$$

4.3.5. Summary of the thrusts acting upon the barrier

Table 1 shows a summary of the resulting horizontal thrusts from E (earth pressure) and W (water pressure) for the considered cases 1 to 4, for the measurements Leonhardsbach L-M and FE calculations Leonhardsbach L-FE. The reduction factors α related to the loads according to ONR 24802 are given in the last column.

5. Measurements at the torrent barriers Leonhardsbach, Schlickerbach and Tödterbach in Tyrol, Austria

For a research project, the instrumentation of several torrent barriers in Tyrol, Austria was carried out to measure the earth pressure and the water pressure over a period of 3 years. The instrumentation included pore water pressure sensors and earth pressure cells at different heights (fig. 15a, 15e and 15g). Figures 15b, 15c, 15d, 15f and 15h show the results of the measurements after completion of the construction work. It can be clearly seen that the pore water pressures are currently of a minor magnitude (fig. 15d, 15f and 15h). Section A-A (fig. 15b) shows a relatively large

Tab. 1 – Comparison of load cases (without model factor).

Case	Conditions	Horizontal load Kn/m	α %
1	backfill moist, no hydrostatic pressure	87.8	34
2	backfill saturated, water pressure according to ONR 24801 and 24802	261.4	100
3	backfill saturated, inclined drainage	92.0	35
4	backfill saturated, vertical drainage	119.3	46
-	Leonhardsbach measurements (see section 5)	78.5-173.9	30-67
2	Leonhardsbach FE (see section 4.2.2)	227.5	87
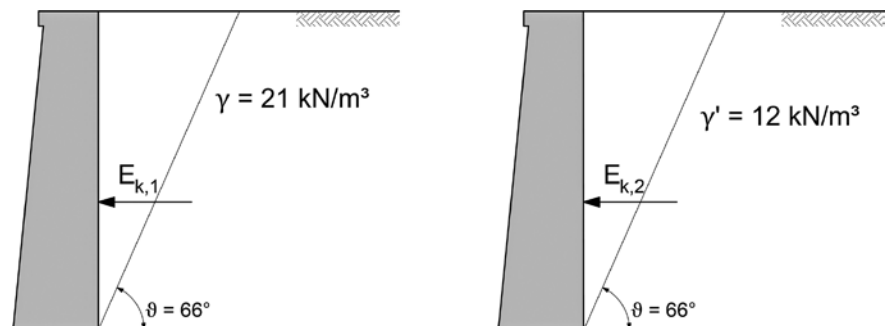
Fig. 13 – (a) Case 1, earth pressure calculated with the moist unit weight. (b) Case 2, without drainage but backfilling water-saturated – full water pressure.
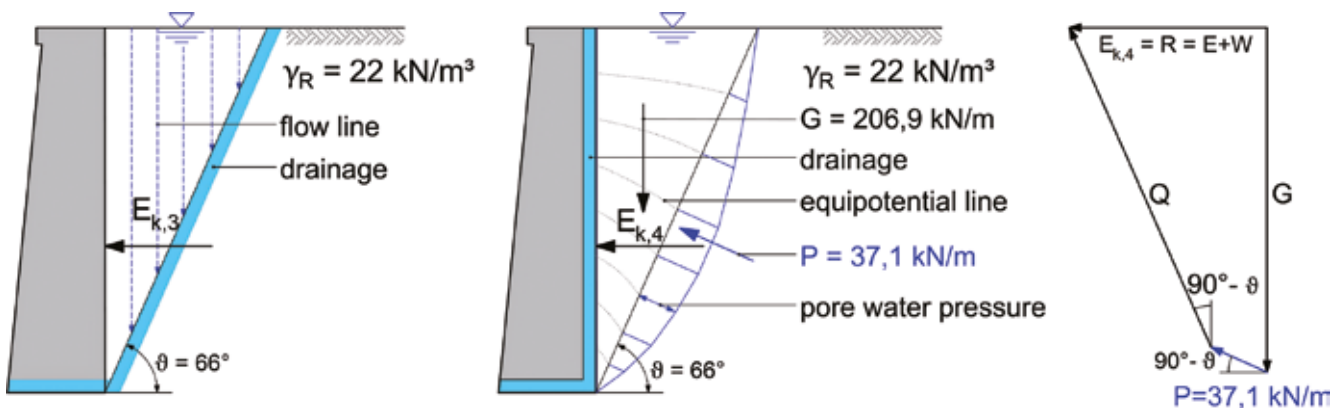
Fig. 14 – (a) Case 3, case of inclined drainage. (b) Case 4, Vertical drainage. (c) Total load on the barrier resulting from water and earth pressures.
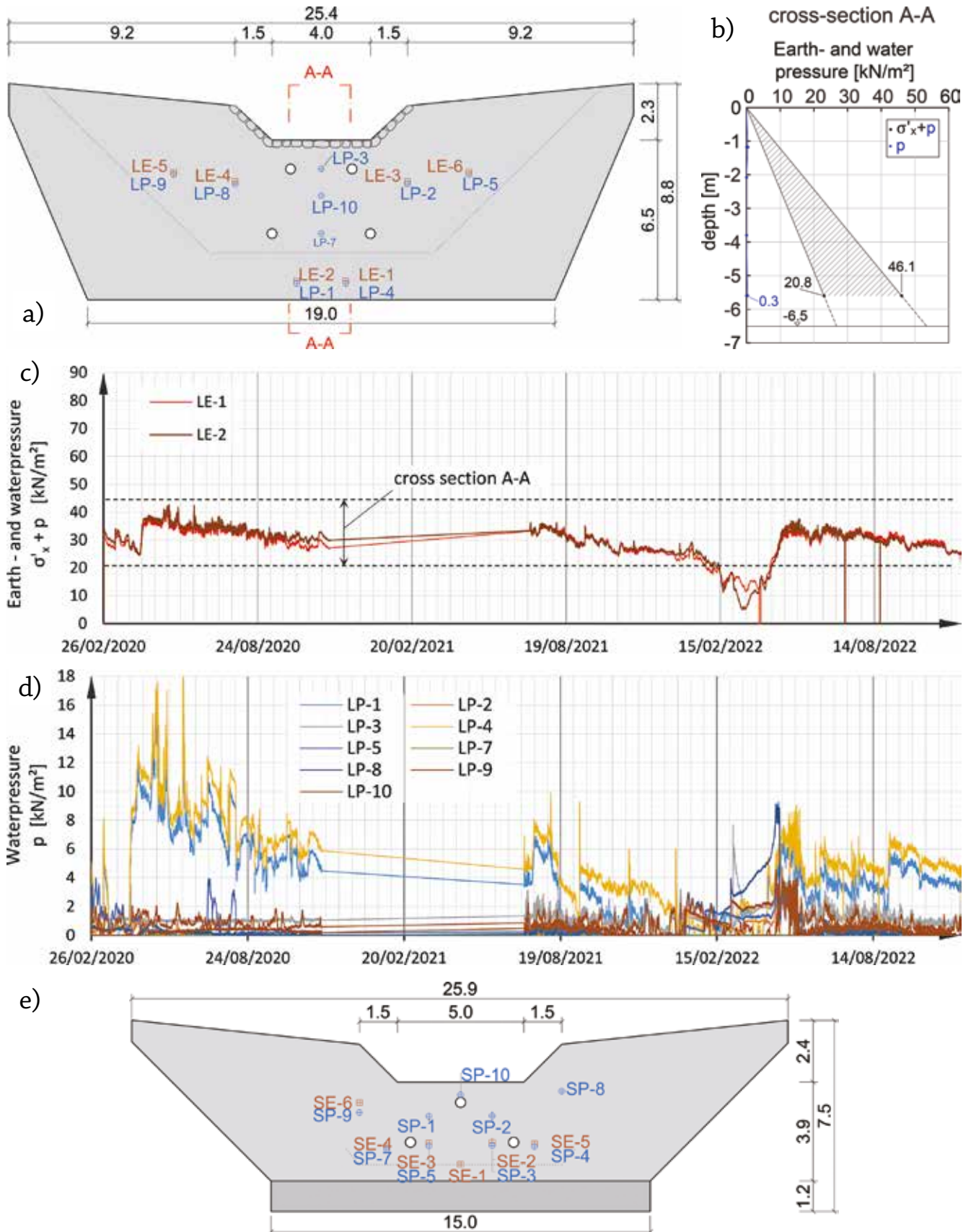
Fig. 15 – (a) Torrenrier Leonhardsbach – Tirol. Water pressure sensors LP1-LP10. Earth pressure cells LE1-LE6. (b) Measured earth pressure ($\sigma'_x + p$) and water pressure (p) in cross-section A-A. (c) Time measurement of the earth- and waterpressure for the torrent barrier Leonhardsbach – Tirol. (d) Time measurement of the waterpressure for the torrent barrier Leonhardsbach – Tirol. (e) Torrent barrier Schlickerbach – Tirol. Water pressure sensors SP1-SP10. Earth pressure cells SE1-SE6.
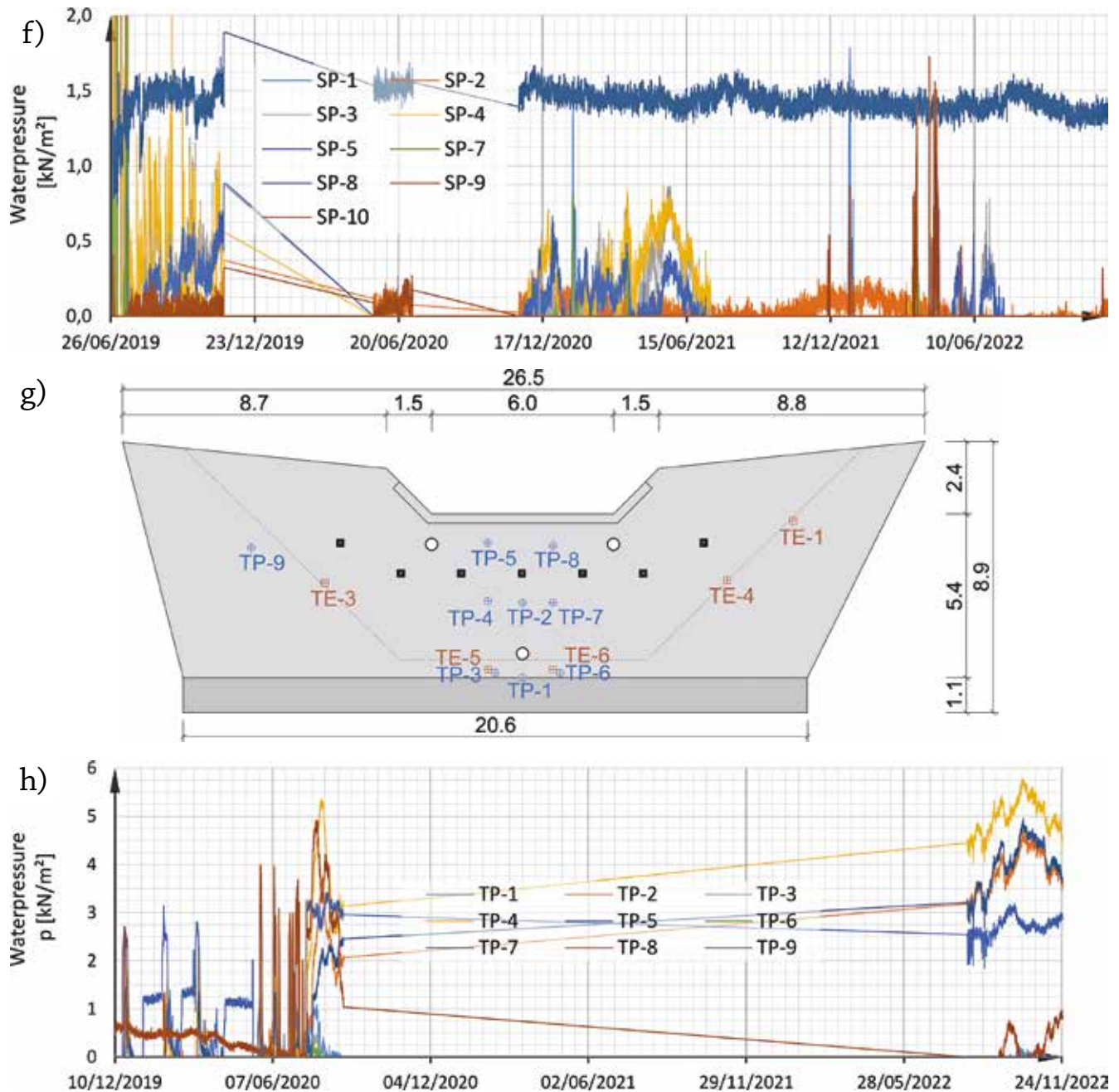
Fig. 15 – (f) Time measurement of the waterpressure for the torrent barrier Schlickerbach – Tirol. (g) Torrent barrier Toedterbach – Tirol. Water pressure sensors TP1-TP10. Earth pressure cells TE1-TE6. (h) Time measurement of the waterpressure for the torrent barrier Toedterbach – Tirol.

fluctuation of the total stresses. The resulting loads on the barriers are determined in formulas 10 and 11.

$$E_{k,A1} = 20.8 \cdot 6.5 \cdot \frac{6.5}{5.6} \cdot \frac{1}{2} = \\ = 78.5 \, \text{kN/m} \qquad (10)$$

$$E_{k,A2} = 46.1 \cdot 6.5 \cdot \frac{6.5}{5.6} \cdot \frac{1}{2} = \\ = 173.9 \, \text{kN/m} \qquad (11)$$

6. Practical implementation and construction recommendations

In the backfill of torrential barriers, a combination of all cases 1 to 4 will occur. The weight of each case and thus the estimation of the load on the structure from water pressure and earth pressure increased by the drag force is difficult because of

the mostly unclear conditions. In sedimentation, less permeable and more permeable layers will alternately be deposited. On the safe side is the approach according to ONR 24801 and ONR 24802, which should be normally used. Only quality-assured construction methods for the cases 1, 3 and 4, shown in Table 1 can reduce the effects. The aim should be to arrange the permeable soils behind the barrier at the
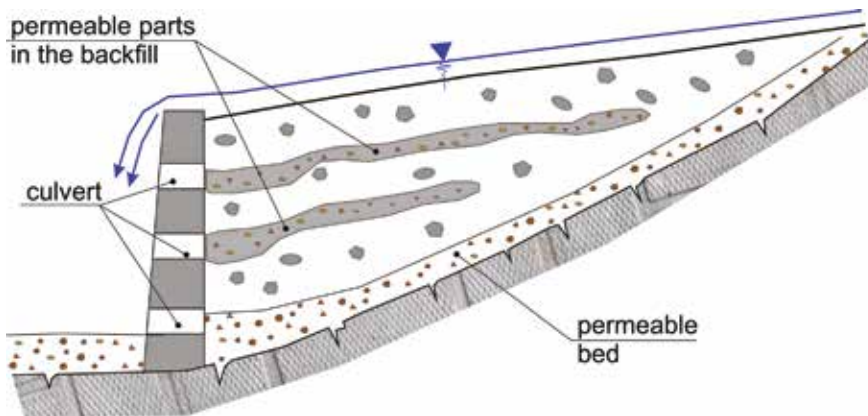
Fig. 16 – Situation in the backfill.

level of the original river bed and to ensure a secure drainage through the culverts. However, the question still remains as to the reliability of these drainage systems with regard to the service life of the barriers.

The combination of cases 1 to 4 (fig. 16) should ultimately be also the reason why, in the case of damage-free torrent barriers, it is not possible to demonstrate the ultimate limit states GEO and STR (Eurocode 7) in accordance with ONR 24801 and ONR 24802, formerly referred to as external GEO and internal stability STR. The calculation results are far beyond the limit state, yet visually no damage is discernible!

7. Proposed procedure for calculating the load

To maintain clarity, we consider all quantities here without safety and mobilization factors. However, to cover the specific uncertainties of the problem under consideration, model factors are introduced which are to be determined at the discretion of the engineers involved. To calculate the loads realistically and to obtain an economic design, it is recommended to select the design case from (case 1 to 4) Table 1 or to determine the loads for the relevant cases and to use a weighted mean value (with the model factors f_i) for the individual loads. Each model factor f_i should

take into account the probability of the respective model. Thus, in cases 3 and 4, the sustainable effectiveness, the quality of execution, the available material and the reliability of the drainage must be taken into account. For case 1, the effectiveness of the sealing of the torrent bottom is of importance. If this is taken into account, the functionality must be guaranteed over the period of use. The model factor f_2 for the most unfavourable load case 2 should be 0.5 from today's point of view. The model factor c (tab. 3) takes into account the risk (via the loss consequence class) of failure of the barrier structure, and the model factor h_m accounts for the height downstram of the structure. The model factors listed reflect the personal assessment of the authors and represent nothing more than a first approximation, which should of course be impro-

Tab. 2 – Model factor h_m for the height H downstram.

Barrier height h	h_m
$H \leq 5\,m$	1.00
$5 < H \leq 10\,m$	1.05
$H > 10\,m$	1.10

Tab. 3 – Model factor c for the failure consequence classes CC (according to EN 1990).

CC	c
CC 1	1.00
CC 2	1.05
CC 3	1.10

ved by subsequent investigations. The characteristic load E_k results as the weighted mean

$$E_k = (E_{k,1} \cdot f_1 + E_{k,2} \cdot f_2 + E_{k,3} \cdot f_3 + \\ + E_{k,4} \cdot f_4 \cdot h_m \cdot c \qquad (12)$$

with
- $f_1 + f_2 + f_3 + f_4 = 1.0$ and
- $E_{k,i}$: characteristic value of earth pressure increased by the drag force and water pressure; calculation for case i
- f_1: 0... 0.2
- f_2: ≥ 0,5
- f_3: 0... 0,2 depending on the drainage effect of the artificial backfill, with independent sedimentation $f_3 = 0$
- f_4: 0... 0.3 depending on the drainage effect of the artificial drainage, with independent sedimentation $f_4 = 0$
- h_m: model factor for the height H, according to Table 2.

With the auxiliary quantity

$$p := (f_1 + f_2 + f_3 + f_4) \cdot h_m \cdot c \qquad (13)$$

equation 12 gives the characteristic thrust as

$$E_k \leq E_{k,2} \qquad (14)$$

The design value of the load is $E_d = E_k \cdot \gamma_E$, where γ_E is the partial safety factor for the load, to be set at 1.0... 1.35 (1.50) depending on the design situation.

With the usual building dimensions and soil parameters, the following load results for the barrier Leonhardsbach for CC1 considered in this article: Without model factors for height and risk, it is obtained:

$$E_k = (87.8 \cdot 0.2 + 261.4 \cdot 0.50 + \\ + 92.0 \cdot 0.2 + 119.3 \cdot 0.05) = \\ = 172.6\ kN/m \qquad (15)$$

8. Conclusions and outlook

In Section 4, four different cases were considered with different ap-

proaches to the effect of water on the earth side of a torrential barrier, in addition to the theoretical analysis of the effect of culverts (Section 4.2). This shows that the provision of culverts (without additional measures) in the barrier can hardly reduce the load and that these structures must therefore be dimensioned in accordance with ONR 24801 and ONR 24802 (Case 2). It is essential to take into account the combination of earth and water pressures, whereby the drag force must also be considered. It goes without saying that the most favourable loads for the barrier result if the torrent water does not percolate. This can be the case due to a lower permeability of the colmated riverbed or by a less permeable backfill (case 1). An inclined or vertical drainage significantly reduces the load from earth and water pressures (cases 3 and 4). In the example of a 6,5 m high barrier discussed in this article, the load reduction is more than 50%.

A reduction of the water pressure on torrential barriers without changing the earth pressure accordingly is not justified. It can be shown that even if the culverts reduce the water pressure, this is accompanied by an increase in the earth pressure as a result of hydrodynamic drag.

References

[1] Böll, A., (1997). Wildbach und Hangverbau, Reports of the Swiss Federal Institute for Forest, Snow and Landscape Research, WSL.

[2] Czerny, F., (1988). Torrent barriers of concrete and reinforced concrete, concrete and cement.

[3] Federal Office for Road and River Engineering, (1973). Dimensioning of torrent barriers, concrete and reinforced concrete, Bern.

[4] Kolymbas, D., (1979). Geotechnics. Soil mechanics, foundation engineering and tunnel construction. 5th edition, Springer Vieweg, 2019.

[5] Lambe, T.W., Whitman, R.V., (1969). Soil Mechanics. SI Version, John Wiley & Sons, New York, Chichester, Brisbane, Toronto, Singapore.

[6] ONR 24802, (2011). Protection structures of torrent control – project planning, dimensioning and structural design. Austrian Standard Institut.

[7] ONR 24800, (2011). Protection structures for torrent control – Terms and their definitions and classification. Austrian Standard Institut.

[8] ONR 24801, (2013). Protection Structures of Torrent Control – Static and Dynamic Effects. Austrian Standard Institut.

Occupational and environmental safety of fluids in chainsaw operations: a review

Marina Clerico*
Nicole Mastromatteo*
Davide Gallione*
Vincenzo Vaccaro*

* Politecnico di Torino

Corresponding author:
nicole.mastromatteo@polito.it

The objective of this review is to analyse the risks associated with the use of fluids in chainsaws operations, comparing traditional and eco-friendly materials.

We chose to investigate operations involving the use of portable equipment, particularly those that still use internal combustion engines. Indeed, they pose a high risk to operators due to their proximity to the machine. The scientific literature concerning fuel mixtures and chain oils was studied.

Correlating the examined activities, equipment and machines and their materials, the risks associated with the use of standard and alkylate fuels and mineral and vegetable chain oils in relation to their use in chainsaw operations were analysed.

The risks depend on the use of the fluids in the different work phases. In the liquid state of the fuel, the absence of benzene in alkylate fuels clearly reduces the carcinogenic risk. In combustion products, the literature review shows that, in the case of 2-stroke engines, the emissions of alkylate fuels are lower than those of conventional fuels for most compounds; on the other hand, the concentrations of PM and formaldehyde do not decrease when alkylate fuels are used.

The literature analysis also shows that the adoption of vegetable chain oils is an improvement.

Keywords: *occupational safety, environmental safety, chainsaw operations, eco-friendly fluids, alkylate gasoline, literature review.*

1. Introduction

As far as the chainsaw operations in forestry are concerned, the "Eco-friendly fluids" definition indicates fuels and oils with low impact on the environment and on the operator's health. These impacts were the topics studied by the "ProBest" operational group, financed through the Regione Piemonte PSR (2014-2020).

This review reports the results of the study conducted by the Department of Environmental, Land and Infrastructure Engineering of the Politecnico di Torino aimed to identify the risks associated with the use of standard fluids and the potential benefits related to more eco-friendly alternative fluids.

The forest area intended for wood production has been relatively stable since 1990. Global wood harvest (from forests, other wooded land and trees outside forests) was estimated to be almost 4.0 billion m^3 in 2018 (considering both industrial roundwood and fuelwood) (FAO,2019). Overall, timber harvesting is globally increasing by 1% per year, both in terms of demand, and consumption of wood products, in line with populations and incomes growth; this trend is expected to continue in coming decades. When done in a sustainable way, woods and forests management stimulates the plants regrowth exceeding the withdrawal balance and resulting in a net CO_2 sink (IPPC, 2022).

Many agricultural, forestry, and other land use (AFOLU) options provide adaptation and mitigation benefits that could be upscaled in the near-term across most regions. Conservation, improved management, and restoration of forests and other ecosystems offer the largest share of economic mitigation potential (IPPC, 2022).

The main fluids involved in forestry work are fuels, additive oils for 2-stroke engines fuel mixtures, hydraulic oils, and lubricating oils, particularly chain oils. Forestry machines using these fluids are distinguished into portable equipment such as chainsaws, brushcutters, mowers, etc. and agricultural machines, such as harvesters, forestry tractors, chippers, etc.

For the occupational issue, operations using hand-held equipment were mainly investigated because of the greater risk to operators, due to the operator-machine proximity.

Despite the growing popularity of electric machines, the most common portable equipment still uses internal combustion engines, particularly 2-stroke engines, so gasoline and additive oils mixtures have been identified as fluids.

In addition, chain oil was also considered in relation to portable tree harvesting and cutting equipment such as chainsaws. It appears to be a fluid that could cause a chemical and/or carcinogenic hazard as a result of its continuous emission (spray) in the chain surrounding environment.

Large machines involved in forestry operations, such as forestry

tractors, excavators and harvesters, require significant amounts of oils for their hydraulic circuits. In case of accidental oil tank/pipes leak, they can induce a significant potential impact on the environment.

These fluids are not the subject of this review because they do not affect the environment under normal operating conditions.

Tab.1 shows the correlation between the examined activities, equipment and machines, and related materials that can generate the previously mentioned risks. Therefore, the review analyzes the risks associated with the use of conventional and alkylated gasolines as well as mineral and vegetable lubricating oils in relation to their use in chainsaw operations. The risks examined include both occupational and environmental aspects.

2. Main reference legislation for the aspects under review

This part of the review identifies the main current regulations in forestry and chainsaw operations. The product regulations governing the fluids under analysis are recalled from time to time in the following paragraphs related to the different risks identified.

Regarding occupational safety, reference is made to Title IX of Legislative Decree 81/08: for chemical risk from exposure to hazardous substances present in mixtures and chain oils, the current reference is Article 223; while for carcinogenic risk, due to exposure to hazardous substances possibly present in mixtures and combustion products, Article 235 is the applicable reference.

Concerning the fuel used for machinery and equipment, there

Tab. 1 – Machines and activities involving contact with and/or use of the fluids analyzed.

		Manual felling
Mixture for two-stroke engine (gasoline and additive oil)	Chainsaw	Manual sectioning
		Manual limbing
		Pruning
		Supply
	Brushcutter	Supply
		Forest clearance cut
Chain oils	Chainsaw	Manual felling
		Manual sectioning
		Manual limbing
		Pruning
	Harvester	Mechanized felling
		Mechanized sectioning
		Mechanized limbing

are many regulatory references dealing with environmental safety, sustainability, containment of climate change and greenhouse effect. In addition to the Directives related to occupational safety, these include Directive 2002/3/EC on ozone in the air, Directive 2008/50/EC on ambient air quality and its Italian transposition with Legislative Decree 155/2010. Regarding environmental aspects, reference is made to Directive 2009/30/EC. It, while regulating minimum specifications for fuels for road and non-road transport, introduces, by amending Directive 98/70/EC, important requirements for environmental impact assessment of fuels and biofuels, reiterating general shared aspects also valid for the present study and adoptable by analogy both for the identification of minimum quality (emissions) targets for gasoline/blends (alkylate gasoline) and for the assessment of the overall impact and greenhouse effect of bio-oils (chain oil and hydraulic oil).

Another regulatory reference is Directive 2009/28/EC on the promotion of the use of energy from renewable sources, which, although not relevant to the pre-

sent study, is important for general criteria and target reference values. Important to mention is Regulation 2016/1628, in which new emission limits for gaseous and particulate pollutants and type-approval for internal combustion engines for non-road mobile machinery are set to achieve the Union's air quality objectives and to reduce emissions from non-road mobile machinery and agricultural and forestry vehicles.

Other regulations related to the type-approval of agricultural and forestry machinery are Directive 2003/37/EC (Agricultural and forestry machinery); Regulation (parent standard) EU 167/2013/EC (Non-road machinery engines); and EU Delegated Regulation 2018/985/EC (Forestry machinery environmental performance). The latter, in Article 3, indicates the adoption of environmental performance as per Regulation 2016/1628/EC also for forestry machinery engines; Article 5, on the other hand, similarly indicates the performance of engines with regard to fuel consumption as per UNECE Regulation No. 120.

Not secondary are the regulatory constraints related to the storage phase of the product, as

well as the transport phase in tanks outside those installed on the equipment. The regulations do not change in the case of conventional or alkylated gasoline and their respective blends; in all cases, the legal limits expressed for maximum quantities that can be stored, the types of storage, the characteristics of suitable containers certified for transport, and the maximum quantity that can be transported must be respected, also depending on the distances to be covered.

The facility of finding gasoline with which to produce the blend locally, close to the operating sites, may mitigate storage and transportation problems. This could disadvantage an increase in products, such as alkylate gasoline blends, that need to be purchased in advance, temporarily stored, and then transported from the company location to the operating site. However, since the difficulty of storing and transporting combustible products (gasoline, blending oils, lubrication oils and hydraulic oils) is a generalized problem, it is hoped that centralized institutional intervention action will be issued, thus encouraging in parallel the use of innovative products, the development of storage areas and transport containers and a greater territorial spread of product distribution points.

3. Methodology

The objective of this review is to assess the benefits of alternative fluids and, in case of multiple options, to focus on those with the best environmental performance, at the same level of human health protection.

The environmental analysis of an action such as the substitution of a material within a production cycle must extend to the entire life cycle of the new product to be adopted, examining local and global impacts, short and long-term effects, and considering both pollutant emissions and resource use. It is also important to check the specific consumption of the products involved. At a reduction in environmental impact due to the change of substance, the increased consumption of resources, or the increase in emissions elsewhere in the system, should not lead to a negative overall environmental balance.

The analysis method adopted can be summarized as follows:
– description of the reason why the material change is desired;
– estimation of the positive employment and environmental impacts of the action on local and global scale;
– identification of any negative spillovers (e.g., packaging, storage, transportation, disposal, etc.) on local and global scale, also considering the product supply chain.

4. Materials involved

The 2-stroke engine is fueled by a gasoline-oil mixture with varying composition depending on the machine (usually the concentration of the oil/fuel mixture is 2%). It is therefore important to keep in mind, as already shown in Table 1, that contact with hazardous substances may occur not only during refueling through the possible inhalation of fuel vapors, but also during operation through the inhalation of exhaust gases.

The main categories of compounds present in exhaust gases generated during the operation of portable equipment potentially dangerous for the operator health are volatile organic compounds (VOCs) identified as aromatic (e.g., benzene) and alipha-tic (e.g., methane) hydrocarbons, polycyclic aromatic hydrocarbons, carbon monoxide (CO), nitrogen oxides (NOx) and other oxides and aldehydes.

Assuming personnel exposure to various hazardous chemicals in the exhaust gases of the equipment used (All. V Legislative Decree 81/08), the presence of carcinogens such as benzene should be highlighted, being such chemical compound classified as carcinogenic to humans, belonging to Group 1 according to the IARC (International Agency for Research on Cancer) classification. Alternative fuels to conventional gasoline, called alkylate gasoline, are available on the market: they propose a potential improvement because they do not contain benzene. This review analyzes the validity of this alternative as an occupational environmental safety improvement.

4.1. Alkylated gasolines

For fuel used for manual forestry equipment such as chainsaws and brushcutters, the risk of emission of toxic products can be represented as high probability, medium magnitude, and correlated with some weighting factors ki such as: k1 (type of fuel used), k2 (type of blend oil used), k3 (2 or 4-stroke engine type), k4 (engine seniority), k5 (combustion quality), k6 (type of activity), k7 (hourly consumption), k8 (packaging mode), k9 (storage/availability mode), k10 (need for decanting), k11 (transportation mode).

Alkylate fuel, commonly used in hand machinery, is rich in short-chain, single-bond hydrocarbons and has a low content of alkenes, oxygenates and aromatic compounds. A.A. Zardini, in research conducted in 2019, certifies not only the components of fuels, but also

those of additive oils in the two-stroke mixture (A.A. Zardini, 2019). He evinces how alkylated gasolines (fuel and/or blend) resulted non-carcinogenic material/input to the production cycle, unlike conventional gasolines.

Concerning the environment, alkylate gasolines are nonrenewable since they are of mineral origin, and therefore derived from petroleum, even if produced from the last stages of distillation. The full safety data sheets show the hazard pictogram for the aquatic environment: H411 and H413 environmental potential classification apply, indicating long-lasting harmfulness and potential toxicity to aquatic life, as well as for conventional gasolines.

Regarding combustion products, emissions are regulated as follows: some emissions (such as CO, THC, PM, PN or PAHs, SOx, FAME) are regulated directly by the type-approval laws of the adopted powertrain and/or fuels of forestry machinery; other substances, which do not have specific limits for emissions in forestry, are controlled in the context of adopted fluid quality and/or air quality (such as benzene, SOx, CO_2, O_3); other constituents, while coded as harmful to humans and/or to the environment, are not explicitly regulated and their presence is controlled within the broader scope of quality and health objectives (such as aldehydes, VOCs, the precursors of O_3), as well as sustainability and containment of climate-altering gases (especially CO_2, N_2O, CH_4).

In (A.A. Zardini, 2014) the regulated and unregulated emissions of a 2-stroke and a 4-stroke engines were characterized for both conventional and alkylated gasoline. Standard gasoline and synthetic lubricating oil were replaced with an alkylate fuel with low aromatic compound content and an ultra-clean lubricating oil with low ash-forming potential. A

reduction in emissions was observed for several gaseous and particulate species, particularly carbon monoxide, particulate mass, aromatic compounds, and secondary organic aerosol (A.A. Zardini, 2014).

The alkylate fuel and ultra-clean oil combination causes a large emission reduction for regulated and unregulated compounds, SOA included, with some exceptions, formaldehyde, for instance (A.A. Zardini, 2014).

In the previously mentioned study by Zardini, from which Figure 1 was extrapolated, lower emissions of alkylate gasoline compared to conventional gasoline are confirmed for regulated compounds, and for PM (A.A. Zardini, 2014).

From an occupational safety perspective, F. Neri's study (F. Neri, 2016) investigates the inhalation exposure of forestry workers to polycyclic aromatic hydrocarbons (PAHs) and BTEX (benzene, toluene, ethylbenzene, and total xylenes) contained in the exhaust

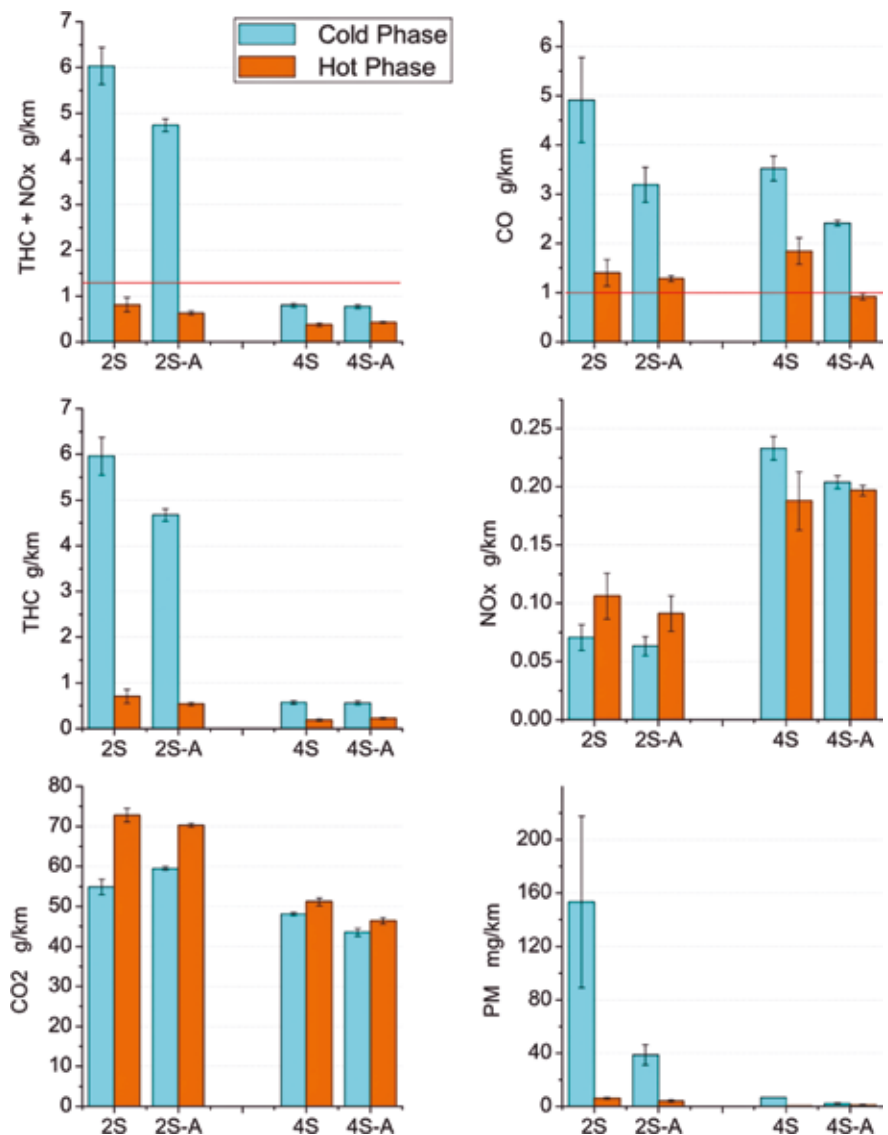Fig. 1 – Average emission factors (mass/distance) of regulated compounds grouped by scooter and fuel types, and split into cycle phases. The 2-stroker (2S) emits more THC, CO, and PM (dominated by cold phase emissions) than the 4-stroker (4S). The use of the alkylate fuel reduces THC, CO, PM and NOx of the 2S (2S-A, where A stands for alkylate) and CO, PM, NOx of the 4S. From: (A.A. Zardini, 2014).

gases released by chainsaws in order to suggest possible safeguards. It compares, over four different silvicultural treatments (clear cutting, conifer thinning, conifer pruning, and sanitary cutting), three different types of chainsaw fuel, specifically a normal two-stroke gasoline blend and two alkylate fuels. Statistically significant differences in inhalation exposure to PAHs and BTEX were recorded when using different types of fuel. In particular, inhalation exposure to PAHs and BTEXs was generally an order of magnitude lower when using modern alkylate fuels than when using the traditional blend of 2-stroke oil and unleaded gasoline. The study indicates that while forestry workers are exposed to PAHs and BTEX, the maximum va-

lues found are generally well below the limits indicated for occupational exposure.

Dimitrakopoulos's study (N. Dimitrakopoulos, 2020) plots emissions of HC, CO, NOx, and SOOT, as a function of engine load, comparing conventional with alkylated gasolines. As shown in Figure 2, the results for alkylate gasolines compared to conventional gasolines indicate similar emission values for HC, lower CO and NOx figures, but higher SOOT amount (in fact, exhaust soot in the case of alkylates is almost double, especially as engine load increases). More complex is the interpretation of data for PM dust and SOOT ash: the improvement introduced by alkylate gasoline is not so clear.

Therefore, the literature analysis shows that for most of the regulated combustion product compounds of two-stroke engines, the emission factors of alkylate gasolines are lower than those of conventional gasolines, although a significant spread in emissions reduction can be noticed across the different tests.

Also, for most of the non-regulated compounds several studies indicate that, the emission factors of 2-stroke engines powered by alkylate gasolines are lower than those of conventional gasolines. On the other hand, the emission factors of CH_4 (and CH_4 CO_2(eq)) and aldehydes (acetaldehyde and formaldehyde) remain more critical, with higher combustion products for alkylate gasolines com-
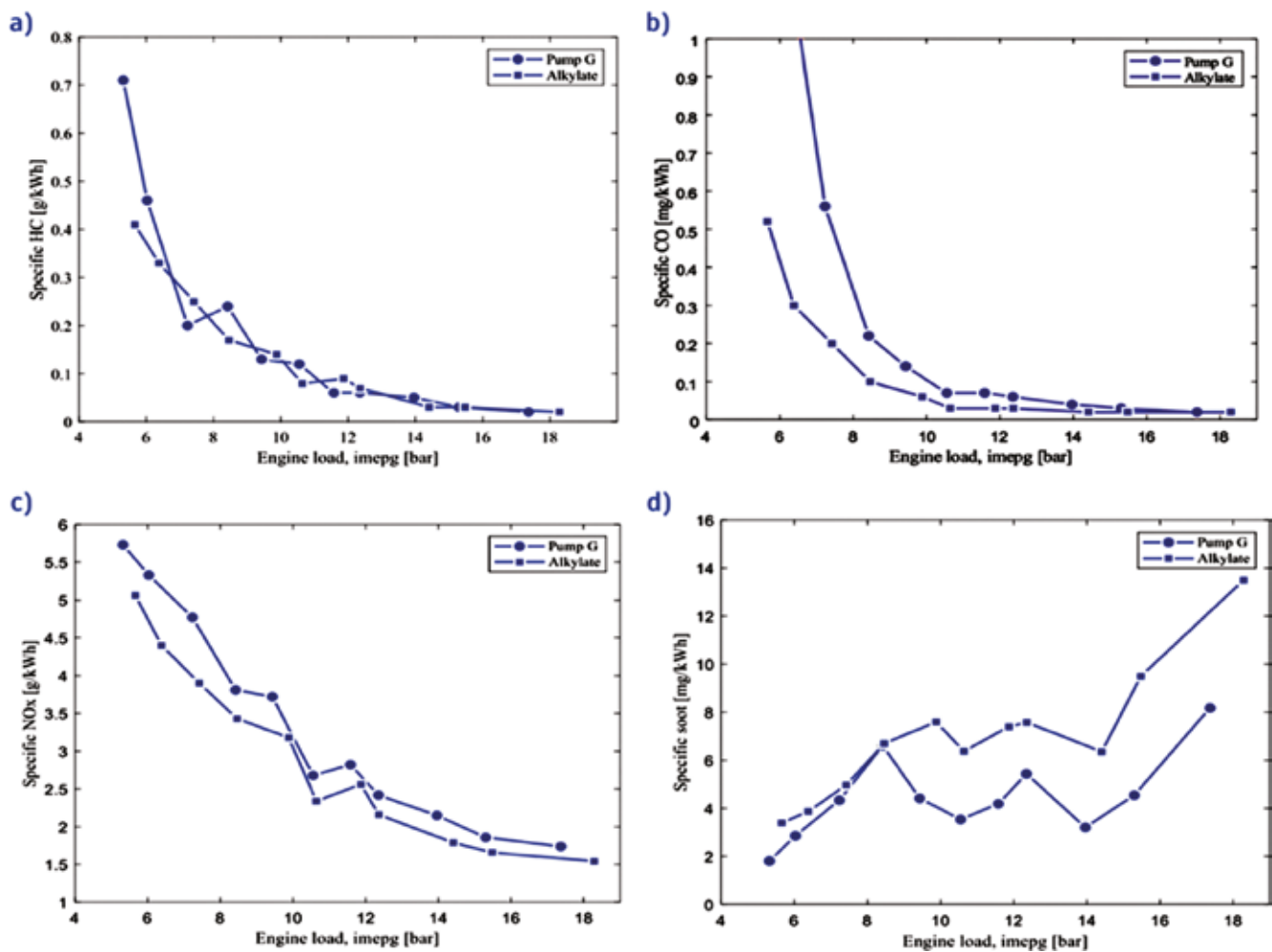

Fig. 2 – Emissions of the different compounds for the two types of gasoline. a) HC, b) CO, c) NOx, d) SOOT. From: (N. Dimitrakopoulos, 2020).

pared with conventional gasolines. In particular, the presence of formaldehyde, which is more critical to worker health, requires further investigation and future monitoring. Another important element to observe is the presence of ozone precursor compounds, the measurement of which is explicitly required in Annex VI of Directive 2002/3/EC.

4.2. Chain oils

The use of oils of vegetable origin is aimed to reduce the toxic substances release into the environment around the processing site, both for the environment and the operators protection.

In the presence of materials with environmentally toxic characteristics, the scenarios describing the emissive dynamics are different whether we are talking about chainsaws rather than harvesters or other agricultural machinery. In the case of chainsaws, chain oil dispersion occurs when the machine is used: the lubricant is supplied to the saw-chain causing the projection of a suspension consisting of droplets and volatile part of fluid into the blade surrounding environment, with the associated generation of continuous environmental pollution which also involves the operator.

So for the dynamics of environmental (as well as occupational) risk, which may account for the emissive condition of the chainsaws lubricating oil, the risk function can be explicated as a relationship between high probability, low magnitude, and ki weighting factors such as: k1 (type of oil used), k2 (flux density g/m^2), k3 (amount of wood cut/h), k4 (sensitive forest environment), k5 (critical biodiversity), and k6 (type of environment in which it operates).

5. Conclusions

Having identified from the local-scale study for portable forestry equipment an improvement for both the human health and the environment associated with the use of alkylate gasoline in place of conventional gasoline, a global scale impact estimation of this substitution is definitely needed to close the environmental balance sheet. In order to support the adoption of alkylate gasolines, management actions for the critical points that could result from their widespread use should be planned.

In particular, improvement actions are to be developed to address:

– the environmental issue induced by the presence of the blend packaging containers (additional use of resources and disposal of plastic materials), imposed at this time due to the absence of "bulk" sales outlets for gasoline, which is the standard situation for conventional gasoline;

– the greater storage problems compared with traditional fluids caused by large quantity/cost effective purchasing and stock issues whose management require upgrades in companies organization and processes; fire and explosion safety problems to third parties are also to be addressed;

– the transportation problems, especially when forestry sites are located far away from populated areas;

– the fossil origin of alkylate gasolines include these fuels in the nonrenewable resources category, and their environmental impact remains that of fossil fuels, with a particularly high energy rating for their derivation from pushed degrees of distillation.

In general, the environmental balance improves by decreasing the products consumption and waste; alkylate gasolines guarantee this with consumption comparable to that of conventional gasolines while granting longer shelf life in storage (even in the machine fuel tank). Referring to chain oils, vegetable origin oils have much lower direct environmental toxicity characteristics than classical mineral or synthetic oils.

As can be observed from the safety data sheets of the substances, many environmental hazards and/or risk statements present in classic oils documentation no longer appear for the proposed alternative vegetable oils. In terms of balance, all aspects that may be involved in the replacement of classic oils with vegetable oils are to be carefully evaluated.

On a local scale, the replacement of synthetic oils with vegetable oils (unlike the alkylate fuels) brings positive spin-offs from both the employment and the environmental point of view (without any impact on packaging, storage and transportation issues). However, socio-economic aspects related to the higher cost of plant products remain open, which requires supporting actions to improve and ensure socio-economic sustainability over time as well. On a global scale, it is necessary to initiate major actions to improve the bio-fluid production sustainability, identifying the impacts of the entire product chain. The reference points for the analysis of the impacts on the global environmental system are already present in the comments of international recommendations, particularly in the EU recommendation sentences of the Biofuels Directive.

For the verification of the environmental balance, bio-fluids must meet the sustainability criteria already referred to for lubricating vegetable oils, as well as set out in Directive 2009/30/EC, namely on sustainability and limitation of the greenhouse effect of bio-fuels (including oils).

References

- D.lgs. 9 aprile 2008, n. 81 Testo coordinato con il D.lgs. 3 agosto 2009, n. 106 testo unico sulla salute e sicurezza sul lavoro.
- Direttiva 2002/3/CE del Parlamento europeo e del Consiglio, del 12 febbraio 2002, relativa all'ozono nell'aria.
- Direttiva 2008/50/CE del Parlamento europeo e del Consiglio, del 21 maggio 2008, relativa alla qualità dell'aria ambiente e per un'aria più pulita in Europa.
- D.lgs. 13 agosto 2010, n. 155 Attuazione della direttiva 2008/50/CE relativa alla qualità dell'aria ambiente e per un'aria più pulita in Europa.
- Direttiva 2009/30/CE del Parlamento europeo e del Consiglio del 23 aprile 2009 "che modifica la direttiva 98/70/CE per quanto riguarda le specifiche relative a benzina, combustibile diesel e gasolio nonché l'introduzione di un meccanismo inteso a controllare e ridurre le emissioni di gas a effetto serra, modifica la direttiva 1999/32/CE del Consiglio per quanto concerne le specifiche relative al combustibile utilizzato dalle navi adibite alla navigazione interna e abroga la direttiva 93/12/CEE".
- Direttiva 98/70/CE del Parlamento europeo e del Consiglio del 13 ottobre 1998 relativa alla qualità della benzina e del combustibile diesel e recante modificazione della direttiva 93/12/CEE del Consiglio.
- Direttiva 1999/32/CE del Consiglio, del 26 aprile 1999, relativa alla riduzione del tenore di zolfo di alcuni combustibili liquidi e che modifica la direttiva 93/12/CEE.
- Direttiva 2009/28/CE del Parlamento europeo e del Consiglio del 23 aprile 2009 sulla promozione dell'uso dell'energia da fonti rinnovabili, recante modifica e successiva abrogazione delle direttive 2001/77/CE e 2003/30/CE.
- Regolamento (UE) 2016/1628 del Parlamento europeo e del Consiglio del 14 settembre 2016 relativo alle prescrizioni in materia di limiti di emissione di inquinanti gassosi e particolato inquinante e di omologazione per i motori a combustione interna destinati alle macchine mobili non stradali, e che modifica i regolamenti (UE) n. 1024/2012 e (UE) n. 167/2013 e modifica e abroga la direttiva 97/68/CE.
- Direttiva 2003/37/CE del Parlamento europeo e del Consiglio del 26 maggio 2003 relativa all'omologazione dei trattori agricoli o forestali, dei loro rimorchi e delle loro macchine intercambiabili trainate, nonché dei sistemi, componenti ed entità tecniche di tali veicoli e abroga la direttiva 74/150/CEE.
- Regolamento (UE) N. 167/2013 del Parlamento europeo e del Consiglio del 5 febbraio 2013 relativo all'omologazione e alla vigilanza del mercato dei veicoli agricoli e forestali.
- Regolamento delegato (UE) 2018/985 della Commissione del 12 febbraio 2018 che integra il regolamento (UE) n. 167/2013 del Parlamento europeo e del Consiglio per quanto riguarda le prescrizioni relative alle prestazioni ambientali e delle unità di propulsione dei veicoli agricoli e forestali e dei loro motori e che abroga il regolamento delegato (UE) 2015/96 della Commissione.
- Regolamento n. 120 della Commissione economica per l'Europa delle Nazioni Unite (UN/ECE) — Disposizioni uniformi relative all'omologazione dei motori a combustione interna destinati a essere montati sui trattori agricoli e forestali e sulle macchine mobili non stradali per quanto riguarda la misurazione della potenza netta, della coppia netta e del consumo specifico di carburante [2019/405].
- D.lgs. 3 aprile 2006, n.152 — Testo unico ambientale.
- D.lgs. 26 giugno 2015, n.105 — Direttiva Seveso III.
- IPPC Intergovernmental panel on climate change, Sixth Assessment Report (AR6), Synthesis Report (2023).
- IPPC Intergovernmental panel on climate change, Sixth Assessment Report (AR6), Climate Change 2022: Mitigation of Climate Change, Cap. 7.
- Comunicazione della Commissione al Parlamento Europeo, al Consiglio, al Comitato Economico e Sociale Europeo e al Comitato delle Regioni – Nuova strategia dell'UE per le foreste per il 2030 (2021)
- D.lgs. 3 aprile 2018, n. 34 – Testo unico in materia di foreste e filiere forestali.
- Direttiva (UE) 2019/130 del Parlamento europeo e del Consiglio del 16 gennaio 2019 che modifica la direttiva 2004/37/CE sulla protezione dei lavoratori contro i rischi derivanti da un'esposizione ad agenti cancerogeni o mutageni durante il lavoro.
- D.lgs. 1 giugno 2020, n. 44 – Attuazione della direttiva (UE) 2017/2398 del Parlamento europeo e del Consiglio, del 12 dicembre 2017, che modifica la direttiva 2004/37/CE del Consiglio, relativa alla protezione dei lavoratori contro i rischi derivanti da un'esposizione ad agenti cancerogeni o mutageni durante il lavoro.
- Decreto 11 Febbraio 2021 – Nuovi processi e sostanze cancerogene e mutagene nel TUS – Recepimento della direttiva (UE) 2019/130 del Parlamento europeo e del Consiglio del 16 gennaio 2019, nonché della direttiva (UE) 2019/983 del Parlamento europeo e del Consiglio del 5 giugno 2019 che modificano la direttiva (CE) 2004/37 del Parlamento europeo e del Consiglio del 29 aprile 2004 sulla protezione dei lavoratori contro i rischi derivanti da un'esposizione ad agenti cancerogeni o mutageni durante il lavoro (in vigore dal 15.02.2021 dalla pubblicazione sul sito MLPS).
- Osservatorio Foreste INEA, MIPAAF, MATTM, CFS, Regione Veneto, Regione Toscana, Regione Basilicata, Regione Puglia, Regione Molise, INEA; CRA e ISMEA. Criteri e buone pratiche di gestione forestale Baseline per l'attuazione della misura silvo-ambientale. Rete Rurale Nazionale, MIPAAF, 2009.
- ILCD Handbook: Framework and requirements for LCIA models and

indicators, JRC European Commission, 2010.

- D.lgs. 18 maggio 2001, n. 227 Orientamento e modernizzazione del settore forestale, a norma dell'articolo 7 della legge 5 marzo 2001, n. 57.

- Decreto 03/09/2002 – Ministero dell'ambiente e della tutela del territorio («Linee guida per la gestione dei siti Natura 2000» ai sensi della L 357/97) e smi.

- Direttiva 2004/37/CE del Parlamento europeo e del Consiglio del 29 aprile 2004 sulla protezione dei lavoratori contro i rischi derivanti da un'esposizione ad agenti cancerogeni o mutageni durante il lavoro (sesta direttiva particolare ai sensi dell'articolo 16, paragrafo 1, della direttiva 89/391/CEE del Consiglio).

- Regolamento (CE) N. 1272/2008 del Parlamento europeo e del Consiglio del 16 dicembre 2008 relativo alla classificazione, all'etichettatura e all'imballaggio delle sostanze e delle miscele che modifica e abroga le direttive 67/548/CEE e 1999/45/CE e che reca modifica al regolamento (CE) n. 1907/2006.

- Decreto 21/01/10 – Ministero delle politiche agricole alimentari e forestali (Buone pratiche forestali ai fini dell'applicazione della misura «pagamenti silvo-ambientali).

- Decisione (UE) 2018/1702 della Commissione dell'8 novembre 2018 che stabilisce i criteri per l'assegnazione del marchio di qualità ecologica dell'Unione (Ecolabel UE) ai lubrificanti.

- Regolamento (UE) N. 167/2013 del Parlamento europeo e del Consiglio del 5 febbraio 2013 relativo all'omologazione e alla vigilanza del mercato dei veicoli agricoli e forestali.

- Regolamento (UE) N. 168/2013 del Parlamento europeo e del Consiglio del 15 gennaio 2013 relativo all'omologazione e alla vigilanza del mercato dei veicoli a motore a due o tre ruote e dei quadricicli.

Dimitrakopoulos, N., Tuné, M., (2020). Evaluation of engine efficiency, emissions and load range of a PPC concept engine, with higher octane and alkylate gasoline [Journal]. – [s.l.]: Fuel, pp. 0016-2361: Vol. 275.

Neri, F., Foderi F.C., Laschi, A., Fabiano, F., Cambi, M., Sciarra, G. Aprea, M.C., Cenni, A., Marchi, E., (2016). Determining exhaust fumes exposure in chainsaw operations [Journal]. – [s.l.]: Environmental Pollution, pp. 1162-1169: Vol. 218.

Ostennark, U. (1996). Alkylate petrol: Environmental Aspects of Volatile Hydrocarbon Emissions // Doctoral Thesis. – Sweden: [s.n.].

Zardini, A.A., Platt, S.M., Clairottem, M., El Haddad I., Temime-Roussel, B., Marchand N., Jezek, I., Luka, L., Mocnik, Slowik, J.G., Manfredi, U, Prévôt, A.S.H., Baltensperger, U., Astorga, C., (2014). Effects of alkylate fuel on exhaust emissions and secondary aerosol formation of a 2-stroke and a 4-stroke scooter [Journal]. – [s.l.]: Atmospheric Environment, pp. 307-315: Vol. 94.

Zardini, A.A, Suarez-Bertoa, R., Forni, F., Montigny, F., Otura-Garcia, M., Carriero M., Astorga, C., (2019). Reducing the exhaust emissions of unregulated pollutants from small gasoline engines with alkylate fuel and low-ash lube oil [Journal]. – [s.l.]: Environmental Research, p. 203, 2014: Vol. 170.

Study on fine soil behaviour in function of temperature in the context of climate change

Jérémy Jean Daniel Torche*
Erika Prina Howald*

* School of Engineering and Management Vaud (HEIG-VD), Institute Insit, Yverdon-les-Bains, Switzerland

Corresponding author:
erika.prinahowald@heig-vd.ch

One of the expected effects of global warming is the gradual melting of permafrost. Its melting will significantly impact soil material properties, potentially causing instability of infrastructures and triggering natural hazards.
The objective of this experimentation is to quantify the effect of thawing on the geomechanical strength of a reconstituted fine soil. More specifically, it is intended to qualify the initial frozen state and compare it to the state after thawing. This study was carried out in three steps. To begin, soil samples were identified by the usual parameters. Then, artificial samples were sheared at a temperature of –5°C in our temperature controlled triaxial press in order to determine the soil's parameters. Finally, identical tests were carried out at a temperature of +5°C in order to thaw the soil completely before the shearing. In total, three tests for each temperature were compared and discussed. The expected results aim at a better understanding and quantification of soil strength reduction after the thawing phase. As many infrastructures are now built on permafrost, such as infrastructures, or alpine chalets, they will be affected by this phenomenon in the near future. A better understanding of (geo)mechanical consequences might facilitate risk analysis, evaluation and mitigation.
***Keywords**: climate change, temperature controlled triaxial test, permafrost.*

1. Introduction

The thawing of permafrost has a lot of consequences, not just for the strength of the ground, but also for the structures and infrastructures built on it. Indeed, the variation in ground resistance during the thawing process can lead to a loss of bearing capacity, causing failure of man-made installations and an increase in the frequency of natural hazards. Therefore, this can have an impact on the life of the community.

Permafrost refers to land where the temperature does not exceed 0 °C for at least one year. There are several categories of permafrost:
- Continuous permafrost (more than 80% of the surface area)
- Discontinuous permafrost (between 30% to 80% of the surface area)
- Sporadic permafrost (less than 30% of the surface area)

Permafrost covers around 20% of continental surfaces, mainly at high latitudes (Arctic polar zone, including Greenland, Arctic Siberia, Alaska and northern Canada). Discontinuous permafrost can also be found in the Alps above 2,500 meters and continuous permafrost above 3,500-4,000 meters.

As the impacts of climate change have become increasingly visible over the last few decades, research has been stepped up around the world. Zhang & al. conducted studies on the response of Canadian permafrost after a rise of aerial temperature. The simulation results showed that, at a depth of 0.2 m, a permafrost temperature increase of 2.1 °C, respectively 5.1 °C was expected, for and aerial temperature increase of 2.8 °C, respectively 7 °C (Zhang, *et al.*, 2008). Several predictions of global warming tend to an increase of air temperature to 2 °C to 4 °C in 2100 (Hipp, *et al.*, 2011; Guo, *et al.*, 2012; Lyon, *et al.*, 2022). The temperature of the permafrost will follow the increase of the air temperature. This rise in the soil's temperature progressively shrinks the extent of permafrost and increases the danger areas.

The permafrost degradation due to the global warming effect has a large incidence on natural hazards incurring in mountains such as debris flows, landslides, rock falls, etc. (Haeberli, 1992; Isaksen, *et al.*, 2001; Isaksen, *et al.*, 2002; Etzelmüller, *et al.*, 2003; Isaksen, *et al.*, 2011; Farbrot, *et al.*, 2013; Blikra & Christiansen, 2014; Myhra, *et al.*, 2017; Frauenfelder, *et al.*, 2018; Matthews, *et al.*, 2018) (Prina Howald, *et al.*, 2016). Risk maps have been drawn up in Russia, based on the effects of global warming on permafrost (Perov, *et al.*, 2017). Other studies (Saemundsson, *et al.*, 2018; Sattler, *et al.*, 2011; Stoffel, *et al.*, 2011; Damm & Felderer, 2013; Bardou, *et al.*, 2011) pointed out the impact of degrading permafrost on the triggering of debris flows. The evolution of the rocky glacier dynamics due to the rise of the temperature (Arenson, *et al.*,

2002) can explain the frequency and amplitude increase of the debris flows. Similar studies have been conducted in China (Ding, *et al.*, 2019) and in the Norwegian sub-arctic permafrost (Hilger, *et al.*, 2021). This degradation is clearly discernible in mountainous countries. For example, in Switzerland we observe the gradual permafrost thawing, thus increasing its instability. This instability can manifest itself by very impressive phenomena such as the collapse of Piz Cengalo in 2017 causing the death of eight people. Another less dramatic issue is the melting of the Theodule glacier. This has caused diplomatic problems between Switzerland and Italy. In fact, the Italian-Swiss border follows the water divide, with the north flowing into Switzerland and the south flowing into Italy. Between 1973 and 2010, the Theodule glacier lost almost a quarter of its mass. This has altered the watershed, forcing the two governments to redraw a few dozen meters of border. Moreover, this border shift has had the effect of "moving" an Italian refuge to Switzerland. The case of the Matterhorn Guides refuge was the subject of intense diplomatic negotiations for over three years in order to reach an agreement between Italy and Switzerland. On top of that, as the risk of falling rocks increases with the thawing of permafrost, many hiking trails close for the safety of people. This closure impacts the local economy.

The consequences of the thaw can have several direct or indirect repercussions for society, which is why it is important to study and understand this phenomenon.

The study of permafrost in Switzerland is an active field of research, mainly since the '70s. A triggering fact was the instability of the ice-saturated scree slopes of the Grande Dixence hydroelectric plant. The study of the phenomenon is very complex and covers many aspects. Chamberlain & Gow have studied in 1979 the evolution of the permeability of four fine-grained soils after a cycle of freeze / thaw. The results are surprising as it was found that the void ratio decreases and the vertical permeability increases. The process depends on the type of soil and no definite relationships have been established (Chamberlain & Gow, 1979). Scientists have also conducted studies on the formation of ice lenses during freezing (Dysli, 1993) and on the evolution of isotherms during freezing, the heat transfers, the water flow during the formation of the ice lenses, the evolution pressures / capillary suctions or the swelling of the ground.

Arenson, Johanson and Springman have proposed mathematical formulations to describe the thermomechanical behavior of ice-rich frozen soils at temperatures close to 0 °C. They highlighted how ice content influences the apparent cohesion and the angle of internal friction. Moreover, apparent cohesion seems to be influenced by the temperature and the applied compression strain rate (Arenson & Springman, 2005). However, only limited analyses of apparent cohesion and friction angle have been carried out and further work is required.

In this paper, a series of temperature-controlled triaxial tests were performed at different temperatures with the aim of simulating the effect of thawing on permafrost. The samples were prepared artificially in order to ensure controlled and repeatable conditions. Thus, only the temperature variable varied during tests. The focus of the investigation presented in this paper was to determine the effect of temperature on the evolution of cohesion and the internal friction angle when samples of fine soil transition from a frozen state to a thawed state.

2. Current state of the applicants' research

Preliminary studies have been carried out on changes in soil strength parameters in order to assess the loss of bearing capacity of permafrost when it thaws (Torche & Prina Howald, 2017; Prina Howald & Torche, 2020). Direct shear tests at the Casagrande box and oedometer tests were performed on silty soils before, during and after a 15-day freezing phase at −15 °C. The result was an increase in soil compressibility of around 40% between soil in its natural state and soil that had undergone a freeze-thaw cycle. In addition, we estimated changes in the soil's angle of internal friction and cohesion by conducting direct shear tests using Casagrande box on samples that were initially frozen at −15 °C and then thawed. However, as the equipment used was not fully adapted to this type of protocol, the test conditions could not be fully controlled.

This preliminary study carried out at the HEIG-VD (High School of Engineering and Management of the canton of Vaud) in Switzerland has shown that soil properties are strongly affected by its physical state (frozen / unfrozen). In fact, the structure of the soil is significantly altered when it freezes. Figures 1 and 2 show the results of tomographic analysis of samples of silty-clay soil with sand and gravel in the frozen state and before freezing. The effect of frost on the structure of the soil is clearly visible.

Although the effects of frost on geomechanical parameters have been shown, the results obtained lack precision.
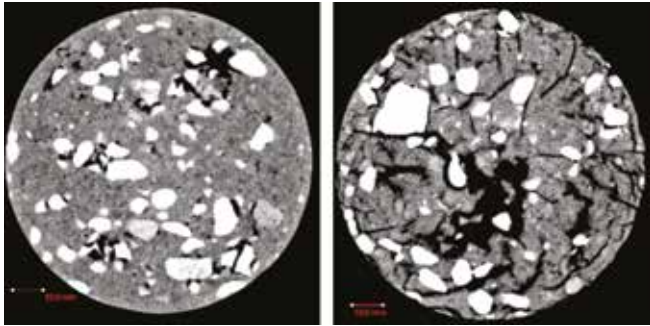
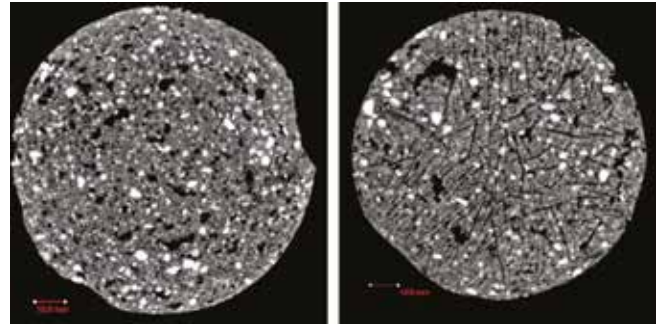Fig. 1 – Unsaturated A sample section before and during freezing.

Fig. 2 – Saturated sample B section before and during freezing.

3. Soil properties and test program

3.1. Classification

The soil analyzed in this study comes from the washing sludge of a lacustrine gravel near Neuchâtel Lake (fig. 3). The properties of the soil were determined according to Swiss standards VSS and listed in table 1. The soil is composed by 3% of sand, 69% of silt and 28% of clay. According to the USCS classification, the soil is a clay loam CL. (fig. 4). The frost sensitivity is very high: G4. According to the compaction test, the maximum dry density and optimum water content are 1.831 Mg/m³ and 14.4% respectively.

3.2. Sample preparation

In order to avoid mismatches in the results due to the natural heterogeneity of the soils, samples were prepared artificially under repeatable conditions. Thus, the variations observed between tests can be directly linked to the freeze/thaw effect. The compaction water content of the samples was set at 20% in order to obtain a degree of

saturation of around 85%. Then, saturation (Sr > 95%) was completed during the first step of the triaxial test. Water was mixed with

the soil powder to reach the target water content using a mechanical mixing machine. Then the soil was stored in a plastic bag until the

Fig. 3 – Localisation of the gravel in Switzerland.

Fig. 4 – USCS classification.

Tab. 1 – Physical properties of tested clay loam.

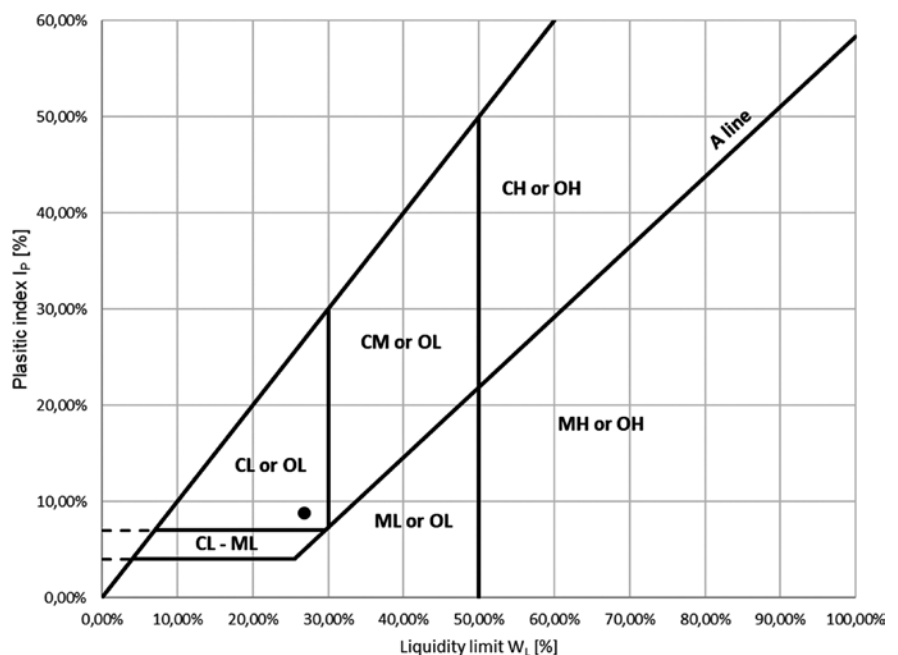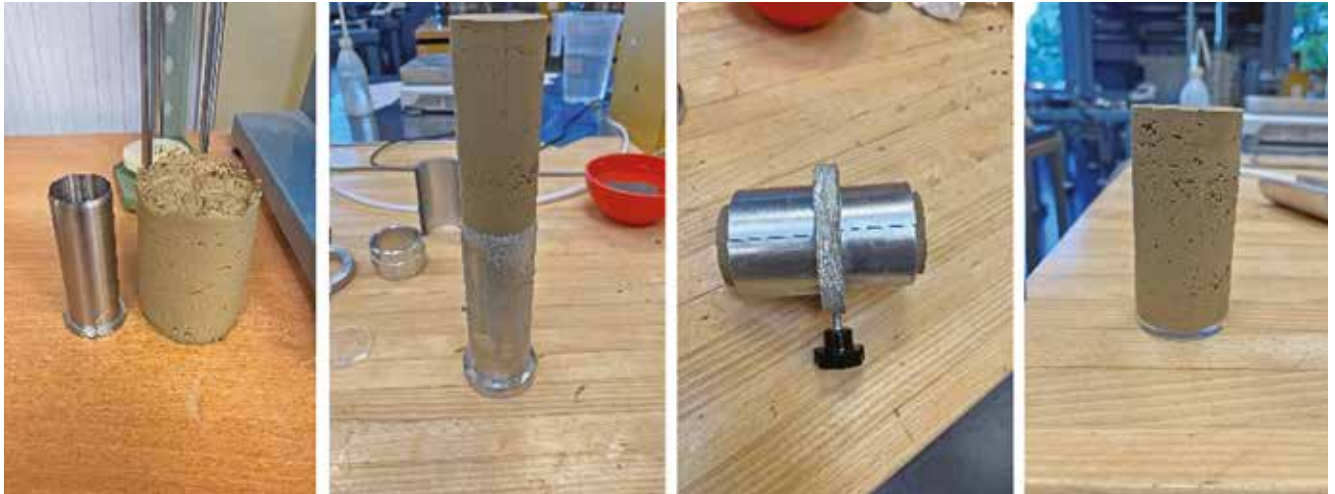| Sand [%]	Silty [%]	Clay [%]	Liquid limit [%]	Plastic limit [%]	Specific gravity [Mg/m³]
3.0	69.4	27.6	27.2	18.5	2.74

Fig. 5 – Sample preparation.

water was homogenously redistributed. The soil was compacted in a A-type Proctor mold (L = 119 mm and Ø = 101 mm) with an energy compaction of 0.6 MJ/m^3. This energy is used for the standard compaction test. Our compacter is set up for this energy, that is why we chose 0.6 Mj/m^3 compaction energy in order to limit the human error during the confection of the samples. Compaction was carried out in a mechanical compacter calibrated precisely for this energy. In that respect, the human errors during the confection of the samples were highly restrained. After extraction from the Proctor mold, the samples were cut in order to obtain a cylinder of 100 mm length and 50 mm diameter (fig. 5).

Finally, several tests were performed on artificial samples before freezing, including a CU+u triaxial test, to determine the reference properties of the specimens and are listed in table 2.

Tab. 2 – Reference properties.

γ [Mg/m^3]	w [%]	Sr [%]	e_0 [-]	c_u [kPa]	φ_u [°]
2.01	20.1	86.4	0.639	23.9	22.4

3.3. Test plan

In this study, a triaxial device with a thermal control was used to experimentally quantify the effect of thawing on the properties of frozen soils.

Initially, three triaxial tests were carried out on samples frozen at –5 °C, followed by three other tests performed at +5 °C.

The choice of the test type was therefore made for a consolidated undrained test (CU) for frozen sample and a consolidated undrained test with pore water pressure measurement (CU+u) for the thawed samples. The tests began with a step of saturation until the B check was bigger than 0.95. The cell pressure is gradually increased to 660 kPa while maintaining an effective pressure of 10 kPa. Then, samples were consolidated during 24 hours. The back pressure was maintained at 650 kPa and the cell pressure was increased to 750 kPa, 850 kPa, 1050 kPa and 1250 kPa. As these tests were innovative, we decided to use four samples per test and selected the three best Mohr circles for analyzing the results. After the consolidation step, samples were frozen at –5 °C temperature during 24 hours.

The temperature of the sample was controlled by a coil connected to the thermal controller (fig. 6). Liquid flows through the coil, heating or cooling the fluid inside the cell. The cell fluid is a mixture of demi-neralized water and antifreeze which helps maintain a liquid state during system cooling and facilitates the application of the cell pressure. A thermal sensor is integrated into the system to monitor the temperature of the containment fluid. After a freeze step of 24 hours at –5 °C, samples were sheared in the press at a speed of 0.02 mm/min. This speed was calculated in function of test conditions and the first curve of consolidation. The shear strength was measured every 0.1% of deformation.

For the tests after thawing, the
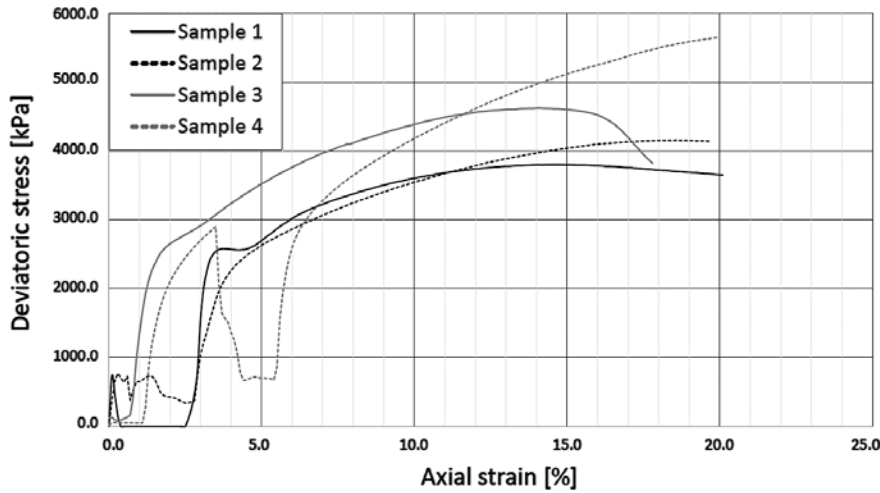

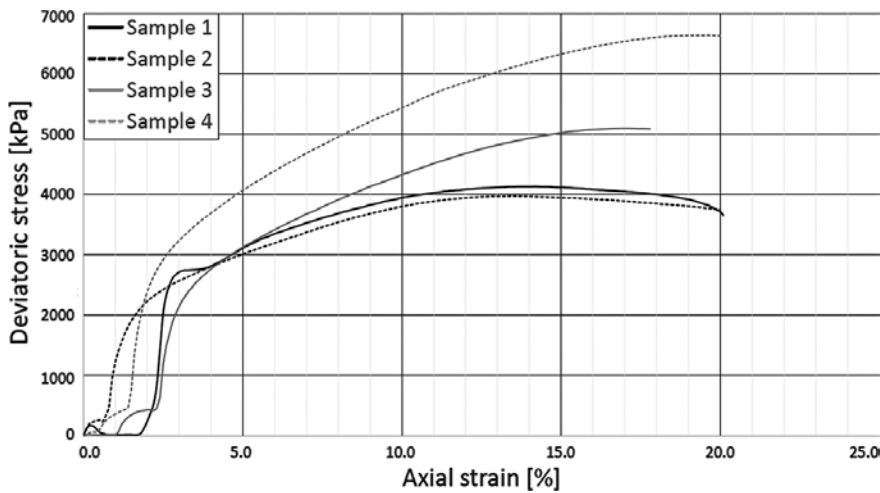Fig. 6 – System assembly.

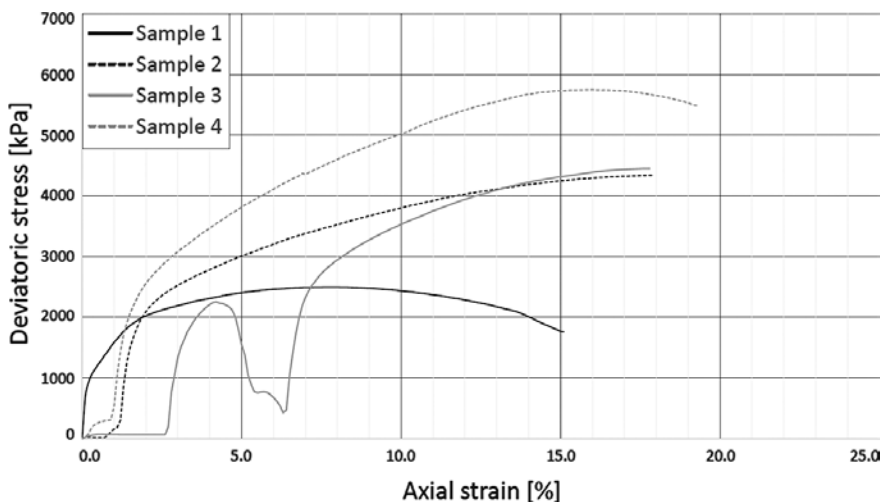Fig. 7 – Deviatoric curves, test 1 at –5 °C.

Fig. 8 – Deviatoric curves, test 2 at –5 °C.

Fig. 9 – Deviatoric curves, test 3 at –5 °C.

samples were frozen following the same procedure as for the frozen tests, then thawed at +5 °C during 12 hours before shearing.

After exploitation of the shear strength curves, we were able to determine the cohesion and the internal friction angle of the soil to compare the state during and after freezing.

4. Test results

4.1. Triaxial test at –5 °C

Interpreting the results of triaxial tests on frozen soils is complicated due to ice presence in the sample. This is why interpreting the stress-strain response of the samples required making certain choices to describe the results, as a standard triaxial test interpretation was not applicable for this type of test. Since the water in the samples was in an ice state, no pore water pressure could be measured. Therefore, the calculations were performed using total stress. Moreover, we assumed that the sample was totally frozen and could be considered as an impervious rock. Thus, we considered the cell pressure as the effective pressure.

The failure criterion adopted in this study was the peak deviatoric stress, unless it was not clearly visible. In which case values of deviatoric stress at a displacement of 15% were used. Some deviatoric stress curves did not show a clear increase upon loading (fig. 7). This effect is due to the engage system of the triaxial press and was taken into account when measuring the

Tab. 3 – Raw results of tests at –5 °C.

		Effective pressure [kPa]	Deviatoric stress peak [kPa]	Axial strain peak [%]
Test 1	sample 1	750.8	3741.5	17.5
	sample 2	850.9	4148.5	17.8
	sample 3	1050.4	4559.0	15.7
	sample 4	1250.3	5262.3	16.1
Test 2	sample 1	750.7	4055.6	16.8
	sample 2	850.5	3932.9	15.7
	sample 3	1050.4	5096.8	17.2
	sample 4	1250.3	6487.9	16.4
Test 3	sample 1	750.8	2497.2	8.0
	sample 2	850.4	4303.1	16.2
	sample 3	1050.4	4449.5	17.8
	sample 4	1250.4	5479.1	16.0

peak of deviatoric stress.

As triaxial tests on frozen ground are rare, we decided to carry out four shear tests per test in case one result was inconsistent with the others. This choice proved to be very useful, because as expected, some points were discarded in order to obtain consistent results. Figures 7, 8 and 9 show the curves of deviatoric stresses. Table 3 summarises the raw results of the three triaxial tests at −5 °C.

4.2. Triaxial test at +5 °C

The analysis of these tests was more conventional. In these cases, the water inside the specimens returned to a liquid phase allowing the pore water sensor to record usable data. As for the tests conducted at −5 °C, deviatoric stress peaks were recorded at 15% displacement (with correction applied) if no peaks were initially observed. Figures 10, 11 and 12 show the curves of deviatoric stresses and table 4 summarises the raw results of the three triaxial tests at +5 °C.

Tab. 4 – Raw results of test at 5 °C.

		Effective pressure [kPa]	Deviatoric stress peak [kPa]	Axial strain peak [%]
Test 1	sample 1	99.5	295.4	17.0
	sample 2	199.7	479.4	15.7
	sample 3	399.9	845.8	19.6
Test 2	sample 1	99.8	268.8	15.6
	sample 2	199.7	467.1	15.5
	sample 3	399.8	857.5	16.3
Test 3	sample 1	99.7	262.0	16.3
	sample 2	199.8	424.0	15.7
	sample 3	399.9	808.2	17.1

Fig. 10 – Deviatoric curves, test 1 at 5 °C.

Fig. 11 – Deviatoric curves, test 2 at 5 °C.

Fig. 12 – Deviatoric curves, test 3 at 5 °C.

5. Discussion
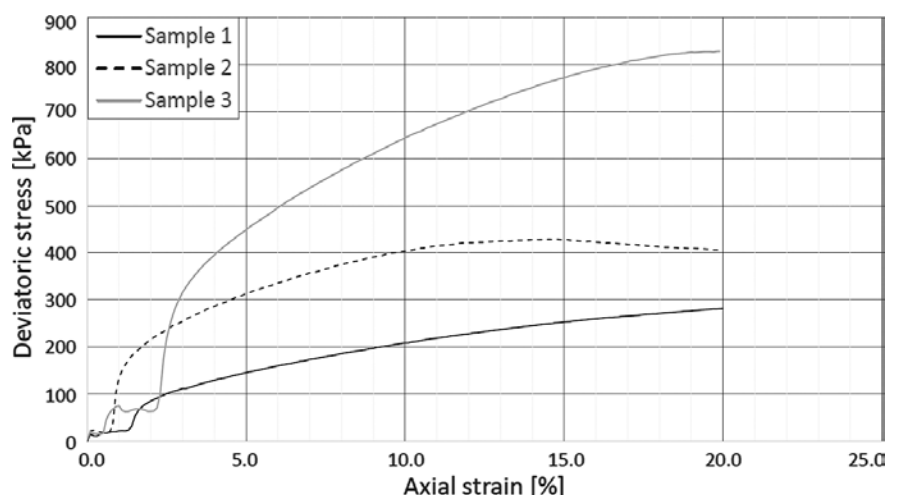
The failure behavior of the samples was generally ductile, although some samples exhibited very pronounced failure planes with a sharp drop in deviatoric stress, such as the sample at 1050kN/m² from test 1 at −5 °C (fig. 13), the other specimens showed predominantly a ductile failure in barreling mode.

As mentioned before, the analysis of the freezing triaxial test re-

Fig. 13 – Sample 3 of test 1 at –5 °C.

sults was difficult. Figures 14, 15 and 16 are the representation of Mohr's circles for the three tests carried out at a temperature of –5 °C. As mentioned in chapter 4, we have considered the frozen samples as a single-phase block, which implies that the cell pressure is equal to the effective pressure of the sample. For each test, sigma 3 is equal to the confining pressure and sigma 1 is the sum of sigma 3 and the deviatoric stress peak.

The difficulty arises in plotting the Mohr-Coulomb line. Mohr's circles did not align perfectly in tests 2 and 3 at –5 °C, making it challenging to draw a tangent line. In contrast, the first test at –5 °C was pretty easy to exploit.

The Mohr-Coulomb line was tangent to the four circles as shown in figure 14.

It can be seen in figure 15 that the Mohr's circle drawn with the results of sample 2 is smaller than the circle of sample 1. There were therefore two possible Mohr-Coulombs lines, the first being the tangent to circles 1, 3 and 4 and the second being the tangent to circles 2, 3 and 4. The second solution was discarded because it gave a soil cohesion value below 0 kPa,

which is impossible. We can therefore conclude that the shearing of sample 2 encountered a problem that led to a low shear strength.

The analysis of the third test at –5 °C presented the greatest challenge. To visualize the issue, two Mohr Coulomb lines were drawn in figure 16. The first Mohr-Coulomb line was constructed using data from samples 1, 3 and 4. Although the line was perfectly tangent to the three circles, this line has been discarded for the fol-
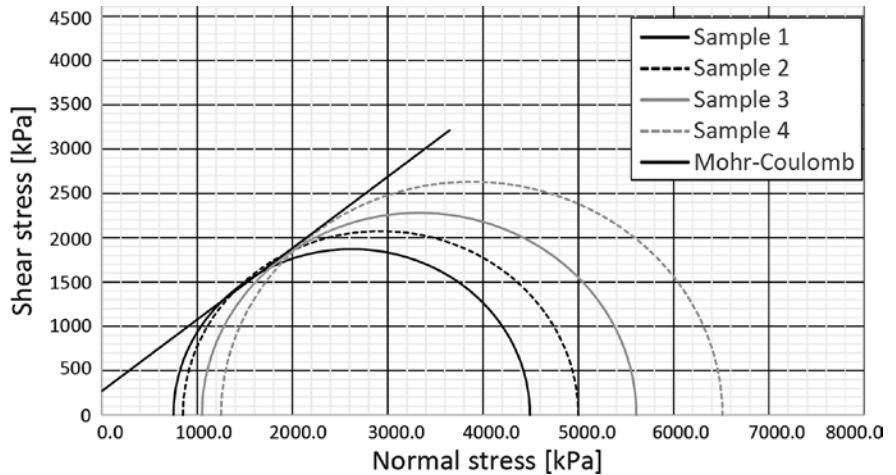

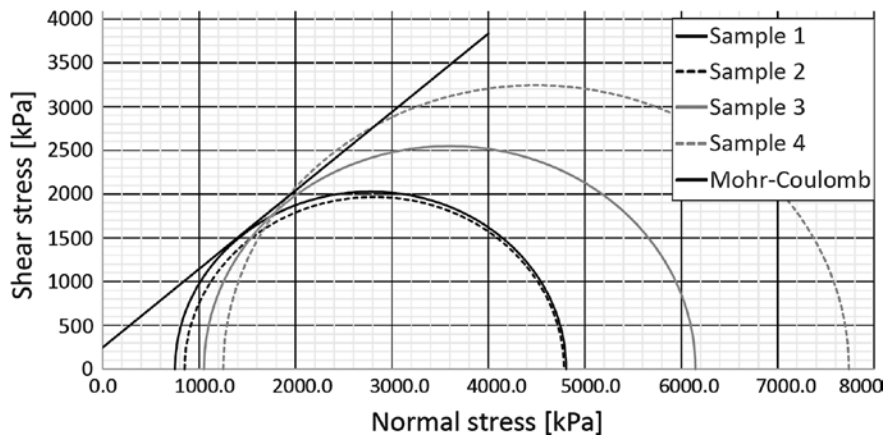Fig. 14 – Test 1 at a temperature of –5 °C.
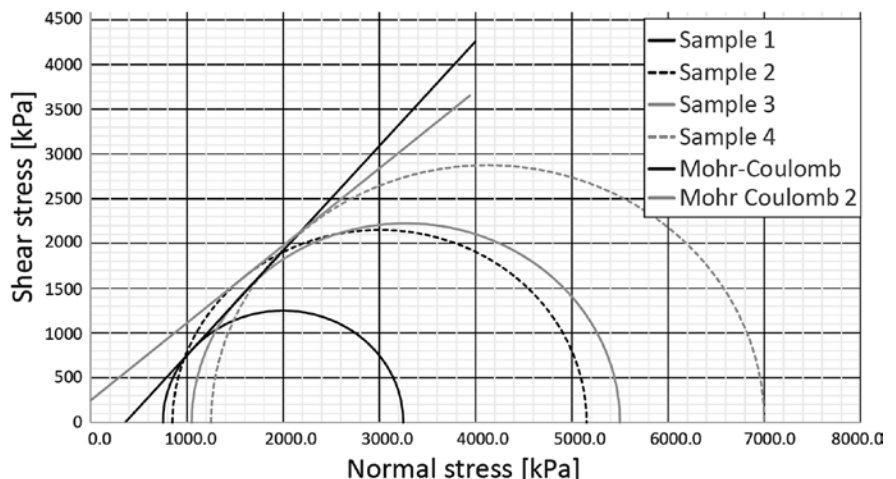

Fig. 15 – Test 2 at a temperature of –5 °C.

Fig. 16 – Test 3 at a temperature of –5 °C.

lowing reasons. Firstly, the deviatoric stress curve of sample 1 exhibited an unusual pattern, with the deviatoric stress peak occurring at an 8% axial strain rate. This value is abnormally low compared to all other tests, roughly half as much and there is no clear evidence of failure. It is likely that the sample had a design flaw, resulting in low shear strength. Secondly, the circle from the results of the third sample is clearly not usable. We can see on figure 16 that the Mohr's circle is smaller than sample 2 for a higher effective stress. This is probably due to the pre-failure visible on figure 9 at 4.5% of deformation. Thirdly, the first Mohr-Coulomb line was not correct because it led to a negative cohesion. That is why we have drawn a second Mohr-Coulomb line tangent to the circles 2 and 4. This line led to a realistic result.

Table 5 summarizes the results of the tests at –5 °C. The results of cohesion and internal friction angle are very similar for the three tests. As expected, the cohesion of the soil increased a lot during the freezing phase. Compared to its initial state, the cohesion of the soil is 10.6 times higher and the internal friction angle is 1.8 times higher. The phase change in soil significantly impacts its mechanical properties.

Tab. 5 – Summary of cohesion and friction angle during freezing.

	Cohesion [kPa]	Internal friction angle [°]
Test 1	268.97	38.89
Test 2	245.47	41.91
Test 3	246.95	40.84
Mean	253.80	40.55
Standard deviation	13.16	1.53

Analyzing the test after the freezing cycle at –5 °C and subsequent thawing at +5 °C did not pose significant difficulties. The alignment of the Mohr-Coulomb lines is almost perfect on all three tests (fig. 17, 18 and 19). On top of that,
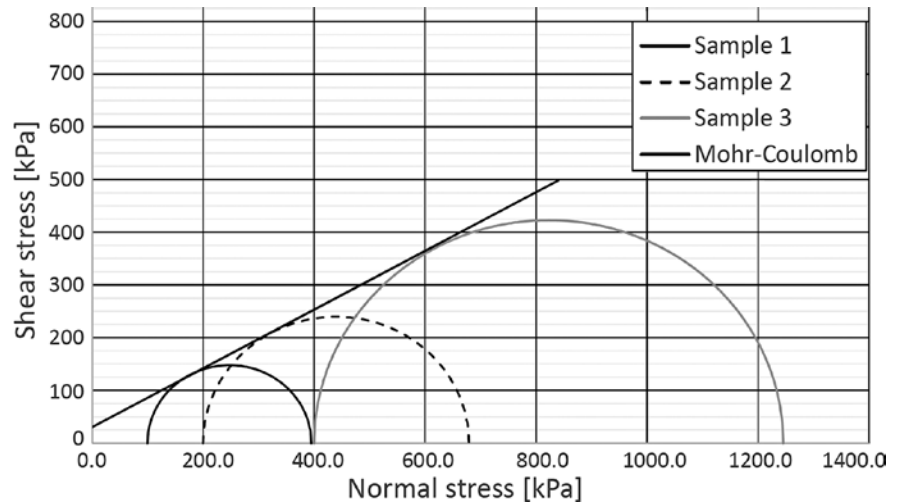
Fig. 17 – Test 1 at a temperature of 5 °C.
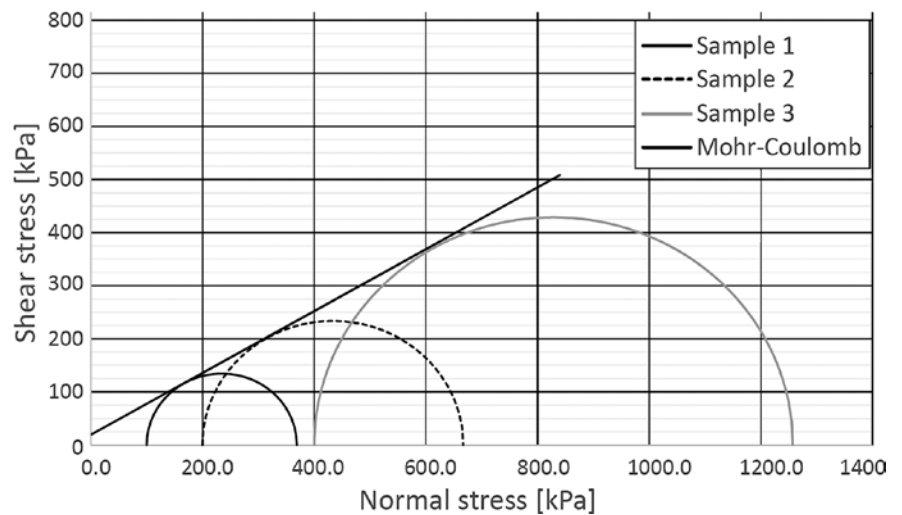
Fig. 18 – Test 2 at a temperature of 5 °C.

Fig. 19 – Test 3 at a temperature of 5 °C.

no anomalies have been detected on the deviatoric curves.

Table 6 summarizes the results of the tests at +5 °C. The first ob-

servation that we could do is the strong decrease of cohesion and internal friction angle after the specimens thawed. Compare to its frozen state, the soil cohesion has decreased by a factor of 10 during the thawing step. The interesting thing is that the cohesion seems to return to its initial value before any freeze/thaw effect even if the value is slightly higher than the initial state. We can, however, question the significance of this increase. Indeed, the initial cohesion of the soil is close to the average value after thawing. Moreover, the standard deviation of the cohesion is quite high and covers the difference between the two values.

Although the effect of one freeze / thaw cycle does not seem to affect significantly the cohesion value, the same is not true for the internal friction angle. Strong changes in the value of the internal friction angle can be identified in all states. When the sample is frozen, friction angle increases by about 81% compared to its initial state. Then during thawing, friction angle decreases by 27.4%. However, after the freeze-thaw cycle, the value of friction angle remains about 30% higher than its pre-freeze state. The results obtained by the six tests (3 during freezing, 3 after thawing) are very close and the standard deviations are low. A phenomenon in the soil occurs during freezing that permanently alters their initial internal friction angle. We can propose various hypotheses regarding its origin. A probable rearrangement of the solid skeleton during the gel phase is one of them. To determine more precisely the cause of this phenomenon, further studies are necessary.

It should also be noted that when the soil goes from the frozen to the thawed state, its mechanical properties decrease very sharply (approximately 10-fold decrease

in cohesion and 30% decrease in friction angle). These changes lead to a sharp decline in the bearing capacity of the soil. The loss of bearing capacity also depends on other factors that are specific to each infrastructure (type of foundation, depth of foundation etc.) and therefore cannot be accurately quantified in a general way.

Tab. 6 – Summary of cohesion and friction angle after thawing.

	Cohesion [kPa]	Internal friction angle [°]
Test 1	30.54	29.12
Test 2	17.64	30.39
Test 3	22.60	28.84
Mean	23.59	29.45
Standard deviation	6.51	0.83

6. Conclusion

This study aimed to experimentally quantify the effect of thawing on a reconstituted soil's geomechanical strength. For this purpose, a classification of soil geomechanical parameters was first established to serve as a reference point. Then, three triaxial shear tests at a temperature of –5 °C were performed. This temperature was chosen to be slightly lower than that measured in permafrost monitoring boreholes in the Alps (Switzerland and France). Three additional tests were carried out at a temperature of 5 °C after being frozen for 24 hours at a temperature of –5 °C.

These tests highlighted the importance of soil condition (frozen/thawed) on soil cohesion. Indeed, cohesion varies by a factor of 11 between these two states. Nevertheless, the value of the cohesion seems to return to its initial state after thawing. Soil cohesion seems to depend only on the state of the

soil (frozen/thawed) but it would be interesting to perform additional tests at different temperatures to confirm this hypothesis.

The variation in the soil's friction angle is less pronounced than that in cohesion. When the soil thaws, friction angle decreases by about 30% of its value. It should be noted that this angle increases sharply when the soil is frozen (+81% compared to its initial state). The most surprising thing is that the value of friction angle does not return to its initial state, unlike cohesion. This may indicate two things:

Either the freeze-thaw cycle causes a fundamental change in soil properties. The soil cannot return to its original mechanical properties.

Either the mechanical parameters of the soil are strongly temperature dependant.

Or a combination of these two facts.

This study should also be completed with additional tests at other temperatures to verify these hypotheses.

Understanding the impacts of permafrost thaw is complex. That is why, further studies on this topic are strongly recommended. The more studies are carried out on the subject, the more we will be able to understand the impact of global warming on permafrost, and therefore the impact on human kind and its environment.

References

Arenson, L., Hoelzle, M., Springman, S., (2002). Borehole deformation measurements and internal structure of some rock glacier in Switzerland. Permafrost and periglacial processes, Volume 13, pp. 117-135. https://doi.org/10.1002/ppp.414

Arenson, L., Springman, S., (2005). Mathematical descriptions for the beha-

viour of ice-rich frozen soils at temperatures close to 0 °C. Canadian Geotechnical Journal, pp. 431-442. https://doi.org/10.1139/t04-109

Bardou, E., Favre-Bulle, G., Ornstein, P., Rouiller, J.-D., (2011). Influence of the connectivity with permafrost on the debris-flow triggering in high-alpine environment. Engineering Geology and the Environment, Volume 10, pp. 13-21. https://doi.org/10.4408/IJEGE.2011-03.B-002

Blikra, L.H., Christiansen, H.H., (2014). A filed-based model of permafrost-controlled rockslide deformation in northern Norway. Geomorphology, Volume 208, pp. 34-49. https://doi.org/10.1016/j.geomorph.2013.11.014

Chamberlain, E., Gow, A., (1979). Effect of Freezing and Thawing on the Permeability and Structure of Soils. Developments in Geotechnical Engineering, Volume 26, pp. 73-92. https://doi.org/10.1016/B978-0-444-41782-4.50012-9

Damm, B., Felderer, A., (2013). Impact of atmospheric warming on permafrost degradation and debris flow initiation – a case study from the eatern European Alps. Quaternary Science journal, 62(2), pp. 136-149. https://doi.org/10.3285/eg.62.2.05

Ding, Y. et al., (2019). Global warming weakening the inherent stability of glaciers and permafrost. Science bulletin, Volume 64, pp. 245-253. https://doi.org/10.1016/j.scib.2018.12.028

Dysli, 1993. Where does the water go during ice lenses thaw?. Anchorage, s.n., pp. 45-50.

Etzelmüller, B., Berthling, I., Sollid, J.L., 2003. Aspects and concepts on the geomorphological significance of Holocene permafrost in southern Norway. Geomorphology, Volume 52, pp. 87-104. https://doi.org/10.1016/S0169-555X(02)00250-7

Farbrot, H., Isaksen, K., Etzelmüller, B., Gisnas, K., (2013). Ground thermal regime and permafrost distribution under a changing climate in Northern Norway. Permafrost and periglacial processes, Volume 24,
pp. 20-38. https://doi.org/10.1002/ppp.1763

Frauenfelder, R., Isaksen, K., Matthew, J.L., Noetzli, J., (2018). Ground thermal and geomechanical conditions in a permafrost-affected high-latitude rock avalanche site (Polvartinden, northern Norway). The cryosphere, Volume 12, pp. 1531-1550. https://doi.org/10.5194/tc-12-1531-2018

Guo, D., Wang, H., Li, D., (2012). A projection of permafrost degradation on the Tibetan Plateau during the 21st century. Journal of Geophysical research, Volume 117. https://doi.org/10.1029/2011JD016545

Haeberli, W., (1992). Construction, Environmental problems and natural hazards in periglacial mountain belts. Permafrost and periglacial processes, Volume 3, pp. 111-124. https://doi.org/10.1002/ppp.3430030208

Hilger, P. et al., (2021). Permafrost as a first order control on long-term rock.slope deformation in (Sub-)Arctic Norway. Quaternary Sciences Reviews, Volume 251. https://doi.org/10.1016/j.quascirev.2020.106718

Hipp, T., Etzelmüller, B., Farbrot, H., Schuler, T.V., (2011). Modelling the temperature evolution of permafrost and seasonal frost in southern Norway during the 20th and 21st century. The cryosphere discussions, Volume 5, pp. 811-854. https://doi.org/10.5194/tcd-5-811-2011

Isaksen, K. et al., (2011). Degrading mountain permafrost in Southern Norway : spatial and temporal varaibility of mean ground temperatures, 1999-2009. Permafrost and Periglacial Processes, Volume 22, pp. 361-377. https://doi.org/10.1002/ppp.728

Isaksen, K. et al., (2002). Mountain permafrost distribution in Dovrefjell and Jorunheimen, southern Norway, based on BTS and DC resistivity tomography data. Norwegian journal geography, 56(2), pp. 122-136. https://doi.org/10.1080/002919502760056459

Isaksen, K., Holmlund, P., Sollid, J.L., Harris, C., (2001). Three deep alpine-permafrost boreholes in Svalbard
and Scandinavia. Permafrost and periglacial processes, Volume 12, pp. 13-25. https://doi.org/10.1002/ppp.380

Lyon, C. et al., (2022). Climate change research and action must look beyond 2100. Global Change Biology, Volume 28, pp. 349-361. https://doi.org/10.1111/gcb.15871

Matthews, J.A. et al., (2018). Small rock-slope failures conditioned by Holocene permafrost degradation: a new approach and conceptual model based on Schmidt-hammer exposure-age dating, Jotunheimen, southern Norway. An international journal of quaternary research, Volume 47, pp. 1144-1169. https://doi.org/10.1111/bor.12336

Myhra, K.S., Westermann, S., Etzemüller, B., (2017). Modelled distribution and temporal evolution of permafrost in steep rock walls along a latitudianal transect in Norway by CryoGrid 2D. Permafrost and Periglacial Processes, Volume 28, pp. 172-182. https://doi.org/10.1002/ppp.1884

Perov, V., Chernomorets, S., Budarina, O., (2017). Debris flow hazards for mountain regions of Russia: regional features and key events. Springer, pp. 199-235. https://doi.org/10.1007/s11069-017-2841-3

Prina Howald, E., Bonnard, C., Laloui, L., (2016). TR3 project: slope safety preparedness for effects of climate change contribution for Switzerland. Dans: H. Ken, S. Lacasse, L. Picarelli, éds. Slope Safety Preparedness for Impact of Climate Change. London: CRC Press. https://doi.org/10.1201/9781315387789

Prina Howald, E., Torche, J., (2020). Global warming and loss of bearing capacity of permafrost : an experimental study on the effects of freezing/thawing cycles on a silty soil. Global Journal of Earth Science and Engineering, Issue 7, pp. 1-21.

Saemundsson, P. et al., (2018). The triggering factors of the Moafellshyrna debris slide in northern Iceland : intense precipitation, earthquake activity and thawing of mountain permafrost. Science of the total en-

vironment, Volume 621, pp. 1163-1175. https://doi.org/10.1016/j.scitotenv.2017.10.111

Sattler, K., Keiler, M., Zischg, A., Schrott, L., (2011). On the connection between debris flow activity and permafrost degradation: a case study from the schnalstal, South Alps, Italy. *Permafrost and periglacial precesses,* Volume 22, pp. 254-265. https://doi.org/10.1002/ppp.730

Stoffel, M., Bollschweiler, M., Beniston, M., (2011). Rainfall characteristics for periglacial debris flows in the Swiss Alps: past incidences – potential future evolutions. *Climatic Change,* Volume 105, pp. 263-280. https://doi.org/10.1007/s10584-011-0036-6

Torche, J., Prina Howald, E., (2017). Influence of the climate change on the evolution of soil bearing capacity : an experimental study on the effects of freezing/thawing cycles. *IX Simposio Nacional sobre Taludes y Laderas Inestables,* pp. 295-306.

Zhang, Y., Chen, W., Riseborough, D.W., (2008). Transient projections of permafrost distribution in Canada during 21st century under scenarios of climate change. *Global and Planetary Change,* Volume 60, pp. 443-456. https://doi.org/10.1016/j.gloplacha.2007.05.003

Preliminary statistical analysis of borehole and geological data from the Po plain

Christoforos Benetatos*

* Politecnico di Torino, DIATI, Torino

Corresponding author:
christoforos.benetatos@polito.it

The Po Plain area in the north of Italy can be considered a natural geological and geophysical laboratory due to its complex geological evolution, particularly from the Miocene to today. Much of our understanding about the subsurface of the Po Plain is due to the large amount of data collected during the period of hydrocarbon exploration in Italy. In total more than 7000 wells have been drilled and thousands of km of seismic acquisition lines have been acquired. Furthermore, the study of the natural gas fields contributed with additional data facilitating the creation of detailed structural and stratigraphic models of the subsurface. The majority of the "original" data, including well logs, seismic and geological profiles existed in paper format thus posing challenges for their integration into modern models where digital data are incorporated to achieve a sound description of the subsoil. Livani et al. (2023) have collected and digitized a large number of "original" data and subsequently used them to recreate the overall subsurface architecture of the Po plain and extract the physical properties of the main geological units. In this study, we use the results of the work of Livani et al. and we perform a preliminary statistical analysis on them. We explore relationships between rock density and geological formations, we compare log data (GR, sonic) with lithologies and we investigate the lithological content for each of geological formations. Ultimately, we compare some of our results with previously published research.

Keywords: *Po plain, sonic log, lithology, P-wave velocity.*

1. Introduction

In Italy, hydrocarbon reservoirs are located along the Apennines, in foredeep basins, and off-shore, along the Adriatic foreland. Most of the gas accumulations were found in the Po Plain and the northern Adriatic Sea while oil accumulations were typically identified along the Southern Apennines and Sicily (Bertello *et al.*, 2010, Cazzini *et al.*, 2018). The distribution of hydrocarbon reservoirs onshore and offshore in Italy highlights the close connection between the evolution of the chain-foredeep-foreland system and the origin of reservoir rocks and traps for the accumulation of oil and gas (Casero, 2004; Casero and Bigi, 2013). Since the second half of the 20th century, the discovery and exploitation of numerous hydrocarbon reservoirs, primarily gas-bearing, have played a pivotal role in Italy's economic advancement. The Po

Plain and the adjacent northern Adriatic Sea have emerged as the primary hosts for hydrocarbon fields in the nation, contributing to nearly 1/3 of the national gas production (Livani *et al.*, 2023). From the mid of the mid-20th century and once the gas reservoirs reached the end of their lifecycle, some of them have been converted into gas storage that are still active nowadays. Eni-Agip company performed large-scale exploration activities throughout the Po Plain and central and Northern Adriatic Sea acquiring a large volume of subsurface data that included 2D and 3D seismic surveys in local and regional scale and well-log data during the drilling of exploration or development wells. Most of the subsurface information coming from the wells is available in the form of well profiles (scale 1:1000) that include a substantial quantity of sedimentological, stratigraphic and structural information. In this

study we use the well-log data present in the database of Livani *et al.*, 2023 in order to perform a preliminary statistical analysis using digitized well logs recordings, lithological and stratigraphic information.

2. Regional geology

The geological framework of the areas containing hydrocarbon reservoirs is the outcome of a complex tectono-stratigraphic evolution marked by a Mesozoic extensional phase, primarily accompanied by carbonate sedimentation (fig. 1). This was followed by a Cenozoic compressional phase associated with the deposition of thick turbidite sequences. The period extending from the Mesozoic through the Lower Paleogene was marked by the formation of important carbonate platform sequences, accompanied by deposits of platform margin and slope, primarily represented by carbonate breccias, and intra-platform basins that characterize the entire peri-Adriatic area. In more recent times the sedimentation in the foredeep was characterized by the deposition of thick clastic successions derived from the erosion of the mountain chains themselves. The Oligo-Miocene foredeep succession comprises a series of turbidite sequences associated with

> If there are references to colour figures in the text, the articles are available in open-access mode on the site www.geam-journal.org

different orogenic phases. From the Messinian to Pleistocene the basin accumulated thick turbidite sequences, reaching thicknesses of 7000-8000 meters, linked to the advancement of the Apennine front that led to the gradual filling of the Po Basin. (e.g. Casnedi *et al.*, 1982; Dondi *et al.*, 1982; Casero, 2004; Fantoni *et al.*, 2004; Fantoni & Franciosi, 2010; Ghielmi *et al.*, 2010 among others).

From a structural and stratigraphic perspective, the most common geological scenarios associated with hydrocarbon reservoirs in Italy are represented by:
1. Deep structures within carbonate successions, primarily linked to Mesozoic extensional phases or their subsequent tectonic inversion.
2. Anticlines within the Tertiary succession associated with south Alpine or Apennine-vergent thrusts connected to the structuring of the two orogenic mountain chains.
3. Gentle, very shallow anticlines developed between the Upper Pliocene and Quaternary.

Specifically, thermogenic oil and gas reservoirs are mainly associated with Mesozoic carbonate successions, while gas reservoirs are primarily linked to Oligo-Miocene foredeep clastic successions (thermogenic gas) and Plio-Pleistocene formations (biogenic gas).

3. Data digitization

The data used in this study are part of the database made available by Livani *et al.* (2023). Their database was created by the collection, digitization, and revision of geological and geophysical data (in raster format) that was derived from public sources. The fundamental source of well data was the VIDEPI project database (http://www.videpi.com) which is the outcome of the collaboration between the Ministry for Economic Development – DGRME, the Italian Geological Society and Assomineraria (the Italian petroleum and mining industry association, now Assorisorse). The main objective was to

allow everyone easy access to all documentation related to Italian oil and gas exploration. This comprehensive database encompasses public well data, documents, mining permits, and concessions submitted to UNMIG, the National Mining Office for Hydrocarbon and Geothermal Energy under the Ministry for Economic Development, since 1957 (Benetatos *et al.*, 2019).

The well-log database of Livani *et al.* comprises digitized data from 160 wells (originally in raster format) located in the Po plain area and the northern Adriatic Sea (fig. 2). The master logs at a 1:1000 scale include a standard set of logs that offer information on lithology, stratigraphy, and fluid saturation. The primary dataset comprises a Spontaneous Potential (SP) log, employed for lithological characterization and stratigraphic correlations, and a Resistivity (Res) log for identifying hydrocarbon-bearing layers. Supplementary data pertains to lithological characteristics (e.g., cuttings and lithological classifications along
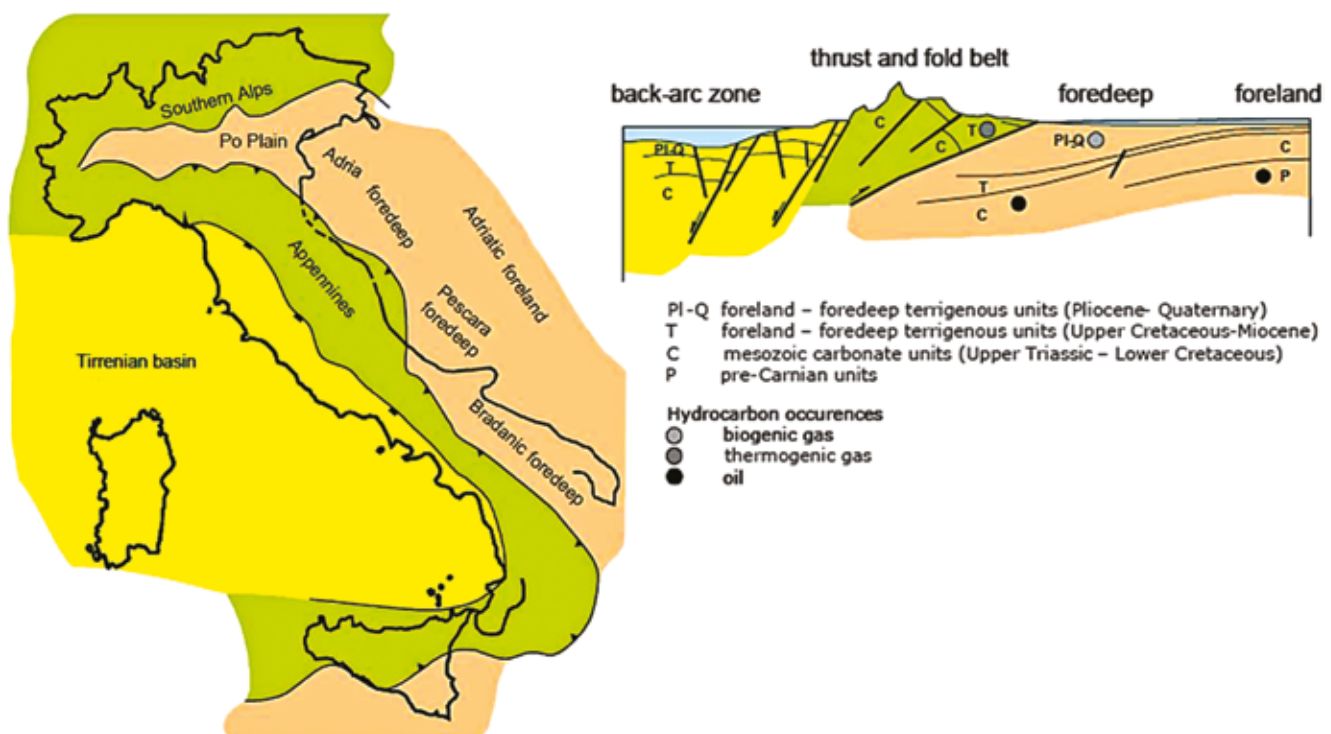

Fig. 1 – Location scheme of the principal gas and oil reservoirs in the Italian geological context (fig. mod. from Bertello *et al.*, 2008).
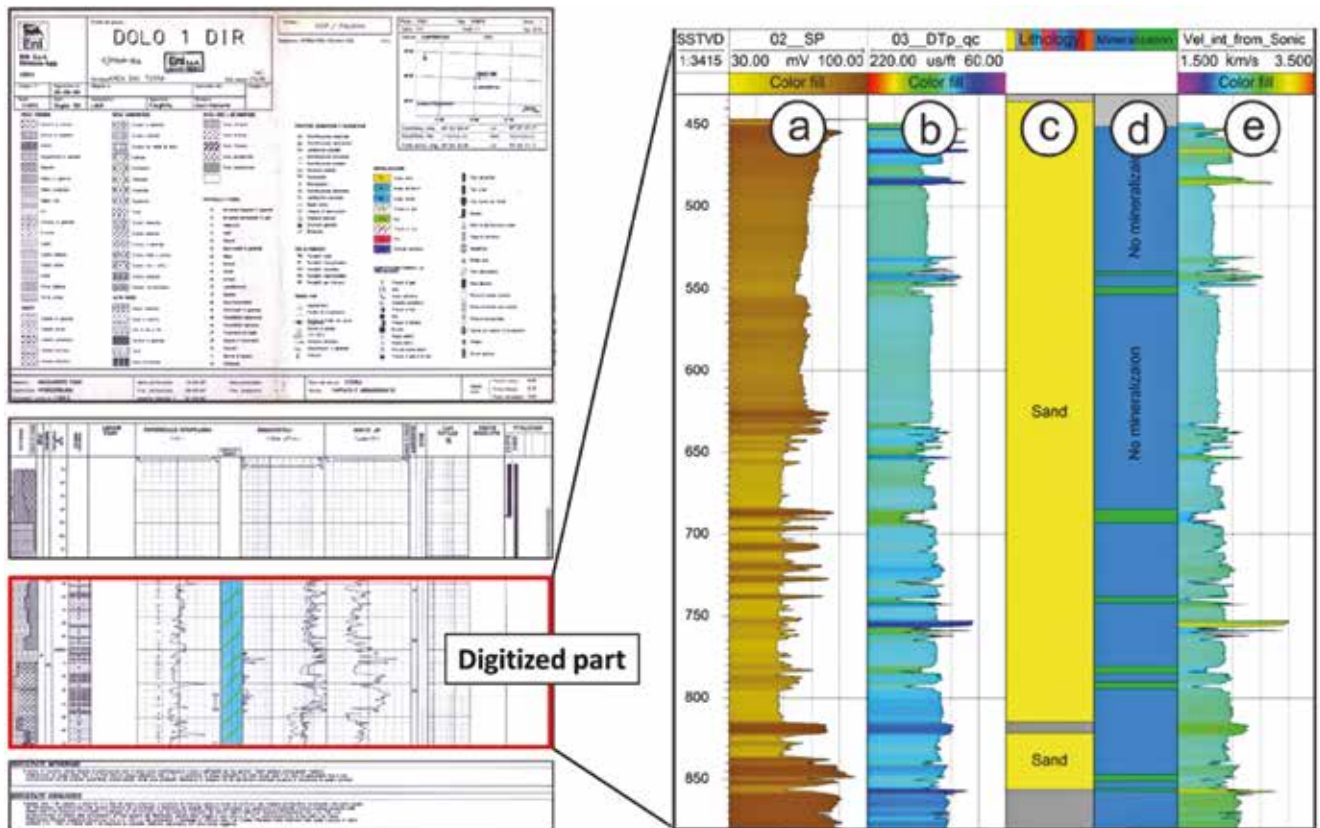
Fig. 2 – (Left) Typical example of well profile (scale 1:1000) from the Po plain area. (Right) Example of a typical logset of the wells in the database. a) Spontaneous Potential log, b) Sonic log, c) Lithological log, d) Mineralization log, e) Sonic velocity log.

the wellbore). Occasionally, Sonic log registrations useful for the calculation of seismic sonic velocities were also available. The digitization procedure was performed manually, with a variable sampling step, or by a semi-automatic method of line recognition and the logs were resampled in steps of 0.5 m.

3.1. Results of the digitization process

The digitization process and the subsequent data analysis led to a variety of stratigraphic, lithological and geophysical results. For the large-scale stratigraphy analysis, the digitized logs, in particular SP and GR were used to perform stratigraphic correlation between the wells at the regional scale. They provided insight into the subsurface stratigraphy by identifying units showing different lithological properties and defining horizons

that divide the geological succession into different parts based on their mechanical properties. The main recognized units were (Livani *et al.*, 2023):
1. Recent clastic deposits of the Po Plain and the Adriatic Sea (hereafter called "**Alluvium**")
2. Late Pliocene-Pleistocene sand-rich sequences (eg. Sand of the Asti Fm, hereafter called "**Pleistocene**")
3. Late Miocene-late Pliocene clastic deposits (e.g. Argille del Santerno Fm./P.to Corsini Fm./P.to Garibaldi Fm., hereafter called "**Pliocene**")
4. Early-late Miocene marly sequences (e.g. Marne di Gallare, hereafter called "**Miocene**")
5. Triassic to Eocene carbonate units (hereafter called "**Triassic**")
6. Varyscan crystalline basement
The adopted names chosen for the 5 main recognized units are hereafter for the sake of simplicity. The

Varyscan crystalline basement is intercepted for very few meters only by 5 wells and since it does not belong to the sedimentary fill of the Po Plain it will not be mentioned or used in the analysis here below.

The lithological analysis was performed by evaluating the information coming from the cuttings description of each well. The cuttings description compiles data acquired during mud logging, involving rock fragments brought to the surface as a result of drilling fluid circulation within the borehole. These mud logging observations were integrated with SP and GR logs, as well as lithological data obtained from core sample analyses recorded in the well profile. This combined dataset was used to establish the lithological characteristics throughout the entire well. Livani *et al.*, 2023 were able to identify 9 macro-lithologies that are (Livani *et al.*, 2023):

Gravel – Sand – Cemented sands – Shale – Sand/Shale alternances – Conglomerates – Marls – Dolomites – Limestone

Within each macro-lithology group, there are also similar lithologies included alongside the primary one. This decision was made to simplify the classification process. For example, the "Sand" macro-lithology group includes also reported lithologies such as "Sand prevalent", "Fine sand", "Sand and shaly sand" and so on.

The geophysical/geomechanical outcome of the digitization process was the calculation of sonic slowness time (µsec/ft) that was later converted to sonic P-wave seismic velocities (m/sec) for all the wells having available registrations of the sonic log. Seismic velocity information along the wellbore is of particular importance since it can be used for the calculation of mechanical properties necessary for geomechanical simulations (e.g. Benetatos *et al.*, 2015, 2017, 2020) during the injection of various types of fluids in the subsurface such as natural gas, CO_2 or H_2. The sonic transit times varied from a maximum of almost 200 µsec/ft for the most superficial geological layers to a minimum of almost 40 µsec/ft for the deepest formations.

4. Preliminary statistical analysis

In this study, we used the results of the digitization and log analysis presented in par. 3 in order to investigate the relationship between lithologies, geological formations and seismic velocities. The first observation that we can extract from the well data of the database is the depth range that they cover inside the Po Plain's subsurface. The bottom hole depth, that is the maximum drilled depth of a well expres-
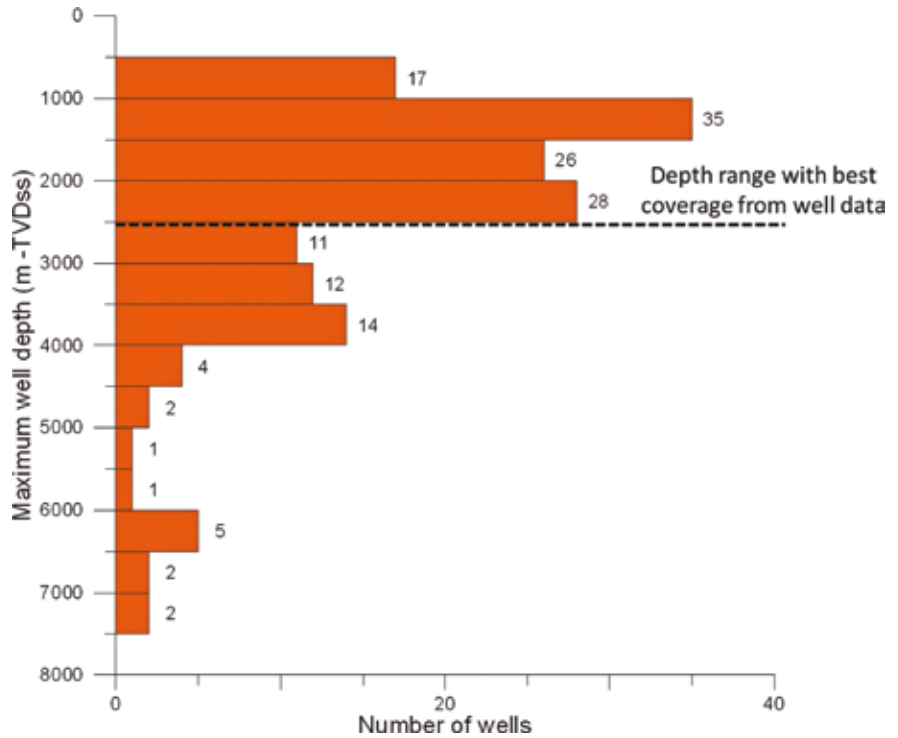

Fig. 3 – Histogram of the bottom hole depth of the wells present in the database.

sed in meters True Vertical Depth Sub Sea (m TVDss) is presented in fig. 3. Most of the wells (almost 90 wells) sample the range down to almost 2500 m, covering very well the upper portion of the ba-

sin, some wells arrive to the middle part while very few wells sample the deeper parts of the basin.

Figure 4 illustrates the depth range covered by the primary stratigraphic units. The boundary
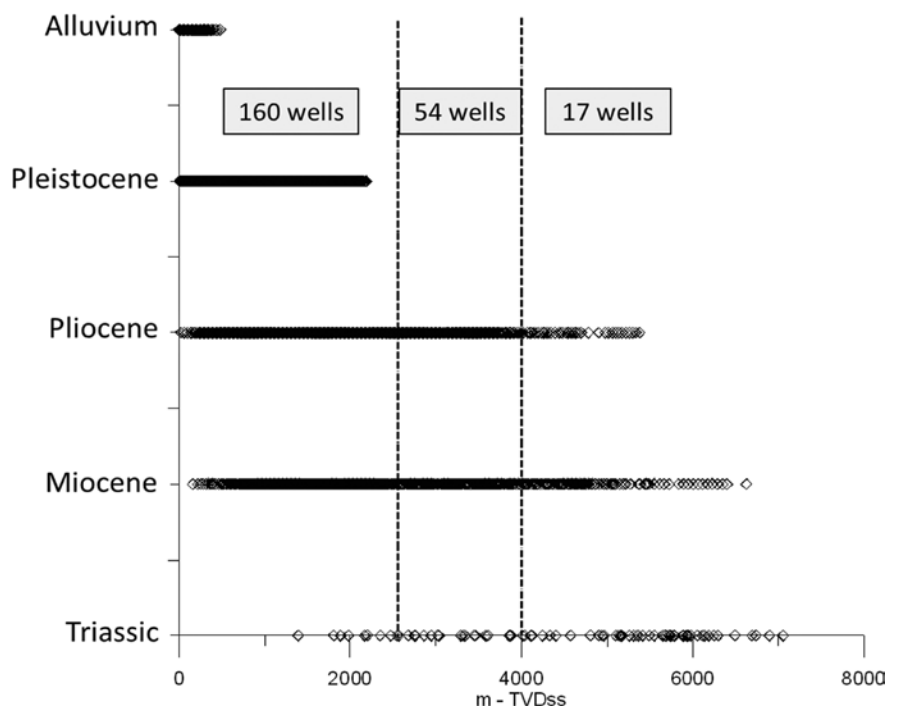

Fig. 4 – Graphs indicating the depth intervals covered by each of the stratigraphic units. The vertical dashed line corresponds to the depth limit that indicates the best well data coverage (maximum number of wells intercepting these depths).

at 2500 meters indicates that the available well data effectively cover the Alluvium, Pleistocene, and a significant portion of the Pliocene and Miocene deposits, with all wells (160) sampling these depths. However, the well data coverage decreases when examining the intermediate parts of the Pliocene and Miocene, with 54 wells sampling this interval while the deeper parts of those stratigraphic intervals and the largest part of the Triassic deposits are sampled by 17 wells only.

The definition of the lithological logs was one of the main objectives during the digitization and analysis part of the geological profiles. Lithologies were recognized in all the wells based on the available information from the well cuttings and in some cases from core analysis. Figure 5 shows an overall histogram with the lithologies from all the wells while in
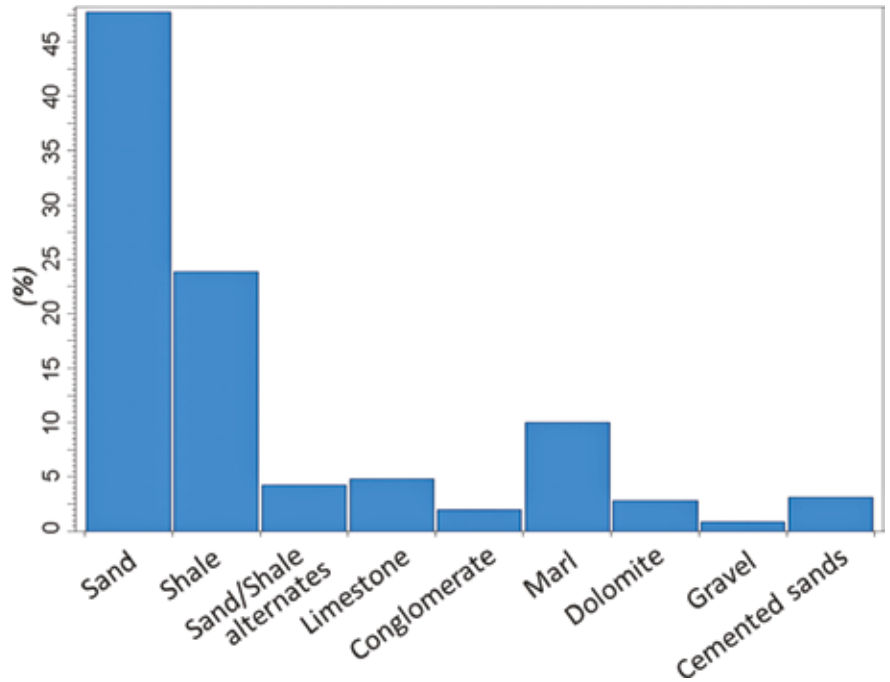

Fig. 5 – Histogram showing the distribution of the 9 macro-lithological groups at the wells position.

fig. 6 are presented separate histograms showing the abundance of these lithologies inside each of the 5 main stratigraphic units.
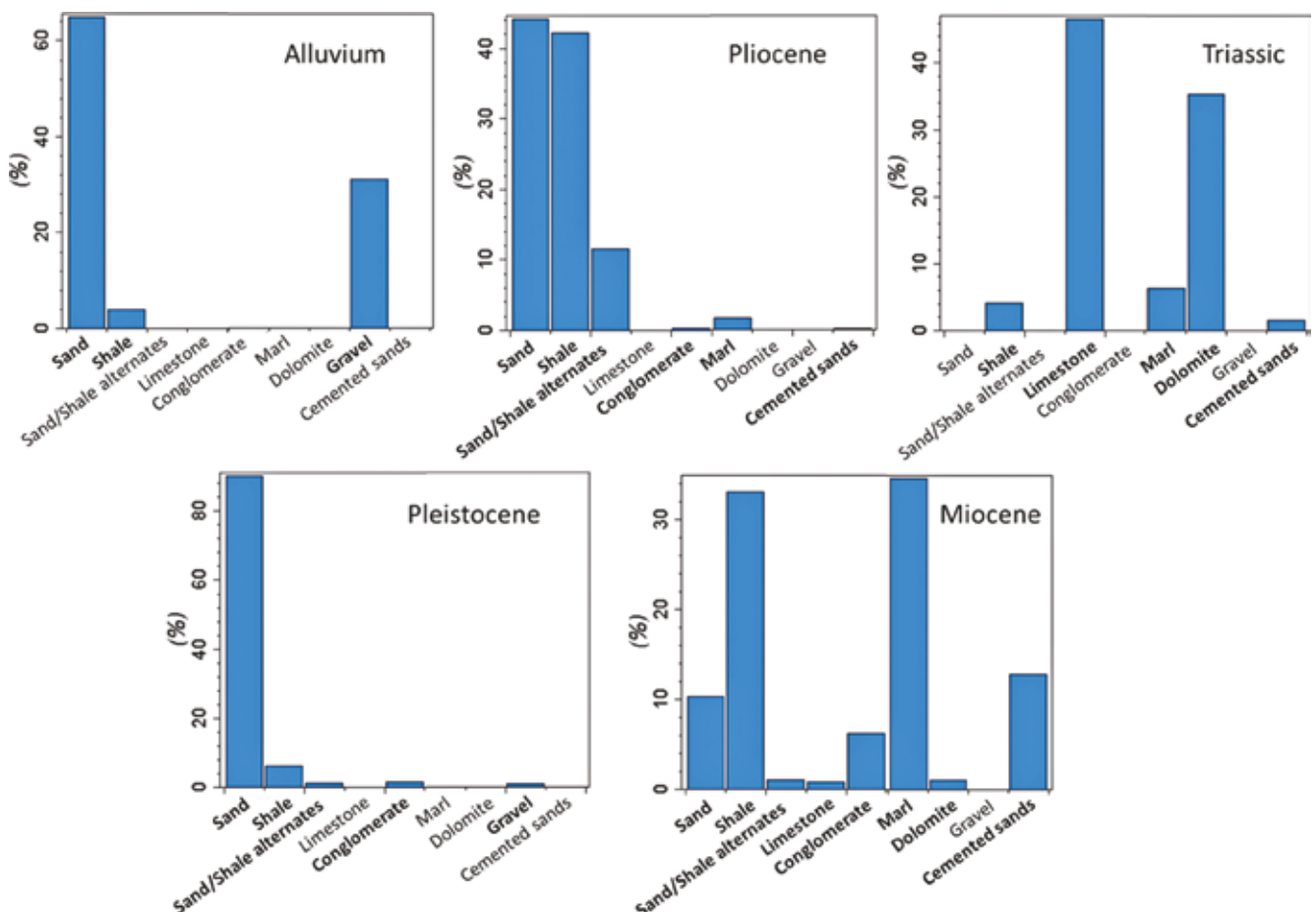

Fig. 6 – Histograms showing the lithological content for each stratigraphic zone.

From the histograms of fig. 6 we can note the prevalence of sand in the Alluvium and Pleistocene deposits; sand is strongly linked to the deposition of turbiditic deposits in a large part of the basin. During the Pliocene period, the shale content significantly increased due to the deposition of the Argille del Santerno Fm. During the Miocene period, we observe a variety of lithological types that include significant percentages of marls, conglomerates and cemented

sands. In the portion of the wells belonging to the Triassic period we observe mostly limestones and dolomites linked to the carbonate platform.

The digitization of the sonic logs (Sonic) offers valuable information regarding the sonic seismic velocities and their variation with depth for the Po Plain area. Figure 7 displays graphs illustrating the fluctuations in P-wave sonic velocities at different depths for the identified macro-lithological units.

This figure reveals that limestones and dolomites maintain relatively constant velocities regardless of depth. In contrast, lithologies like marls and cemented sandstones exhibit a distinctive behavior: a cessation in velocity increase that occurs at approximately 4 km depth, followed by a consistent trend at greater depths. More information regarding the velocity variations for each macro-lithological group can be found in Benetatos *et al.*, (2019).
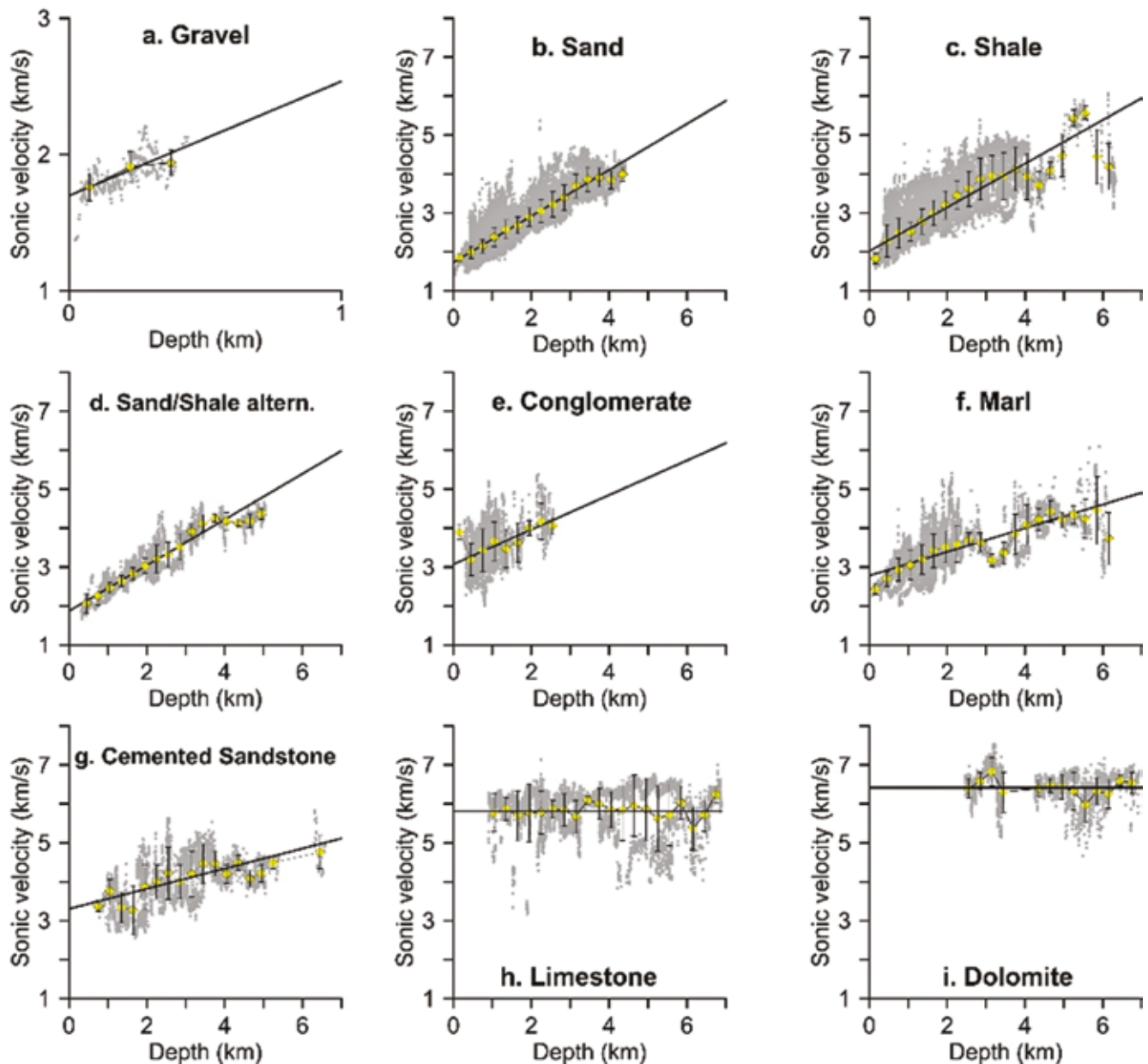
Fig. 7 – Relations between sonic velocities and depth for each lithological type recognized at the well profiles. The black line corresponds to the simple linear regression. The yellow points with the corresponding black upper and lower bounds correspond to the average values and standard deviation of the sonic velocities for 300 m intervals (fig. from Benetatos *et al.*, 2023).

The sonic velocities of the primary stratigraphic units were compared with those documented in the work of Montone and Mariucci (2020). The findings are outlined in Table 1 and represented in fig. 8. In those cases where the velocity values of a specific lithological composition are more appropriate for comparison purposes than those of the entire stratigraphic unit, such values have been utilized in the table. In some cases, merging the velocity results from two stratigraphic units was necessary in order to perform a more accurate comparison with the results of the other researchers.

5. Conclusions

The discovery and exploitation of numerous hydrocarbon resources in the Po Plain basin led to large-scale exploration activities, in particular by Eni-Agip company. The investigated area comprises the Po Plain and at the central
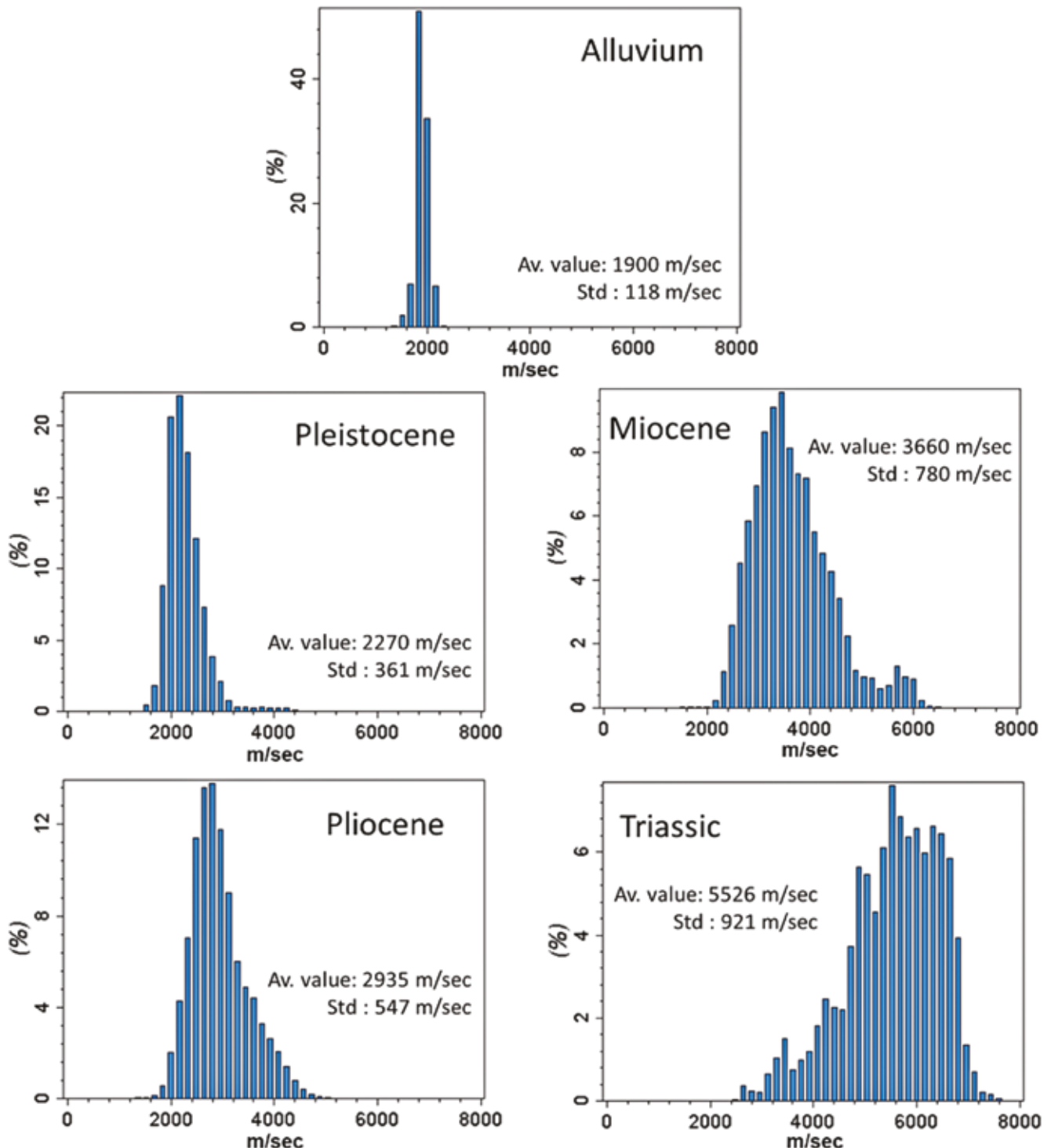

Fig. 8 – Histograms indicating the distribution of the sonic P-wave velocities for each stratigraphic unit.

Tab. 1 – P-wave sonic velocity (km/s, mean and standard deviation) compared to other studies. Units are: Q, Quaternary; PL, Pliocene; MIO-PL, Miocene-Pliocene; FMA, Marnoso Arenacea Formation; EO-MIO, Eocene-Miocene; C-EO, Cretacic-Eocene; J-C, Jurassic-Cretacic; J, Jurassic; TR, Triassic; V, Verrucano. (Table mod. from Montone and Mariucci, 2020).

	This study	Montone and Mariucci (2020)	Lithostratigraphic units from Porreca et al.	This study	Porreca et al. (2018)	Latorre et al. (2016)	Scisciani et al. (2014)	Bigi et al. (2011)	Mirabella et al. (2011)	Barchi et al. (1998)	Bally et al. (1986)
UNIT	vel. (km/sec)	vel. (km/sec)		vel. (km/sec)	vel. (km/sec)	vel. (km/sec)	vel. (km/sec)	vel. (km/sec)	vel. (km/sec)	vel. (km/sec)	vel. (km/sec)
Q	2.3 ± 0.3	2.2 ± 0.1	Plio-Pleistocene	2.6 ± 0.6			3.6		2.0	2.3-2.5	2.0
PL	2.9 ± 0.5	3.4 ± 0.6									2.6
MIO-PL	3.7 ± 0.8	4.0 ± 0.5	Miocene Turbidites	3.4 ± 0.6	4.0		4.0	3.6			3.4-4.0
FMA		4.0 ± 0.3				3.9			4.0	4.0	
EO-MIO		4.8 ± 0.5	Marly group	3.7 ± 0.8			5.0	4.5		4.0	3.4
C-EO	5.5 ± 0.9	5.8 ± 0.3	Scaglia group	5.7 ± 0.8	5.8	5.7		5.8	5.6		4.5
J-C		5.9 ± 0.4	Carbonate multilayer				5.5	6.1		5.5	5.2
J		6.3 ± 0.4	Calcare Massiccio Fm.				6.8	6.4			6.0
TR		6.3 ± 0.3	Evaporites		6.4	6.3	6.0	6.0	6.1	6.1	6.4
V		4.9 ± 0.2	Basement s.l. phyllites		5.1	5.3	5.5		5.1	5.0	3.9
			Crystalline basement unit			5.8	6.0		6.0	5.5	

and northern Adriatic Sea. These activities resulted in the accumulation of a large volume of data related to the basin's subsurface that includes 2D and 3D seismic surveys at the local and regional scale and well-log data. The digitization of a large part of that dataset, performed by Livani *et al.* (2023), has provided a lot of information in a digital format for further analysis. This dataset encompasses a large range of geological and stratigraphic data, offering valuable insights into lithology, stratigraphy and geophysical properties of the Po Plain, providing a useful data pool to many other researchers.

The preliminary statistical analysis conducted in this study provides a first insight into the relationships between lithologies, geological formations, and seismic velocities in the Po Plain area. It is evident that the distribution of lithologies across the different stratigraphic units is linked to the complex geological history of the region. Furthermore, the analysis of sonic log data offered the possibility to calculate the seismic velocities, revealing their different characteristics and trends with depth, and to link them to lithologies. The velocity data also provided critical information for geomechanical simulations during subsurface operations (Benetatos *et al.*, 2023), offering the basis for further geological and geophysical studies.

References

Bally, A., Burbi, L., Cooper, C. & Ghelardoni, R. (1986). Balanced sections and seismic reflection profiles across the central Apennines. Mem. Soc. Geol. Ital. 35, 257-310.

Barchi, M. *et al.* (1998). The structural style of the Umbria-Marche fold and thrust belt. Mem. Soc. Geol. Ital. 52, 557-578

Benetatos, C. Rocca, V., Sacchi, Q. Verga, F., (2015). How to Approach Subsidence Evaluation for Marginal Fields: A Case History. Open Petrol. Eng. J., 8, 213-234.

Benetatos, C., Codegone, G., Deangeli, C. Giani, G.P. Gotta, A., Marzano, F. Rocca, V., Verga, F., (2017). Guidelines for the Study of Subsidence Triggered by Hydrocarbon Production. GEAM, 152, 85-96.

Benetatos, C., Codegone, G., Marzano, F., Peter, C., Verga, F., (2019). Calculation of Lithology-Specific p-Wave Velocity Relations from Sonic Well Logs for the Po-Plain Area and the Northern Adriatic Sea; Offshore Mediterranean Conference and Exhibition 2019, OMC: Ravenna, Italy, 2019; p. 148084.

Benetatos, C., Codegone, G., Ferraro, C., Mantegazzi, A., Rocca, V., Tango, G., Trillo, F., (2020). Multidisciplinary Analysis of Ground Movements: An Underground Gas Storage Case Study. Remote Sens., 12, 3487. https://doi.org/10.3390/rs12213487

Benetatos, C., Catania, F., Giglio, G., Pirri, C.F., Raeli, A., Scaltrito, L., Serazio, C., Verga, F., (2023). Workflow for the Validation of Geomecha-

nical Simulations through Seabed Monitoring for Offshore Underground Activities. J. Mar. Sci. Eng., 11, 1387. https://doi.org/10.3390/jmse11071387

Bertello, F., Fantoni, R., Franciosi, R., (2008). Overview of the Italy's Petroleum Systems and Related Oil and Gas Occurrences. CD Extended Abstract & Exhibitor's Catalogue, 70th EAGE Conference & Exhibition, A018, pp. 1-4

Bertello, F., Fantoni, R., Franciosi, R., Gatti, V., Ghielmi, M., Pugliese, A., (2010). From thrust-and-fold belt to foreland: hydrocarbon occurrences in Italy. In: Vining, B.A., Pickering, S.C.(Eds.) Petroleum geology: from mature basin to new frontiers. Proceedings of the 7th Petroleum Geology Conference, pp. 113-112. doi: 10.1144/0070113.

Bigi, S., Casero, P. & Ciotoli, G., (2011). Seismic interpretation of the Laga basin; constraints on the structural setting and kinematics of the Central Apennines. J. Geol. Soc. London 168, 179-190, https://doi.org/10.1144/0016-76492010-084

Casero, P., (2004). Structural setting of petroleum exploration plays In Italy. Special Volume of the Italian Geological Society for the IGC 32 Florence-2004, pp. 189-199.

Casero, P., Bigi, S., (2013). Structural setting of the Adriatic basin and the main related petroleum exploration plays. Marine and Petroleum Geology, vol. 42, pp. 135-147. https://doi:10.1016/j.marpetgeo.2012.07.006

Casnedi, R., Crescenti, U., Tonna, M. (1982). Evoluzione della avanfossa adriatica meridionale nel Plio-Pleistocene, sulla base di dati di sotto-suolo. Memorie della Società Geologica Italiana, vol. 20, pp. 243-260

Cazzini, F., Dal Zotto, O., Fantoni, R., Ghielmi, M., Ronchi, P., Scotti, P., (2015). Oil and gas in the Adriatic foreland, Italy. Journal of Petroleum Geology, vol. 38 (3), pp. 255-279. doi:10.1111/jpg.12610

Cazzini F., Dal Zotto O., Fantoni R., Ghielmi M., Ronchi P., Scotti P., (2018). Oil and gas in the Adriatic foreland, Italy. Journal of Petroleum Geology, 38(3), 255-279.

Dondi, L., Mostardini, F., Rizzini, A. (1982). Evoluzione sedimentaria e paleogeografica nella Pianura Padana. In: Cremonini G., Ricci Lucchi F. (Eds.), Guida alla Geologia del margine appenninico-padano. Guide Geologiche Regionali, Società Geologica Italiana, pp. 47-58

Fantoni , R., Bersezio, R., Forcella, F., (2004). Alpine structure and deformation chronology at the Southern Alps-Po Plain border in Lombardy. Bollettino della Società Geologica Italiana, vol. 123, pp. 463-476

Fantoni, R., Franciosi, R., (2010). Mesozoic extension and Cenozoic compression in Po Plain and Adriatic foreland. Rendiconti Lincei – Scienze Fisiche e Naturali, vol. 21 (1), pp. 197-209. doi: 10.1007/s12210-010-0102-4

Ghielmi, M., Minervini, M., Nini, C., Rogledi, S., Rossi, M., Vignolo, A., (2010). Sedimentary and tectonic evolution in the eastern Po-Plain and northern Adriatic Sea area from Messinian to Middle Pleistocene (Italy). Rendiconti Lincei Scienze Fisiche e Naturali, vol. 21, pp. S131-S166. doi: 10.1007/s12210-010-0101-5.

Latorre, D., Mirabella, F., Chiaraluce, L., Trippetta, F. & Lomax, A., (2016). Assessment of earthquake locations in 3-D deterministic velocity models: a case study from the Altotiberina near fault observatory (Italy). J. Geophys. Res. 121, 8113-8135, https://doi.org/10.1002/2016JB013170

Livani, M., Petracchini, L., Benetatos, C., Marzano, F., Billi, A., Carminati, E., Doglioni, C., Petricca, P., Maffucci, R.,Codegone, G., et al.(2023). Subsurface Geological and Geophysical Data from the Po Plain and the Northern Adriatic Sea (North Italy). Earth System Science Data Discussions 2023, 1-41, doi:10.5194/essd-2023-65.

Mirabella, F., Brozzetti, F., Lupattelli, A. & Barchi, M.R., (2011). Tectonic evolution of a low-angle extensional fault system from restored cross sections in the Northern Apennines (Italy). Tectonics 30, TC6002, https://doi.org/10.1029/2011TC002890

Montone, P., Mariucci, M.T., (2020). Constraints on the Structure of the Shallow Crust in Central Italy from Geophysical Log Data. Sci Rep 10, 3834. https://doi.org/10.1038/s41598-020-60855-0

Porreca, M. et al., (2018). Seismic reflection profiles and subsurface geology of the area interested by the 2016-2017 earthquake sequence (Central Italy). Tectonics 37, 1116-1137, https://doi.org/10.1002/2017TC004915

Scisciani, V. et al., (2014). Positive inversion tectonics in foreland fold and thrust belts: a reappraisal of the Umbria-Marche northern Apennines (Central Italy) by integrating geological and geophysical data. Tectonophysics 637, 218-237, https://doi.org/10.1016/j.tecto.2014.10.010